Resonance Production and Nuclear Fragmentation for Space Radiation

by

Ryan B. Norman

A Dissertation

Submitted to the Faculty

of the

Worcester Polytechnic Institute

in partial fulfillment of the requirements for the

Degree of Doctor of Philosophy

in

Physics

April 2008

Resonance Production and Nuclear Fragmentation for Space Radiation

by

Ryan B. Norman

A Dissertation

Submitted to the Faculty

of the

Worcester Polytechnic Institute

in partial fulfillment of the requirements for the

Degree of Doctor of Philosophy

in

Physics

April 2008

APPROVED:

Professor John W. Norbury, Major Advisor

Professor Padmanabhan K. Aravind, Co-Advisor

Dr. Steve R. Blattnig, Co-Advisor
NASA Langley Research Center

Abstract

Space radiation and its effects on human life and sensitive equipment are of concern to a safe exploration of space. Radiation fields are modified in quality and quantity by intervening shielding materials. The modification of space radiation by shielding materials is modeled by deterministic transport codes using the Boltzmann transport equation. Databases of cross sections for particle production are needed as input for transport codes. A simple model of nucleon-nucleon interactions is developed and used to derive differential and total cross sections. The validity of the model is verified for proton-proton elastic scattering and applied to Δ-resonance production. Additionally, a comprehensive validation program of the nucleus-nucleus fragmentation cross section models NUCFRG2 and QMSFRG is performed. A database of over 300 experiments was assembled and used to compare to model fragmentation cross sections.

Acknowledgements

First and foremost, thanks to my wife, Rebecca, for her unending support, limitless patience and infallible belief in me. Also, thanks to my son Liam, whom I dedicate this work, for reminding me that no matter how dark the tunnel is, the light at the end is warm, beautiful and worth the journey! Thanks to my parents, brother and my whole family, for always believing in me and supporting my studies.

Special thanks to Dr. Steve Blattnig for all the guidance, insight and help he has been kind enough to give me over the years. Also, special thanks to Professor P.K. Aravind for stepping in as my advisor and mentor at WPI. Last but not least, very special thanks to Professor John Norbury for the years of patience, guidance and tutelage extending back to when I was an undergraduate student and continuing through graduate school. I am very proud to call all of you my mentors.

Contents

List of Figures

List of Tables

Chapter 1

Introduction

1.1 Background and Motivation

On the surface of the Earth, life is shielded from the harmful radiation of space by the Earth's atmosphere and magnetic field. Once a person leaves the confines of Earth's surface, however, they subject themselves to the radiation environments of space that can damage both biological tissues and important electronic systems. Shielding of this radiation must occur if these sensitive sites are to avoid potentially lethal effects. The addition of extra weight to a spacecraft payload due to excessive shielding can be exceedingly expensive and therefore efficient shielding techniques are advantageous. The reduction of parasitic shielding can be achieved by a better understanding of radiation through increased research to determine the effects of radiation and how it is modified as it traverses shielding materials. Increasing our current understanding of how radiation interacts with intervening shielding materials will translate into a better evaluation of the effects on electronics and living tissue and ultimately decrease costs.

The danger of radiation is contained in its ionizing effects. Ionizing radiation consists of moving particles that have sufficient energy to remove an electron from an atom or molecule, causing the atom or molecule to become charged, or ionized. The ionization produced from this radiation can significantly alter the structure of molecules within a

living cell, potentially leading to the death of the cell or possibly the entire organism.

As radiation passes through matter, such as the walls of a spacecraft, the composition of the radiation is altered. The modification of radiation as it passes through matter is affected by the production of secondary particles and is significant in the assessment of the effects on human tissue and electronics. Although secondary particles, such as light-ions or pions, may directly ionize cells or electronics, secondary particles are also of concern due to their indirect effects. These indirect effects are due to the multiple decay products of the meson that can be more damaging than the original particle. A secondary particle or one of its decay products can ionize the atoms of a medium, generating free electrons, muons and other particles. The produced free particles can then ionize additional atoms creating more free particles. The damage due to this chain reaction, called an electromagnetic cascade, can be much more harmful than the initial single particle.

To account for the modification of radiation as it interacts with intervening shielding material and obtain an accurate understanding of the radiation environment inside a spacecraft given the external radiation environment, the radiation transport code HZETRN [1] was created. HZETRN solves the one-dimensional Boltzmann transport equation in the straight-ahead approximation and was developed as a fast and accurate engineering tool to aid in the design of spacecraft and modules [1].

HZETRN requires accurate cross section databases of all particle interactions that are of interest from a space radiation perspective. The evaluation and development of these cross section databases is the focus of this work. I introduce a scalar quantum field theory of pion exchange, called the scalar one pion exchange model (SOPEM), for nucleon-nucleon scattering in an attempt to provide an accurate description of the nucleon-nucleon interaction over a large range of projectile kinetic energies. After comparing the scalar one pion exchange model to proton-proton elastic scattering, I apply the model to the production of Δ-resonances and complete a comparison analysis with two competing models and available experimental data for single and double Δ-resonance production. The production of pions via an intermediate Δ-resonance is an important process at the

energies of interest for space radiation [2–4]. In addition, I investigate two models of nuclear fragmentation and compare the models to an extensive experimental cross section database I compiled to determine the validity of the nuclear fragmentation models, identify model weaknesses and determine how nuclear fragmentation model discrepancy affects the results of analysis using HZETRN.

1.2 Space Radiation Environment

The radiation environment of space is quite complex, varying both spatially and temporally and consisting of a wide array of particles. There exist three main sources of radiation that are of importance to space operations: terrestrial, solar and galactic. Terrestrial radiation is contained in the Earth's two radiation belts known as the inner and outer Van Allen belts. Solar radiation originates from the sun and galactic cosmic rays are a low intensity background radiation that exists throughout the galaxy. Each type of radiation will be discussed below.

1.2.1 Terrestrial Radiation

The Earth's magnetosphere is able to confine charged particles to regions of space surrounding the Earth creating radiation belts. The Earth's radiation belts consist of two belts, called the inner and outer belts, that surround the earth. Radiation is trapped in these belts by the Earth's magnetic field. Ions, mainly protons, of the inner belt and electrons of the outer belt are the main source of problems because they reach energies high enough to significantly penetrate matter.

The inner belt is a relatively stable collection of protons, with electrons and heavier ions. The protons can reach energies of hundreds of MeVs and generally exist at an average distance of 3 Earth radii (R_E) above the surface of the Earth [5–8]. In general, the geomagnetic field lines are not geocentric, but offset. In addition, the inner belt drops very close to the Earth's surface in a region of the southern Atlantic ocean. This gives rise to the phenomenon known as the South Atlantic Anomaly (SAA). The SAA has been

shown to account for about half the radiation dose received by an astronaut even though a crew will only spend approximately 2–5% of their time within the SAA [6].

The outer belt is dominated by electrons with energies on the order of 10 keV to 10 MeV. The outer belt extends out to approximately 12 R_E [5, 8]. The variation of the radiation belts, especially the outer belt, is affected mainly by the Sun. Order of magnitude increases in the electron intensity correlate with the solar wind phenomenon known as high-speed solar wind streams [6].

1.2.2 Solar Radiation

Solar radiation energetic enough to significantly penetrate matter is called a solar particle event (SPE). SPEs consist mainly of hydrogen and helium, with the heavier ion component typically neglected due to the small flux [5]. Large SPEs typically occur during active solar periods and correlate with the 11 year sun spot cycle but exceptions do occur. They can be produced by solar flares or shock driven by coronal mass ejections [7]. The ability to predict when an SPE will occur, and its associated energy spectrum, is poor. To account for this, worst case scenarios are used for shielding analysis. In fact, one of the worst case scenarios used in shielding analysis, the August 1972 SPE, occurred during the fairly quiet solar cycle 20 [5].

1.2.3 Galactic Cosmic Rays

Galactic cosmic rays (GCRs) are particles traveling with energy from 10^8 eV to above 10^{20} eV with a peak flux occurring at about 300 MeV (10^6 eV = 1 MeV), composed of about 2% electrons and positrons and 98% ionized nuclei and originating from outside the solar system. The nuclear component is made up of approximately 87% protons, 12% alphas (helium nuclei) and 1% heavier nuclei [9, 10].

GCRs are distributed isotropically with temporal variations anti-correlated with solar activity. The interplanetary magnetic field generated by the Sun provides a shielding effect resulting in a decrease of integral GCR flux by roughly a factor of 2 during solar

maximum compared to solar minimum. Of the three sources of space radiation, GCRs have the smallest intensity with a maximum total fluence rate of about 4 particles cm^{-2} s^{-1} [10].

Chapter 2

Scalar Quantum Field Theory and Proton-Proton Elastic Scattering

2.1 Introduction

An accurate understanding of the elementary particle interactions in the energy range of the galactic cosmic ray (GCR) spectrum is important to the shielding of sensitive equipment and personnel on long duration space missions [4]. In order to determine the validity of current models of the strong force at energies of importance to the shielding of galactic cosmic rays, the one pion exchange model (OPEM) is investigated in this work. In the OPEM, the interaction of nucleons is mediated by the exchange of a pion. The pion couples to the nucleons via a pseudoscalar interaction and the invariant amplitude is calculated in a full field theoretic framework which includes spin and isospin.

Recently the NASA heavy ion transport code, HZETRN, was extended to include the effects of pion and muon production in the meson and muon transport code MESTRN [4]. An important production mechanism of pions in the energy range of .5 to 3 GeV is through an intermediate resonance state. This region of energy is of significance to space radiation shielding because the GCR flux peaks there. The Δ-resonance (the first excited state of the nucleon) has been shown [11] to account for the majority of the pion production cross

section near 1 GeV. Currently, MESTRN does not include the production of particles from an intermediate resonant state.

MESTRN uses parameterizations of the inclusive cross section, $p+p \rightarrow \pi^{\pm}+X$ (where X is everything else allowed in the reaction), using high energy data for the direct production of pions from proton-proton interactions. In fact, due to the scarcity of total cross section (σ) data for this inclusive process, Lorentz invariant differential cross section ($E\frac{d^3\sigma}{dp^3}$) parameterizations were numerically integrated to get spectral cross section ($\frac{d\sigma}{dE}$) points [12]. These numerically integrated points were then used as "data" to fit parameterizations of the total cross section for pion production from proton-proton collisions. The preciseness of the total cross section parameterizations is limited by both the accuracy of the original parameterization of the Lorentz invariant differential cross section and the accuracy of the total cross section parameterization to the numerically integrated Lorentz invariant differential cross section parameterization. The parameterizations were compared to total cross section data by Blattnig *et al.* in Ref. [12]. This data was very limited for the charged pions, consisting of only 3 data points in the laboratory kinetic energy range of approximately 10-25 GeV. From the perspective of radiation transport, this is not as desirable as one might hope, since the GCR spectrum peaks around 1 GeV/nucleon and drops by about an order of magnitude by 10 GeV/nucleon [9]. Since all of these issues stem from the parameterizations used, it would be useful to have the cross sections used in MESTRN developed from the physics of the interaction, not simply parameterizations. The addition of cross sections based on physical models and the inclusion of intermediate resonance states into MESTRN is the ultimate goal of this research.

A promising theoretical mechanism for including the Δ-resonance is through the one boson exchange model (OBEM) [2]. The OBEM is an extension of the OPEM that uses the exchange of virtual mesons in addition to the pion to mediate the strong force at low energies where perturbative quantum chromodynamics (QCD) is unfeasible. As a first step in the implementation of this model into the physics of MESTRN, proton-proton elastic scattering is considered using the framework of the OPEM. In general, however,

nucleon-nucleon elastic scattering is important to transport codes that include trapped radiation and solar radiation environments. The theoretical cross sections of the OPEM, both total and differential, are then compared to experimental data.

Deterministic transport codes require simple formulas for both total and differential cross sections in order to minimize the computational power required for shielding analysis. With that in mind, the simplest possible theories should be used whenever possible and therefore a simple scalar theory is presented in addition to the OPEM. The scalar theory is based on the theory presented by Griffiths [13, 14], called ABC theory. It is presented as a full quantum field theory and is compared to both the OPEM and experimental data in an attempt to give insight into the importance of spin at these energies.

2.2 Pseudoscalar Theory: One Pion Exchange Model

In the one pion exchange model, a virtual pion is used to mediate the force between two interacting nucleons. As the lightest meson, the pion has the longest interaction range and therefore is the dominant mechanism at low energies. As the incident nucleon's energy increases, the interaction range decreases, and the theoretical cross sections fit to the data should worsen. The inclusion of heavier bosons and multiple boson processes to the exchange mechanism has been shown to fit the data well at higher energies [15].

The Feynman rules for the OPEM with pseudoscalar coupling of the pion to the nucleon are presented below and the Feynman diagrams are shown in Figure 2.1:

1. Interaction Lagrangian:

$$\mathcal{L}_{\pi NN} = -ig_{\pi NN}\bar{\Psi}\gamma_5\boldsymbol{\tau}\cdot\boldsymbol{\pi}\Psi. \tag{2.1}$$

2. Vertex:

$$-ig_{\pi NN}\gamma_5\tau_i. \tag{2.2}$$

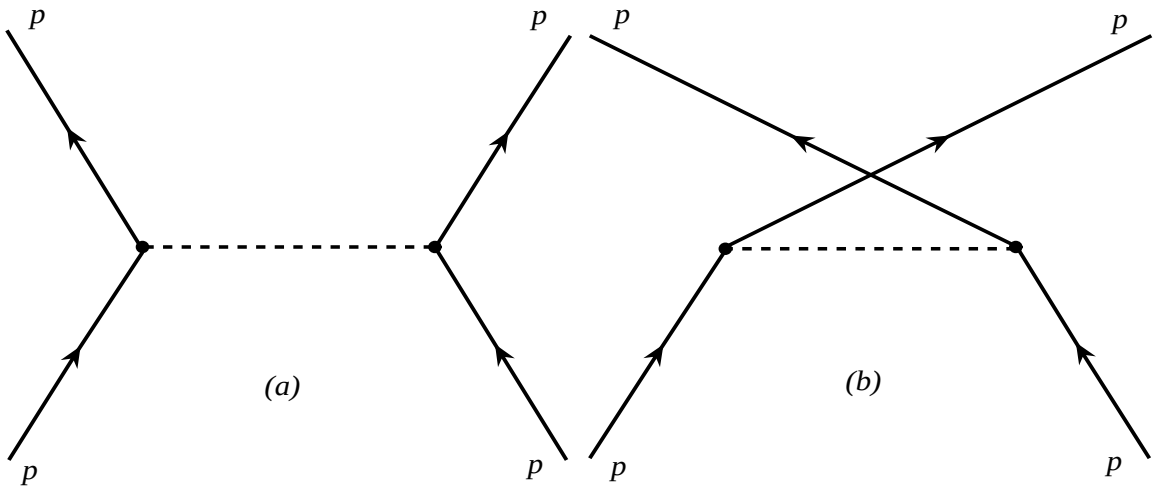

Figure 2.1: The Feynman diagrams of the direct and exchange amplitudes that contribute to the proton-proton elastic scattering process.

3. Propagator:

$$\frac{i\delta_{ij}}{q^2 - m_\pi^2}. \tag{2.3}$$

Where Ψ is the nucleon field and $\boldsymbol{\pi}$ is the pion field. $\boldsymbol{\tau}$ are the usual Pauli isospin matrices, γ_5 is the product of Dirac gamma matrices and is equal to $-i\gamma_0\gamma_1\gamma_2\gamma_3$, $g_{\pi NN}$ is the coupling constant of the pion-nucleon-nucleon vertex and q is the momentum of the exchange particle, the pion. In Equation 2.1, one can expand the fields as $\bar{\Psi}\boldsymbol{\tau}\cdot\boldsymbol{\pi}\Psi = \sqrt{2}\bar{p}n\pi^- + \sqrt{2}\bar{n}p\pi^+ + \bar{p}p\pi^0 - \bar{n}n\pi^0$ (see Appendix A).

2.2.1 Invariant Amplitude

For proton-proton (pp) elastic scattering the t channel (direct channel) amplitude is given by Feynman's rules corresponding to Figure 2.1(a):

$$i\mathcal{M}_d = \frac{i\delta_{ij}g_{\pi NN}}{t - m_\pi^2}(\bar{\Psi}_3\tau_i\gamma_5\Psi_1)(\bar{\Psi}_4\tau_j\gamma_5\Psi_2). \tag{2.4}$$

The u channel (exchange channel) amplitude for pp elastic scattering, corresponding to

Figure 2.1(b), is given as:

$$i\mathcal{M}_e = \frac{i\delta_{ij} g_{\pi NN}}{u - m_\pi^2}(\bar{\Psi}_4 \tau_i \gamma_5 \Psi_1)(\bar{\Psi}_3 \tau_j \gamma_5 \Psi_2), \tag{2.5}$$

Where $\Psi_i = \Psi(p_i)$ and define t and u as:

$$t \equiv (p_1 - p_3)^2, \tag{2.6}$$

$$u \equiv (p_1 - p_4)^2, \tag{2.7}$$

and p_i is the 4-momentum of the ith particle.

Now take the isospin terms out and group them together in the following way:

$$\delta_{ij}\tau_i\tau_j = \tau_i\tau_i \equiv I. \tag{2.8}$$

It should be noted that the isospin factors, I, must be the same for both the direct and exchange channels since this is proton-proton elastic scattering. For clarity, the terms I_d and I_e, corresponding to the direct and exchange terms will remain in the calculation until the very end.

To compute the cross section, square the total invariant amplitude and sum over the final spin states and average over the initial spin states.

$$\frac{1}{4}\sum_{spins}|\mathcal{M}|^2 = \frac{1}{4}\sum_{spins}(|\mathcal{M}_d|^2 + |\mathcal{M}_e|^2 - \mathcal{M}_d^*\mathcal{M}_e - \mathcal{M}_e^*\mathcal{M}_d). \tag{2.9}$$

Now look at each term in Equation 2.9 separately.

$$\frac{1}{4}\sum_{spins}|\mathcal{M}_d|^2 = \sum_{spins}\frac{g_{\pi NN}^4 I_d^2}{4(t - m_\pi^2)^2}(\bar{\Psi}_4\gamma_5\Psi_1)(\bar{\Psi}_4\gamma_5\Psi_1)^*(\bar{\Psi}_3\gamma_5\Psi_2)(\bar{\Psi}_3\gamma_5\Psi_2)^*. \tag{2.10}$$

Use the following to simplify Equation 2.10.

$$(\bar{\Psi}_i\gamma_5\Psi_j)^* = \Psi_j^\dagger\gamma_5^\dagger\gamma_0^\dagger\Psi_i = \Psi_j^\dagger\gamma_5\gamma_0\Psi_i = -\Psi_j^\dagger\gamma_0\gamma_5\Psi_i = -\bar{\Psi}_j\gamma_5\Psi_i. \tag{2.11}$$

Using this fact one obtains:

$$\frac{1}{4}\sum_{spins}|\mathcal{M}_d|^2 = \sum_{spins}\frac{g_{\pi NN}^4 I_d^2}{4(t-m_\pi^2)^2}(\bar{\Psi}_4\gamma_5\Psi_1)(\bar{\Psi}_1\gamma_5\Psi_4)(\bar{\Psi}_3\gamma_5\Psi_2)(\bar{\Psi}_2\gamma_5\Psi_3). \tag{2.12}$$

Now perform the sum over the spins using the convention of Peskin and Schroeder [16] where

$$\sum_s \Psi^s\bar{\Psi}^s = \not{p} + m, \tag{2.13}$$

$$\begin{aligned}\frac{1}{4}\sum_{spins}|\mathcal{M}_d|^2 &= \frac{g_{\pi NN}^4 I_d^2}{4(t-m_\pi^2)^2}Tr[(\not{p}_4+m_p)\gamma_5(\not{p}_1+m_p)\gamma_5] \\ &\quad \times Tr[(\not{p}_3+m_p)\gamma_5(\not{p}_2+m_p)\gamma_5],\end{aligned} \tag{2.14}$$

where one must remember that $\not{p}_i = \gamma_\mu p_i^\mu$ and

$$Tr(\text{odd number of gammas}) = 0, \tag{2.15}$$

$$\gamma_5\gamma_5 = \begin{pmatrix} 1 & 0 & 0 & 0 \\ 0 & 1 & 0 & 0 \\ 0 & 0 & 1 & 0 \\ 0 & 0 & 0 & 1 \end{pmatrix}. \tag{2.16}$$

Using the above, evaluate the traces to obtain the direct contribution to the invariant amplitude.

$$\frac{1}{4}\sum_{spins}|\mathcal{M}_d|^2 = \frac{g_{\pi NN}^4 I_d^2}{4(t-m_\pi^2)^2}(-4p_3\cdot p_1 + 4m_p^2)(-4p_4\cdot p_2 + 4m_p^2). \tag{2.17}$$

From Equations 2.6 and 2.7 one can see that

$$\begin{aligned} t &= (p_1 - p_3)^2 \\ &= p_1^2 + p_3^2 - 2p_1 \cdot p_3 \\ &= 2m_p^2 - 2p_1 \cdot p_3, \qquad (2.18) \\ \Longrightarrow p_1 \cdot p_3 &= m_p^2 - \frac{1}{2}t, \qquad (2.19) \end{aligned}$$

but $t = (p_2 - p_4)^2$ also. This implies that

$$p_2 \cdot p_4 = p_1 \cdot p_3 = m_p^2 - \frac{1}{2}t \qquad (2.20)$$

Now look at the Mandelstam variables u and s.

$$\begin{aligned} u &= (p_1 - p_4)^2 \\ &= (p_2 - p_3)^2, \qquad (2.21) \\ \Longrightarrow p_1 \cdot p_4 &= m_p^2 - \frac{1}{2}u \\ p_2 \cdot p_3 &= m_p^2 - \frac{1}{2}u, \qquad (2.22) \end{aligned}$$

$$\begin{aligned} s &= (p_1 + p_2)^2 \\ &= (p_3 + p_4)^2, \qquad (2.23) \\ \Longrightarrow p_1 \cdot p_2 &= \frac{1}{2}s - m_p^2 \\ p_3 \cdot p_4 &= \frac{1}{2}s - m_p^2. \qquad (2.24) \end{aligned}$$

Now returning to Equation 2.10 one can make some simplifications.

$$\begin{aligned}\frac{1}{4}\sum_{spins}|\mathcal{M}_d|^2 &= \frac{g_{\pi NN}^4 I_d^2}{4(t-m_\pi^2)^2}(-4p_3\cdot p_1+4m_p^2)(-4p_4\cdot p_2+4m_p^2)\\ &= \frac{g_{\pi NN}^4 I_d^2}{4(t-m_\pi^2)^2}(-4(m_p^2-\frac{1}{2}t)+4m_p^2)(-4(m_p^2-\frac{1}{2}t)+4m_p^2)\\ &= \frac{g_{\pi NN}^4 I_d^2 t^2}{(t-m_\pi^2)^2}. \end{aligned} \tag{2.25}$$

To calculate the second term in Equation 2.10, replace $t \rightarrow u$ in Equation 2.25. Therefore:

$$\frac{1}{4}\sum_{spins}|\mathcal{M}_e|^2 = \frac{g_{\pi NN}^4 I_e^2 u^2}{(u-m_\pi^2)^2}. \tag{2.26}$$

Now calculate the cross terms

$$\begin{aligned}\frac{1}{4}\sum_{spins}\mathcal{M}_d^*\mathcal{M}_e &= \sum_{spins}\frac{g_{\pi NN}^4 I_d^* I_e}{4(t-m_\pi^2)(u-m_\pi^2)}(\bar{\Psi}_4\gamma_5\Psi_1)(\bar{\Psi}_3\gamma_5\Psi_2)\\ &\quad\times(\bar{\Psi}_2\gamma_5\Psi_4)(\bar{\Psi}_1\gamma_5\Psi_3)\\ &= \frac{g_{\pi NN}^4 I_d^* I_e}{4(t-m_\pi^2)(u-m_\pi^2)}Tr[(\not{p}_4+m_p)\gamma_5(\not{p}_1+m_p)\\ &\quad\times\gamma_5(\not{p}_3+m_p)\gamma_5(\not{p}_2+m_p)\gamma_5]\\ &= \frac{g_{\pi NN}^4 I_d^* I_e}{4(t-m_\pi^2)(u-m_\pi^2)}[(\frac{1}{2}u-m_p^2)^2-(\frac{1}{2}s-m_p^2)^2\\ &\quad+(\frac{1}{2}t-m_p^2)^2-4m_p^4]. \end{aligned} \tag{2.27}$$

Looking at the other cross term,

$$\begin{aligned}
\frac{1}{4}\sum_{spins}\mathcal{M}_e^*\mathcal{M}_d &= \sum_{spins}\frac{g_{\pi NN}^4 I_d I_e^*}{4(t-m_\pi^2)(u-m_\pi^2)}(\bar{\Psi}_2\gamma_5\Psi_3)(\bar{\Psi}_1\gamma_5\Psi_4) \\
&\quad\times(\bar{\Psi}_3\gamma_5\Psi_1)(\bar{\Psi}_4\gamma_5\Psi_2) \\
&= \frac{g_{\pi NN}^4 I_d I_e^*}{4(t-m_\pi^2)(u-m_\pi^2)}Tr[(\not{p}_2+m_p)\gamma_5(\not{p}_3+m_p)\gamma_5 \\
&\quad\times\not{p}_1+m_p)\gamma_5(\not{p}_4+m_p)\gamma_5] \\
&= \frac{g_{\pi NN}^4 I_d^* I_e}{4(t-m_\pi^2)(u-m_\pi^2)}[(\frac{1}{2}u-m_p^2)^2-(\frac{1}{2}s-m_p^2)^2 \\
&\quad+(\frac{1}{2}t-m_p^2)^2-4m_p^4]. \qquad (2.28)
\end{aligned}$$

Also note that in the case of elastic scattering the isospin factors are both equal to one ($I_d = I_e = 1$). Therefore our total spin averaged and summed invariant amplitude is:

$$\begin{aligned}
\frac{1}{4}\sum_{spins}|\mathcal{M}|^2 &= g_{\pi NN}^4\left\{\frac{t^2}{(t-m_\pi^2)^2}+\frac{u^2}{(u-m_\pi^2)^2}-\frac{2}{4(t-m_\pi^2)(u-m_\pi^2)}\right. \\
&\quad\left.\times\left[(\frac{1}{2}u-m_p^2)^2-(\frac{1}{2}s-m_p^2)^2+(\frac{1}{2}t-m_p^2)^2-4m_p^4\right]\right\}. \qquad (2.29)
\end{aligned}$$

2.2.2 Cross Section

Now that the invariant amplitude is calculated, the next step is to calculate the total cross section. The differential cross section is given as:

$$\frac{d\sigma}{dt} = \frac{S}{16\pi\lambda_{12}}\frac{1}{4}\sum_{spin}|\mathcal{M}|^2, \qquad (2.30)$$

where

$$\begin{aligned}
\lambda_{ij} &\equiv (s-m_i^2-m_j^2)^2-4m_i^2m_j^2, &(2.31)\\
\lambda_{12} &= s(s-4m_p^2), &(2.32)\\
s &\equiv (p_1+p_2)^2 \\
&= E_{cm}^2, &(2.33)
\end{aligned}$$

and the statistical factor S is given by $\frac{1}{j!}$ for j identical particles in the final state. So in the case of elastic scattering of protons, $S = \frac{1}{2}$. The total cross section is then

$$\sigma = \int_{t_\pi}^{t_0} \frac{d\sigma}{dt} dt. \tag{2.34}$$

The limits of the integration (see Appendix B for a derivation) are given as:

$$t_0(t_\pi) \equiv \frac{1}{4s}\left[(m_1^2 - m_2^2 - m_3^2 + m_4^2)^2 - (\sqrt{\lambda_{12}} \mp \sqrt{\lambda_{34}})^2\right]. \tag{2.35}$$

Which yields

$$t_0 = 0, \tag{2.36}$$

$$t_\pi = 4m_p^2 - s. \tag{2.37}$$

To simplify the calculation, break up the total cross section into parts: the direct, exchange, and interference portions:

$$\sigma = \sigma_d + \sigma_e + \sigma_i. \tag{2.38}$$

This will make our integration easier to understand. A new variable, K, is defined to make notation easier:

$$\begin{aligned} K &\equiv \frac{g_{\pi NN}^4 S}{16\pi\lambda_{12}} \\ &= \frac{g_{\pi NN}^4 m_p^4}{32\pi s(s - 4m_p^2)}. \end{aligned} \tag{2.39}$$

So the direct channel cross section is:

$$\begin{aligned} \sigma_d &= K\int_{t_\pi}^{t_0} \frac{t^2}{(t - m_\pi^2)^2} dt \\ &= K\left[\frac{(s - 4m_p^2)(4m_p^2 - 2m_\pi^2 - s)}{4m_p^2 - s - m_\pi^2} + 2m_\pi^2 ln\left(\frac{m_\pi^2}{s + m_\pi^2 - 4m_p^2}\right)\right]. \end{aligned} \tag{2.40}$$

For the exchange channel, one notices that:

$$
\begin{aligned}
u &= 4m_p^2 - s - t, && (2.41)\\
du &= -dt, && (2.42)\\
t_\pi &= u_0, && (2.43)\\
t_0 &= u_\pi, && (2.44)\\
& && (2.45)
\end{aligned}
$$

This all implies that

$$
\begin{aligned}
\sigma_e &= K\int_{t_\pi}^{t_0}\frac{u^2}{(u-m_\pi^2)^2}dt\\
&= K\int_{4m_p^2-s}^{0}\frac{u^2}{(u-m_\pi^2)^2}du, && (2.46)\\
\Longrightarrow \sigma_d &= \sigma_e. && (2.47)
\end{aligned}
$$

The interference cross section is

$$
\begin{aligned}
\sigma_i &= -\frac{K}{2}\int_{t_\pi}^{t_0}\frac{(\frac{1}{2}u-m_p^2)^2-(\frac{1}{2}s-m_p^2)^2+(\frac{1}{2}t-m_p^2)^2-4m_p^4}{(t-m_\pi^2)(u-m_\pi^2)}dt\\
&= -\frac{K}{2}\int_{4m_p^2-s}^{0}\frac{\frac{1}{2}t^2+t(\frac{1}{2}s-2m_p^2)-3m_p^4}{(t-m_\pi^2)(4m_p^2-s-t-m_\pi^2)}dt\\
&= -\frac{K}{2}\left[2m_p^2-\frac{1}{2}s+\frac{\frac{1}{8}(s+2m_\pi^2)^2-m_p^4-m_p^2(s+2m_\pi^2)}{s+2m_\pi^2-4m_p^2}ln\left(\frac{s+m_\pi^2-4m_p^2}{m_\pi^2}\right)\right] && (2.48)
\end{aligned}
$$

Therefore, the total cross section is

$$
\begin{aligned}
\sigma &= \sigma_d+\sigma_e+\sigma_i\\
&= \frac{g_{\pi NN}^4}{16\pi s(s-4m_p^2)}\left\{\frac{(s-4m_p^2)(4m_p^2-2m_\pi^2-s)}{4m_p^2-s-m_\pi^2}+2m_\pi^2 ln\left(\frac{m_\pi^2}{s+m_\pi^2-4m_p^2}\right)\right.\\
&\quad \left.-\frac{1}{4}\left[2m_p^2-\frac{1}{2}s+\frac{\frac{1}{8}(s+2m_\pi^2)^2-m_p^4-m_p^2(s+2m_\pi^2)}{s+2m_\pi^2-4m_p^2}ln\left(\frac{s+m_\pi^2-4m_p^2}{m_\pi^2}\right)\right]\right\} && (2.49)
\end{aligned}
$$

2.3 Scalar Theory: Scalar One Pion Exchange Model

A simple scalar theory presented in Griffiths [13] (often called ABC theory) provides a good check of whether or not spin is important to calculations of this kind. In this theory, only scalar fields couple to each other. The rules of this theory for elastic scattering are given below.

1. Interaction Lagrangian:

$$\mathcal{L}_{scalar} = -igAAB. \tag{2.50}$$

2. Vertex:

$$-ig. \tag{2.51}$$

3. Propagator:

$$\frac{i}{q^2 - m_\pi^2}. \tag{2.52}$$

In the above equations, A and B are scalar fields obeying the Klein-Gordon equation, g is the coupling constant, and once again, q is the exchange particles 4-momentum.

2.3.1 Invariant Amplitude

With this simple theory one can immediately write down the total invariant amplitude.

$$\mathcal{M} = \frac{g^2}{t - m_\pi^2} + \frac{g^2}{u - m_\pi^2}. \tag{2.53}$$

To compute the total cross section, square the invariant amplitude $\mathcal{M}$

$$|\mathcal{M}|^2 = \frac{g^4}{(t - m_\pi^2)^2} + \frac{g^4}{(u - m_\pi^2)^2} + \frac{2g^4}{(t - m_\pi^2)(u - m_\pi^2)}. \tag{2.54}$$

2.3.2 Cross Section

Just as was done in the case of the pseudoscalar theory, consider the terms of Equation 2.54 separately in evaluating the cross section. Similar to Equation 2.30,

$$\frac{d\sigma}{dt} = \frac{S}{16\pi\lambda_{12}}|\mathcal{M}|^2, \tag{2.55}$$

with λ_{12} being defined in Equation 2.32.

The total cross section is given by Equation 2.34 with the limits specified by Equation 2.35. Once again, the statistical factor $S = \frac{1}{2}$. Again, define a variable K to make our equations simpler.

$$\begin{aligned} K &= \frac{g^4 S}{16\pi\lambda_{12}} \\ &= \frac{g^4}{32\pi s(s-4m_p^2)}. \end{aligned} \tag{2.56}$$

The direct channel cross section (the contribution from the first term in Equation 2.54) is,

$$\begin{aligned} \sigma_d &= K\int_{t_\pi}^{t_0} \frac{1}{(t-m_\pi^2)^2}dt \\ &= \frac{K}{m_\pi^2 - t}\bigg|_{4m_p^2-s}^{0} \\ &= K\left(\frac{1}{m_\pi^2} - \frac{1}{s+m_\pi^2-4m_p^2}\right). \end{aligned} \tag{2.57}$$

Once again, it is shown that $\sigma_d = \sigma_e$. If one remembers that,

$$\begin{aligned} u &= 4m_p^2 - s - t, && (2.58)\\ du &= -dt, && (2.59)\\ t_\pi &= u_0, && (2.60)\\ t_0 &= u_\pi. && (2.61)\\ & && (2.62) \end{aligned}$$

It can once again be shown that

$$\begin{aligned} \sigma_e &= K\int_{t_\pi}^{t_0} \frac{1}{(u-m_\pi^2)^2}dt \\ &= K\int_{4m_p^2-s}^{0} \frac{1}{(u-m_\pi^2)^2}du, && (2.63)\\ \Longrightarrow \sigma_d &= \sigma_e. && (2.64) \end{aligned}$$

All that is left to do is to calculate the interference term.

$$\begin{aligned} \sigma_i &= 2K\int_{t_\pi}^{t_0} \frac{1}{(t-m_\pi^2)(u-m_\pi^2)}dt \\ &= 2K\int_{4m_p^2-s}^{0} \frac{1}{(t-m_\pi^2)(4m_p^2-s-t-m_\pi^2)}dt \\ &= \frac{2K}{s+2m_\pi^2-4m_p^2} ln\left(\frac{t+s+m_\pi^2-4m_p^2}{t-m_\pi^2}\right)\Bigg|_{4m_p^2-s}^{0} \\ &= \frac{4K}{s+2m_\pi^2-4m_p^2} ln\left(\frac{s+m_\pi^2-4m_p^2}{m_\pi^2}\right). && (2.65) \end{aligned}$$

Now the total cross section is

$$\begin{aligned}
\sigma &= \sigma_d + \sigma_e + \sigma_i \qquad (2.66)\\
&= 2K\left[\frac{1}{m_\pi^2} - \frac{1}{s+m_\pi^2-4m_p^2}\right.\\
&\quad \left. + \frac{2}{s+2m_\pi^2-4m_p^2} ln\left(\frac{s+m_\pi^2-4m_p^2}{m_\pi^2}\right)\right]\\
&= \frac{g^4}{16\pi s(s-4m_p^2)}\left[\frac{1}{m_\pi^2} - \frac{1}{s+m_\pi^2-4m_p^2}\right.\\
&\quad \left. + \frac{2}{s+2m_\pi^2-4m_p^2} ln\left(\frac{s+m_\pi^2-4m_p^2}{m_\pi^2}\right)\right]. \qquad (2.67)
\end{aligned}$$

2.4 Total Cross Section in the Asymptotic Region

Now that the total cross sections for both the scalar theory (Equation 2.67) and the OPEM (Equation 2.49) have been calculated, the theoretical cross section are investigated to make sure that they do not have any odd behavior that may cause problems when the cross sections are used in computer codes such as MESTRN. The first thing to examine is the limit of the cross section as s approaches its minimum value of $4m_p^2$. The scalar theory gives:

$$\lim_{s\to 4m_p^2} \sigma_{scalar} = \frac{3g^4}{64\pi m_p^2 m_\pi^4}. \qquad (2.68)$$

While the OPEM gives:

$$\lim_{s\to 4m_p^2} \sigma_{OPEM} = \frac{g^4(m_\pi^4+6m_p^4)}{1024 m_p^2 m_\pi^4}. \qquad (2.69)$$

From both a physical understanding viewpoint and an applications perspective the cross section must be well behaved in order to have physical meaning and application. In this case, both models are finite at threshold energy.

The cross sections should also obey the Froissart bound [17] which states that

$$\lim_{s\to\infty} \sigma_{total} < c(log[s])^2, \tag{2.70}$$

where c is a constant and σ_{total} is the total cross section (elastic plus inelastic). Now compute the limits of the cross sections as $s \to \infty$. The scalar theory gives

$$\lim_{s\to\infty} \sigma_{scalar} = 0, \tag{2.71}$$

and the OPEM model gives

$$\lim_{s\to\infty} \sigma_{OPEM} = 0. \tag{2.72}$$

While the Froissart bound applies to the inelastic plus the elastic cross section, it is still a good test of the physical validity of our theories. Both the OPEM and the scalar model elastic cross sections obey the Froissart bound (see Figure C.1).

The result that in the limit of large s the theoretical cross sections go to zero is not surprising. As the energy increases, the colliding particles approach more closely and the likelihood of an inelastic reaction occurring becomes more likely.

2.5 Comparison of the Models

Now that the models have been developed, they need to be compared to data to determine their usefulness. To do this, the coupling constant is left as a free parameter and fitted the value of the theoretical curve to the data at one point. When the scalar theory is compared to the pseudoscalar theory, over all energy ranges and for the majority of the data sets, the scalar theory is the better fit (see Figures C.1–C.38). This is especially true for the invariant differential cross sections in the region of t close to zero, as will be discussed below. In general, the pseudoscalar pion exchange of the OPEM tends to severely underestimate the invariant differential cross section in this region. While the

scalar theory fits the data well in this region, as t approaches 0 it tends to overestimate the data (see below).

As another test of how well these theories fit the data, a simple parameterization [18] is also introduced. For the total cross section the Bertsch parameterization gives:

$$\begin{aligned} \sigma(\sqrt{s}) &= 55 && if\ \sqrt{s} < 1.8993\,\text{GeV} \\ &= \frac{35}{1+200(s-1.8993)} + 20 && if\ \sqrt{s} > 1.8993\,\text{GeV}, \end{aligned} \tag{2.73}$$

and for the invariant differential cross section it gives

$$\frac{d\sigma}{dt} = ae^{bt}, \tag{2.74}$$

where b is defined as

$$b(\sqrt{s}) = \frac{6(3.65(\sqrt{s}-1.866))^6}{1+(3.65(\sqrt{s}-1.866))^6}, \tag{2.75}$$

and the variable a is taken as a parameter that is used to fit to the data.

2.5.1 Total Cross Section

An overall view of the total cross section curves, along with experimental data from the Particle Data Group [19] in the momentum range of 0 to 10 GeV is shown in Figure C.2. Figure C.2 shows the OPEM and the scalar model providing a good fit to the data in the low energy region. As will be discussed in the next section, the scalar theory does an excellent job of fitting the data in this region. As the momentum increases, the OPEM and the scalar theory fall off too quickly to represent the experimental data well when using a coupling constant appropriate for low momentum. A discussion of this is presented below.

Figure C.3 illustrates that the scalar and pseudoscalar pion exchange models fit the data well below approximately .5 GeV. The scalar theory does a slightly better job com-

pared to the OPEM for this momentum range. When the incident lab momentum, $p_{lab} > .5$ GeV the theoretical curves fall off very quickly compared to the data. In the .5 GeV to 1 GeV momentum range both models begin to slightly underestimate the data. The parameterization of Bertsch [18] (labeled as Bertsch on the graphs) works well for $1\ GeV\ >\ p_{lab}\ >\ .5$ GeV but is definitely not appropriate below .5 GeV since it has a discontinuity at $p_{lab} = .3003$ GeV and underestimates the cross section in this region significantly. This can be seen in Figure C.3.

As the incident particle momentum in the lab frame increases, the theoretical curves for the OPEM and scalar model are shown to both be poor representations of the data. This is partially due to the decaying functional form of the model cross sections. In the lab momentum range of 1 to 2 GeV the Bertsch parameterization works well.

As the lab momentum is increased further the Bertsch parameterization begins to overestimate the data. This behavior begins in the 2 to 5 GeV region. It is at this point that the relative error of the Bertsch parameterization begins to increase steadily to approximately 100% for the entire momentum range of 5 GeV to 50 GeV, while the OPEM and scalar model both underestimate the data. This signals the failure of the models and indicates the need for a more complex theory to account for the larger cross section in this momentum range. The failure of the models at high energies is not a suprise. Any theory based solely on the exchange of a pion should begin to fail at higher energies as heavier exchange particles become more important.

The Coupling Constants

As was shown in Figure C.2, the coupling constant used to fit in the very low momentum region does not fit the experimental data at higher momentum. Using the momentum ranges of 1–2 GeV, 2–10 GeV and 10–50 GeV, the coupling constant for both the OPEM and the scalar model were varied to determine if the data could be broken up into momentum regions and ascertain whether different coupling constants could be used to reproduce the data in these regions. This is shown in Figures C.4–C.6. In general it was found that

increasing the coupling constant of either theory led to the exaggeration of the curvature of the theoretic cross section. This is due to the coupling constant being a multiplicative variable in the cross section formulas. So increasing the coupling constant has the feature of shifting the curves up slightly, but due to the quick decay of the cross section, simply changing the coupling constant is not enough to produce exact fits to the data.

In Figure C.4, the data seems to be approximately constant over the momentum range. The theoretic models, however, have decreasing slope. The increased coupling constant fits the data much better than the one used in the very low momentum region for both theories, but does not have the correct slope.

Figure C.5 shows that the OPEM actually does a very good job of fitting the data with a coupling constant value of 11.5. The scalar theory does a decent job also, but the curve falls off faster than the OPEM does.

In the 10 to 50 GeV range (Figure C.6), the experimental cross section becomes constant again and both theories fall off too quickly with increasing momentum to fit the data precisely.

2.5.2 Invariant Differential Cross Section

In Figures C.7–C.38, the invariant differential cross section ($\frac{d\sigma}{dt}$) data collected by different experiments is presented and compared to our models and the parametrization. For each momentum value, a unique coupling constant was fit to the data for each of the different theories and for the Bertsch parameterization. It is important to note that the coupling constant for the scalar theory has dimensions of energy while the coupling constant of the OPEM is dimensionless and an analysis of the coupling constants was not preformed.

Albrow *et al.*, **1970**

For Figures C.7–C.9, data was taken from Albrow, *et al.* [20] at 3 different momenta. At $p_{lab} = 1.118$ GeV (Figure C.7) the theoretical curves, especially the OPEM theory, work quite well. The OPEM fits the data at this momentum very well with only a few percent

error for the majority of the data points. As the incident lab momentum is increased to 1.38 GeV (Figure C.8), the scalar theory becomes a slightly better fit than the OPEM, while the Bertsch parameterization is a relatively poor fit. At $p_{lab} = 2.74$ GeV (Figure C.9), the fit to the data is better for the Bertsch parameterization than the theoretical curves.

Dobrovolsky *et al.*, 1988

For the data taken from Dobrovolsky, *et al.* [21], which are all at low momentum (1.39 GeV to 1.68 GeV) and correspond to values of t very close to zero, the Bertsch parameterization is the best fit to the data. This is shown in Figures C.10–C.13. The slopes of the two theoretical curves are too steep to fit the data well in these regions very well.

Jenkins *et al.*, 1980

In Figures C.14–C.21, the data of Jenkins *et al.* [22] with a momentum range of 1.896 GeV to 8.022 GeV are compared with the 3 curves. One thing to note is that as t approaches zero, the differential cross section should increase [22] and therefore the data points that fall off as t approaches zero should be disregarded. With this in mind, over the whole momentum range the scalar theory fits the data the best. The slope of the Bertsch parameterization is too steep to fit the data well over the whole range of t. The OPEM does fit the data well in the region further away from zero. The scalar theory does a very good job of fitting the data. The only area where it seems to have some problems is at the lowest momentum, where it tends to underestimate the cross section data.

Ambats *et al.*, 1974

In Figures C.22–C.25, the data was taken from Ambats, *et al.* [23] and is in the momentum range of 3.00 GeV to 6.00 GeV. This data was taken over a wide range of t values. As t approaches zero, for all values of momentum in these data sets, the curves fall away from the data fairly significantly. At approximately $t > -.5$ GeV^2, the OPEM begins

to increasingly underestimate the data. As t continues to get closer to zero, the scalar theory starts to overestimate the cross section while the parameterization of Bertsch tends to underestimate. This trend is true across the entire data set. Notice that at values of t away from zero the scalar theory does a very good job of fitting the data. This can especially be seen in Figures C.23–C.25.

Baglin *et al.*, 1975

At a lab momentum of 9 GeV, the data of Baglin *et al.* [24] are used in Figure C.26. The theoretical curves of the scalar theory and OPEM both fail when fit to this data set. As has been seen in previous data sets, the OPEM does not start rising in value until too close to zero to be able to fit the data well. In the case of the scalar theory, it does not have a steep enough slope to fit the data well but still gives a good general trend for the data. The Bertsch parameterization does a good job in the steeply increasing section near $t = -1$ GeV^2 but underestimates the cross section in the region $t < -1$ GeV^2.

Brandenburg *et al.*, 1975

When the 3 curves are plotted against the data presented by Brandenburg *et al.* [25] (Figure C.27), the data is fit well by both the scalar theory and the Bertsch parameterization. This experimental data was taken at $p_{lab} = 10.4$ GeV. The OPEM severely underestimates in the t range close to zero. Figure C.27 is another instance of the scalar theory being a good fit to the differential cross section data except in the t range close to zero. Surprisingly, the scalar theory does a fairly good job fitting the data in the t range far from zero.

Beznogikh *et al.*, 1973

The data gathered by Beznogikh *et al.* [26] is presented in Figures C.28–C.34. This data was spanned the momentum range of 9.43 GeV to 30.45 GeV. The t values for this data set were all very close to zero. All the curves follow the general trend of the data. For one set

(p_{lab} = 13.16 GeV, Figure C.29) the OPEM seems to do well, but overall the theoretical curves and the Bertsch parameterization are poor fits. This follows the general trend of the curves to not fit the data well in the region of t close to zero.

Edelstein *et al.*, 1972

In Figures C.35 to C.38, the data gathered by Edelstein *et al.* [27] was compared with the theoretical curves and the Bertsch parameterization. That data was at higher momentum (9.9 GeV to 29.7 GeV) where the theoretical models are not thought to be valid. This data set spans a much larger t range than the Beznogikh data set and was used to determine how well the theoretical models are doing overall at higher momentum. Surprisingly, the scalar theory does a very good job fitting the data all the way up to p_{lab} = 29.7 GeV, as shown in Figure C.38. The OPEM continues the general trend of doing well in the t range far from zero but severely underestimates the experimental cross section in the t region close to zero.

2.6 Conclusions

Two quantum field theoretic models of proton-proton elastic scattering were presented. One model, the one pion exchange model, contained full spin and isospin dependence, while the other model was based solely on scalar fields. The models were used to develop total and invariant differential cross sections that were then compared to data and a simple parametrization.

When the models were compared to the total cross section data available it was found that the scalar theory was the best fit to the data below lab momentum of .5 GeV. This is a nice finding since the scalar theory is very simple. Above a lab momentum of 3 GeV, both the theories and the Bertsch parameterization do poorly as fits to the total cross section data using the same coupling constant that was used in the very low momentum region. Increasing the coupling constant was found to give a better fit. The fit to the data, however, is not as good as was found in the very low momentum region.

For the invariant differential cross section data, the analysis is slightly more tricky. The data of 7 papers was presented and the models were compared to the data, which included a laboratory momentum range of 1.38 GeV to 30.45 GeV. Over the complete set of data that was investigated, the OPEM was the poorest fit. The scalar model and the Bertsch parameterization fit the data very well, until t approached zero (corresponding to the center of mass angle approaching zero). In the t close to zero range, the scalar theory tended to overestimate the data while the Bertsch parameterization underestimated. They both had a comparable error until the data came very close to zero, where the scalar theory tended to severely overestimate the data. The models began to fail when the laboratory momentum reached approximately 10 GeV.

With this analysis complete, the use of the OPEM by itself as the basis of the physics of proton-proton elastic scattering used in a radiation transport code (*i.e.* MESTRN) can be ruled out by the fact that in the regions in which it does work well, the scalar model does a better job of fitting the data. There is hope, however, that a more robust theory which includes heavier boson exchanges may make up for the failure of the OPEM. On the other hand, the scalar theory, is the best model for total cross section in the momentum range below .5 GeV and can be used as a physical model of proton-proton elastic scattering.

For the case of the invariant differential cross section, the scalar model was the overall best fit to the data. The Bertsch parameterization has a major downfall in this case. Figure C.39 shows the curves corresponding to the two theoretical models and the Bertsch parameterization plotted over the full physical region of t. The two theoretical models show the classic shape of two body differential cross sections (similar to Rutherford scattering), while the parametrization displays a simple exponential curve. This is disappointing considering the Bertsch parameterization is the best fit overall to all the data investigated in this paper. The scalar theory does a good job of fitting the data but overestimates in the t close to zero region. The scalar theory was found to have the surprising result of fitting the differential data well at much higher incident momentum than would be expected of a simple scalar theory. The OPEM is a much poorer fit compared to the scalar theory as

a general rule.

There is another subtlety associated with using the invariant differential cross sections of this paper in a transport code like MESTRN. The coupling constants were used as a free parameter to fit the data. The coupling constants were all found to vary with the laboratory momentum of the incident particle. This fitting procedure allows the cross sections to only be calculated at the lowest order. The coupling constant then simulates the additional information contained in the higher order diagrams in the perturbation series. A detailed analysis would have to be performed to determine how the coupling constant should vary to achieve the best fit to the data over the entire physical momentum range.

In conclusion, the first step towards using cross sections based on physical interactions in NASA's radiation transport code MESTRN has begun with the investigation of proton-proton elastic scattering. It was found that a simple scalar model works very well in the low energy region when considering the total cross section and that more work needs to be done in the high energy region to develop a physical model the fits the data well. The GCR spectrum ranges from about 100 MeV to 10 EeV ($10^{20}eV$), with the majority of the flux contained in the 100 MeV to 10 GeV region [9, 10]. There is no single theory that gives calculable cross sections for the 100 MeV to 10 GeV energy region of high flux, let alone the entire 12 orders of magnitude spanned by the complete GCR spectrum.

Future work will require the development of cross sections for other fundamental processes based on physical models. In addition, production of particles from intermediate resonance states must be investigated to obtain accurate cross sections, especially for pion production.

Chapter 3

A Comparison of Δ-resonance Production

3.1 Introduction

Motivated by the importance of nucleon resonances to the dynamics of heavy-ion collisions [28–32] the validity of two widely used models of Δ-resonance production [2, 3] are investigated and compared to a simplified model presented herein. Most models of heavy-ion collisions are based on fundamental nucleon-nucleon collisions with in-medium effects taken into account. The Δ-resonance, being the lightest of the nucleon resonances, is the most easily excited and therefore, the most abundantly produced. With this in mind, I investigate the validity of currently accepted models of nucleon-nucleon scattering producing one or two Δ-resonances.

The Δ-resonance is the first excited state of the nucleon. It is a spin $\frac{3}{2}$, isospin $\frac{3}{2}$ state which corresponds to a $\Delta S = \Delta T = 1$ spin-isospin excitation with an excitation energy of about 300 MeV. Its dominant decay products are $N\pi$.

From a quark model perspective, the excitation of a Δ-resonance from a nucleon corresponds to a spin and isospin flip of a quark in the nucleon. For example:

$$p(u\uparrow u\uparrow d\downarrow)+p(u\uparrow u\uparrow d\downarrow)\rightarrow\Delta^{++}(u\uparrow u\uparrow u\uparrow)+n(d\downarrow u\uparrow d\downarrow). \tag{3.1}$$

The Δ also plays a very important role in the production of mesons in elementary particle physics. In fact, the Δ-resonance was known to play an important role in pion production as early as 1958 when Mandelstam introduced his resonance model for pion production [33]. Mandelstam showed that close to threshold, pion production from an intermediate Δ-resonance state (shown below) can account for the total pion production cross section.

$$N+N\rightarrow N+\Delta\rightarrow N+N+\pi. \tag{3.2}$$

In addition to producing pions, the Δ-resonance may also have a role in the production of ρ mesons, kaons, N^*-resonances and in the production of strange baryons that accompany the production of kaons [19].

With Δ-resonance standing on important physical ground, I wanted to investigate the state of the art in the theory of Δ-resonance production and how it compares to experimental data.

3.2 Meson Exchange Models

The three models used in this analysis are a scalar one pion exchange model (SOPEM), the one pion exchange model (OPEM) of Dmitriev *et al.* [3] and the one boson exchange model (OBEM) of Huber & Aichelin [2]. The SOPEM is introduced in Section 3.2.1 and the OPEM of Dmitriev *et al.* and the OBEM of Huber & Aichelin [2] are briefly discussed in Sections 3.2.2 and 3.2.3, respectively.

3.2.1 SOPEM

As a comparison to the well-established physics models, I decided to investigate how well a simplified OPEM would work. In this model, all the particles are treated as scalar fields. The application of this work to deterministic radiation transport codes used in space radiation protection analysis requires simple cross section formulas to minimize computational time. The use of a simple model to obtain a simple cross section formula seemed like a reasonable starting place.

The interaction Lagrangians for the scalar one pion exchange model are presented below:

$$\mathcal{L}_{\pi NN} = -ig_{\pi NN}\phi_\pi\phi_N\phi_N, \tag{3.3}$$

$$\mathcal{L}_{\pi N\Delta} = -ig_{\pi N\Delta}\phi_\pi\phi_N\phi_\Delta. \tag{3.4}$$

Where $g_{\pi NN}$ and $g_{\pi N\Delta}$ are the coupling constants and ϕ_x is a scalar field obeying the Klein-Gordon equation with the mass specified by the physical mass of particle x.

With this simple scalar theory one can immediately determine the invariant amplitude for a given process, shown below:

$$\mathcal{M} = \frac{g_{\pi N\Delta}g_{\pi NN}}{t-m_\pi^2} + \frac{g_{\pi N\Delta}g_{\pi NN}}{u-m_\pi^2}, \tag{3.5}$$

$$\mathcal{M} = \frac{g_{\pi N\Delta}^2}{t-m_\pi^2} + \frac{g_{\pi N\Delta}^2}{u-m_\pi^2}. \tag{3.6}$$

Where, Eq. 3.5 applies to reactions of the form $NN \to N\Delta$ and Eq. 3.6 applies to $NN \to \Delta\Delta$.

Once the invariant amplitude is computed the differential cross section can be obtained for the reactions of interest using:

$$\frac{d\sigma}{dt} = \frac{S}{16\pi\lambda_{12}}|\mathcal{M}|^2, \tag{3.7}$$

with

$$\lambda_{ij} \equiv (s - m_i^2 - m_j^2)^2 - 4m_i^2 m_j^2. \tag{3.8}$$

Where s is the center of mass energy squared, t is the Mandelstam variable corresponding to the momentum transferred in the reaction and S is a statistical factor given by $\frac{1}{j!}$ for j identical particles in the final state.

To obtain the total cross section, the differential cross section is intgrated from t_π to t_0. The limits of integration for a reaction of the form $1 + 2 \rightarrow 3 + 4$ are (see Appendix B):

$$t_{\frac{\pi}{0}} = \frac{1}{4s}\left[(m_1^2 - m_2^2 - m_3^2 + m_4^2)^2 - (\sqrt{\lambda_{12}} \pm \sqrt{\lambda_{34}})^2\right]. \tag{3.9}$$

The integral can be computed analytically and the total cross section is then:

$$\begin{aligned}\sigma = \frac{S g_{\pi NN}^2 g_{\pi N\Delta}^2}{16\pi\lambda_{12}}\Bigg(&\frac{2}{m_\pi^2 - t_0} - \frac{2}{m_\pi^2 - t_\pi} + \frac{1}{s + 2m_\pi^2 - \sum_i m_i^2} \\ &\times Log\left[\frac{(t_\pi - m_\pi^2)(t_0 + s - \sum_i m_i^2 + m_\pi^2)}{(t_0 - m_\pi^2)(t_\pi + s - \sum_i m_i^2 + m_\pi^2)}\right]\Bigg),\end{aligned} \tag{3.10}$$

where $\sum_i m_i^2$ is the sum of all the masses of the particles involved in the reaction.

To take into account the fact that the Δ-resonance is an unstable particle in an intermediate state in reactions of the form of Eq. 3.2, the mass of the Δ-resonance is allowed to vary and is integrated over. For single Δ-resonance production it takes the form:

$$\sigma = \int \sigma(\mu)\rho(\mu^2)d\mu^2, \tag{3.11}$$

with

$$\rho(\mu^2) = \frac{1}{\pi}\frac{m_\Delta \Gamma}{(\mu^2 - m_\Delta^2)^2 + m_\Delta^2\Gamma^2}. \tag{3.12}$$

Where μ is the varying mass of the Δ-resonance , m_Δ is the physical mass of the Δ-resonance (1.232 GeV [19]). Γ is the decay width (.120 GeV [19]). The limits of the integral in Eq. 3.11 are found from conservation of energy and momentum. To derive the maximum value of μ for a reaction of the type $1 + 2 \rightarrow 3 + 4$, where particle 4 is taken to be the Δ-resonance, use the Mandelstam variable s:

$$s \equiv (p_1 + p_2)^2 = (p_3 + p_4)^2 \tag{3.13}$$

$$= m_3^2 + m_4^2 + 2E_3E_4 - 2\boldsymbol{p}_3 \cdot \boldsymbol{p}_4. \tag{3.14}$$

For a given s, m_4^2 is maximum when $p_3 = p_4 = 0$ and all the energy and momentum of particles 1 and 2 goes into the mass of particles 3 and 4 ($E_3 = m_3$ and $E_4 = m_4$):

$$s = (m_3 + m_4)^2, \tag{3.15}$$

which gives a maximum value of:

$$\mu_{max} = m_{4,max} = \sqrt{s} - m_3. \tag{3.16}$$

Since the Δ-resonance is an unstable particle, the minimum value of m_4 must be the sum of the masses of its decay products. In the case of the Δ-resonance , it decays to πN with a branching ratio of greater than .99 [19]. Therefore the minimum value of m_4 is:

$$\mu_{min} \quad = \quad m_{4,min} = m_N + m_\pi. \tag{3.17}$$

In the case of two Δ-resonances in the final state (particles 3 and 4 are Δs), an additional integral over the varying Δ-resonance mass is needed in Eq. 3.11. It then becomes:

$$\sigma \quad = \quad \int\int \sigma(\mu_3, \mu_4)\rho(\mu_3^2)\rho(\mu_4^2)d\mu_4^2 d\mu_3^2. \tag{3.18}$$

With the limits of integration given as:

$$m_N + m_\pi \leq \quad \mu_3 \quad \leq \sqrt{s} - \mu_4, \tag{3.19}$$

$$m_N + m_\pi \leq \quad \mu_4 \quad \leq \sqrt{s} - m_N - m_\pi. \tag{3.20}$$

The minimum values of Eqs. 3.19 and 3.20 are simply the sum of the masses of the decay products once again. The maximum values are interdependent. The maximum value of μ_4 is the available energy of the reaction ($\sqrt{s}$) minus the minimum value of μ_3. The maximum value of μ_3 is the available energy of the reaction minus the amount used (μ_4).

3.2.2 OPEM of Dmitriev *et al.*

In the OPEM, a virtual pion is used to mediate the force between two interacting hadrons. The Lagrangians for the pion interacting with nucleons and Δ-resonances are given below:

$$\mathcal{L}_{\pi NN} = \frac{f_{\pi NN}}{m_\pi}\bar{\Psi}\gamma_\mu\gamma_5\boldsymbol{\tau}\Psi\partial_\mu\boldsymbol{\pi}, \tag{3.21}$$

$$\mathcal{L}_{\pi N\Delta} = \frac{f_{\pi N\Delta}}{m_\pi}\bar{\Delta}_\mu\boldsymbol{T}\Psi\partial_\mu\boldsymbol{\pi} + h.c. \tag{3.22}$$

Where Ψ is the nucleon field, Δ_μ is the Rarita-Schwinger field for the Δ-resonance and π is the pion field. τ are the usual Pauli isospin matrices and T is the transition isospin operator that takes isospin $\frac{1}{2} \rightarrow \frac{3}{2}$. $f_{\pi NN}$ and $f_{\pi N\Delta}$ are the pseudovector coupling constants for the pion-nucleon-nucleon and pion-nucleon-delta vertexes respectively.

In the Dmitriev *et al.* version of the OPEM they introduce a simple form factor in the vertices [3]:

$$F(t) = \frac{\Lambda^2 - m_\pi^2}{\Lambda^2 - t}. \tag{3.23}$$

Λ is a parameter and t is the Mandelstam variable corresponding to the transferred 4-momentum squared. This form factor is used to take into account the off-mass-shell behavior of the exchanged pion. In addition, the finite width of the Δ-resonance and the possibility for it being off-mass-shell are also addressed in Dmitriev *et al.* and the reader is referred to the original paper for further discussion.

3.2.3 OBEM of Huber & Aichelin

The OPEM was found to work well, but it did not account for some phenomena observed in the basic nucleon-nucleon interaction [15]. This lead some researchers to consider the exchange of other mesons in addition to the pion and thus the one boson exchange model came into existence. The one boson exchange model (OBEM) is very similar to the OPEM,

but the introduction of different virtual mesons as exchange particles leads to richer and more complex interactions.

The model discussed here is the OBEM presented by Huber & Aichelin in 1994 [2]. The interaction Lagrangians are presented below:

$$\mathcal{L}_{\pi NN} = -ig_{\pi NN}\bar{\Psi}\gamma_5\boldsymbol{\tau}\boldsymbol{\pi}\Psi, \tag{3.24}$$

$$\mathcal{L}_{\pi N\Delta} = \frac{g_{\pi N\Delta}}{m_\pi}\bar{\Delta}_\mu\boldsymbol{T}\Psi\partial_\mu\boldsymbol{\pi} + h.c., \tag{3.25}$$

$$\mathcal{L}_{\rho NN} = -g_{\rho NN}\bar{\Psi}\gamma_\mu\boldsymbol{\tau}\boldsymbol{\rho}^\mu\Psi - \frac{f_{\rho NN}}{2m_N}\bar{\Psi}\sigma_{\nu\mu}\partial^\nu\boldsymbol{\tau}\boldsymbol{\rho}^\mu\Psi, \tag{3.26}$$

$$\mathcal{L}_{\rho N\Delta} = i\frac{g_{\rho N\Delta}}{m_N + m_\rho}\bar{\Delta}_\mu\boldsymbol{T}(\partial^\nu\boldsymbol{\rho}^\mu - \partial^\mu\boldsymbol{\rho}^\nu)\gamma_\nu\gamma_5\Psi + h.c. \tag{3.27}$$

In the above equations Ψ is the nucleon field, Δ_μ is the Rarita-Schwinger field for the Δ-resonance and π is the pion field. $\boldsymbol{\tau}$ are the usual Pauli isospin matrices and $\boldsymbol{T}$ is the transition isospin operator that takes isospin $\frac{1}{2} \rightarrow \frac{3}{2}$. $g_{\pi NN}$ and $g_{\pi N\Delta}$ are the pseudoscalar coupling constants for the pion-nucleon-nucleon and pion-nucleon-delta vertexes respectively. $\boldsymbol{\rho}^\mu$ is the field for the vector meson ρ. Due to the pseudovector nature of the Δ-resonance only isospin-1 mesons can couple to the $N\Delta$ vertex. Since ρ is a vector particle, it can couple as both a vector and a tensor with different coupling constants as shown in Eq. 3.26. The term $\sigma_{\nu\mu}$ that appears in the tensor coupling term is defined as:

$$\sigma_{\nu\mu} \equiv \frac{1}{2}i(\gamma_\nu\gamma_\mu - \gamma_\mu\gamma_\nu). \tag{3.28}$$

Huber & Aichelin choose a parameterization of the vertex form factor which is shown below:

$$F(Q^2) = \frac{\Lambda^2}{\Lambda^2 - Q^2}. \tag{3.29}$$

Q is the 4-momentum of the exchanged meson and Λ is the parameter. This form factor is used to take into account the off mass-shell behavior of the exchanged particle.

Due to the complexity of the final results for the cross sections within this model, the authors give simple parameterizations of the cross sections. Once again, the reader is referred to the original paper for more detail.

3.3 Single Δ-resonance Production

As a test of the validity of the models of single Δ-resonance production, the three models were compared to available experimental data for reactions of the form $NN \rightarrow N\Delta$. The threshold incident laboratory momentum for these types of reactions is about 1.26 GeV. Because much of the data was inferred from single pion production reactions, subthreshold data is included in this analysis.

To obtain the total cross section for reactions of the $NN \rightarrow N\Delta$ in the case of the Dmitriev *et al.* OPEM model, the differential cross section presented in the original 1986 paper [3] was numerically integrated. For the Huber & Aichelin OBEM, the parameterizations given in the 1994 [2] paper were used. For both the OPEM and OBEM, values for any parameters of the model were taken directly from the published article. For the scalar one pion exchange model, Eq. 3.11 with the appropriate masses was used. The coupling constant for the pion-nucleon-delta interaction ($g_{\pi N\Delta}$) was left as a free parameter and fitted to the data, while the coupling constant for the pion-nucleon-nucleon interaction had the value of $g_{\pi NN} = 13.553$.

3.3.1 $pp \rightarrow n\Delta^{++}$

Fig. 3.1 shows the three models compared to the experimental data. Overall, all three models follow the general trend of the data. The OPEM of Dmitriev *et al.* seems to consistently over estimate the data.

Near the peak of the data (see Fig. 3.1), one can see that the SOPEM fits the data very well, but does not have a steep enough slope after the peak resulting in a small deviation

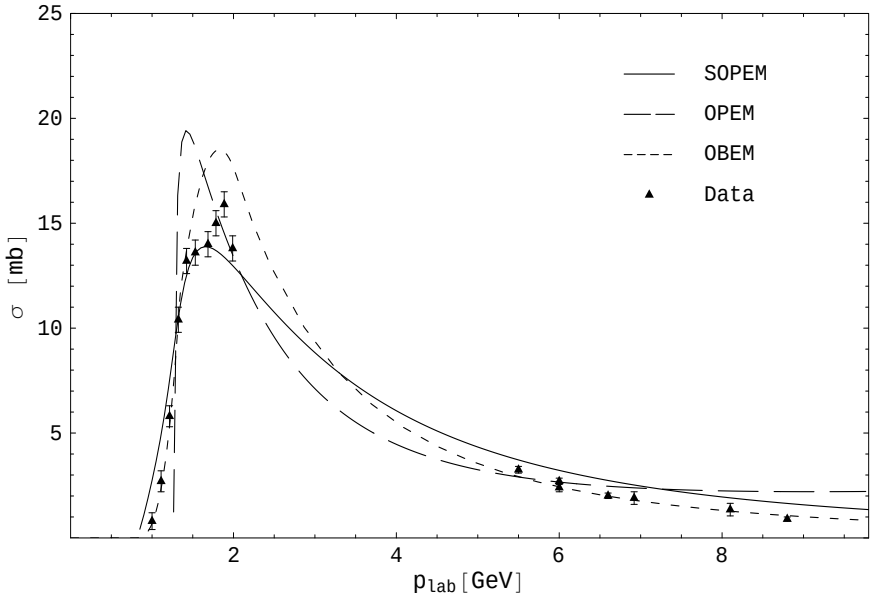

Figure 3.1: Comparison of the scalar one pion exchange model (SOPEM), the OPEM of Dmitriev *et al.* [3] and the OBEM of Huber & Aichelin [2] to experimental data [34–43] for the reaction $pp \to n\Delta^{++}$.

from the data. A value of $g_{\pi N\Delta} = 1.88$ was used for this data. The Huber & Aichelin OBEM, on the other hand, fits the data very well after the peak in the cross section, but gives a slightly too large cross section in the region near the peak. The OPEM of Dmitriev *et al.* predicts a peak cross section too large and at too low of momentum compared to the experimental data.

Fig. 3.2 shows the high momentum data plotted with the SOPEM using a coupling constant of $g_{\pi N\Delta} = 2.0449$. In the 1994 paper by Huber & Aichelin [2], the authors only define their parameterizations up to $\sqrt{s} = 4.50$ GeV ($p_{lab} \approx 9.8$ GeV). In all of our analyses, the parameterizations were extended beyond this point. If the parametrization becomes negative, the value of the model was not used in the analysis. As shown in Fig. 3.2, the SOPEM matches the data well in this large momentum range. The model of Dmitriev *et al.* is not included in this graph. The total cross section obtained from their model begins to increase with increasing incident lab momentum near $p_{lab} = 12$ GeV. This behavior is due to the invariant amplitude of the exchange diagram for one pion exchange

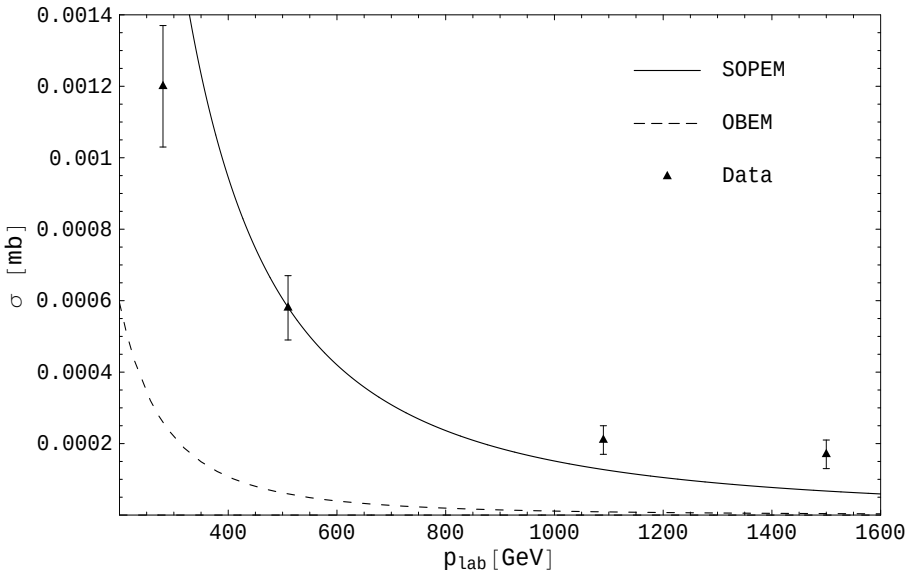

Figure 3.2: Comparison of the scalar one pion exchange model (SOPEM) and the OBEM of Huber & Aichelin [2] to experimental data [34–43] for the reaction $pp \to n\Delta^{++}$ at high incident momentum.

being proportional to p_{lab} at large momentum.

3.3.2 $pp \to p\Delta^+$

20 data points were found for the $pp \to p\Delta^+$ reaction with which to compare the models. Fig. 3.3 shows the Huber & Aichelin OBEM once again overpredict the peak of the data, while the SOPEM is able to fit the data in the peak very well using a coupling constant of $g_{\pi N\Delta} = 1.9789$. In addition, the tendency of the OPEM of Dmitriev *et al.* continues to give a peak cross section that is too large and a peak at too low of momentum compared to the experimental data. The SOPEM is the better fit to the experimental data for this reaction over the whole data set.

3.3.3 $pn \to p\Delta^0$

Fig. 3.4 shows the results for the reaction $pn \to p\Delta^0$. The available data for this reaction was significantly smaller than the other single Δ-resonance production reactions with only

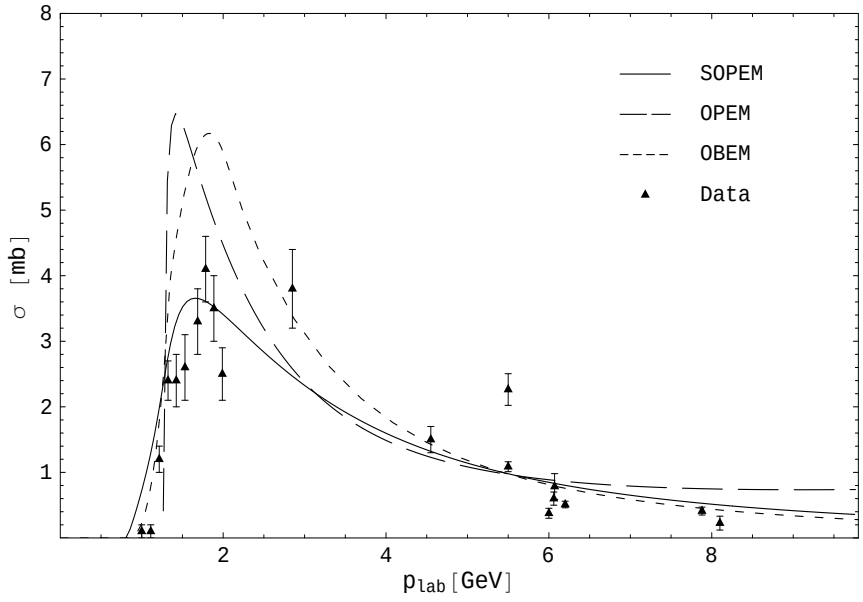

Figure 3.3: Comparison of the scalar one pion exchange model (SOPEM), the OPEM of Dmitriev *et al.* [3] and the OBEM of Huber & Aichelin [2] to experimental data [27,34,43–45] for the reaction $pp \to p\Delta^+$.

8 data points found. The trend of the other reactions continues with both the SOPEM and the OBEM of Huber & Aichelin doing fairly well over the entire data set. The Huber & Aichelin OBEM is the better overall fit, while the SOPEM is the better in the peak region of the cross section and the Dmitriev *et al.* OPEM continues to be the poorest representation of the experimental cross sections. For this reaction, the SOPEM was found to work best with a coupling constant of $g_{\pi N\Delta} = 2.1768$.

3.3.4 Overall Analysis

Table 3.1 shows the results of a χ^2 analysis of the theoretical models and experimental data. As the graphs showed, the Huber & Aichelin OBEM is the better fit to the data for all but the $pp \to p\Delta^+$ reaction, where the SOPEM is the best. Overall, the SOPEM does a better job of fitting the data in the threshold to 5 GeV momentum range. This momentum range is important because the peak in the experimental cross sections occurs at a lab momentum of about 2 GeV.

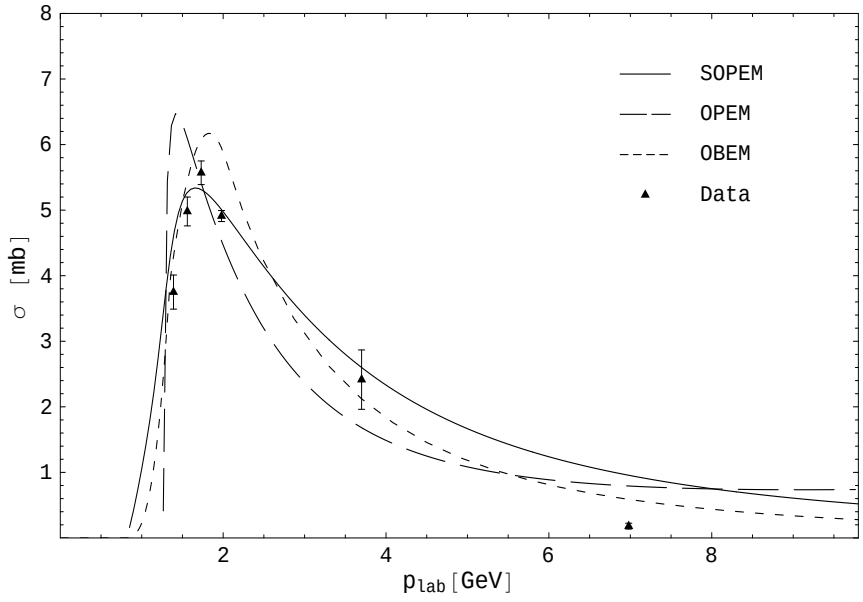

Figure 3.4: Comparison of the scalar one pion exchange model (SOPEM), the OPEM of Dmitriev *et al.* [3] and the OBEM of Huber & Aichelin [2] to experimental data [34, 46, 47] for the reaction $pn \to p\Delta^0$.

3.4 Double Δ-resonance Production

Next, the production of two Δ-resonances in reactions of the form $NN \to \Delta\Delta$ is investigated. Only the Huber & Aichelin OBEM and the SOPEM will be considered since the OPEM of Dmitriev *et al.* is only used for single Δ-resonance production. The threshold momentum for reactions of this type is about 2.09 GeV. Overall, there is a only a small amount of experimental data available for comparison.

3.4.1 $pp \to \Delta^{++}\Delta^0$

For the reaction $pp \to \Delta^{++}\Delta^0$, 11 experimental data points were found [34,48–50]. Fig. 3.5 shows the two models compared to the data at low incident momentum. The Huber & Aichelin OBEM severely underpredicts the maximum value of the experimental data, while the SOPEM has a maximum value closer to the maximum value of the data. The coupling constant for the pion-nucleon-delta interaction were once again fitted to the data. For this

Table 3.1: χ^2 per degree of freedom analysis for $NN \rightarrow N\Delta$ reactions

		χ^2 **per degree of freedom**	
Reaction	**Model**	**up to 9.8 GeV**	p_{lab} **up to 5 GeV**
$pp \rightarrow n\Delta^{++}$	SOPEM	13.2	4.2
	OBEM	9.7	15.4
	OPEM	38.1	47.4
$pp \rightarrow p\Delta^{+}$	SOPEM	19.0	5.9
	OBEM	18.4	24.2
	OPEM	31.1	42.0
$pn \rightarrow p\Delta^{0}$	SOPEM	68.3	2.5
	OBEM	42.2	34.0
	OPEM	57.2	38.9

data set we used a value of $g_{\pi N\Delta} = 5.5937$. Both models peak approximately 3 GeV too low in incident momentum to match the peak in the experimental data well.

In Fig. 3.6, the high momentum data is presented along with the SOPEM using the coupling constant fit to the low momentum data. As was already mentioned, although the Huber & Aichelin paramterizations are not defined above $\sqrt{s} = 4.50$ GeV ($p_{lab} = 9.8$ GeV) they were extended to higher momentums. The parameterization did eventually yield a negative cross section and are therefore not shown. As shown in Fig. 3.6, the SOPEM does very well as a fit to the data especially while using the coupling constant fit to the low momentum data.

3.4.2 $pn \rightarrow \Delta^{++}\Delta^{-}$

Only four experimental data points were found for the reaction $pn \rightarrow \Delta^{++}\Delta^{-}$ [34, 48–50]. Fig. 3.7 shows that once again, the theoretical models peak about 3 GeV too low in incident momentum compared to the maximum value of the experimental data. A value of $g_{\pi N\Delta} = 5.3486$ was used for the SOPEM. The Huber & Aichelin OBEM predicts a smaller maximum total cross section compared to the SOPEM and inconsistent with the experimental data. The small set of experimental data points available coupled with the fact that the two models lie very close to each other make a thorough analysis inconclusive.

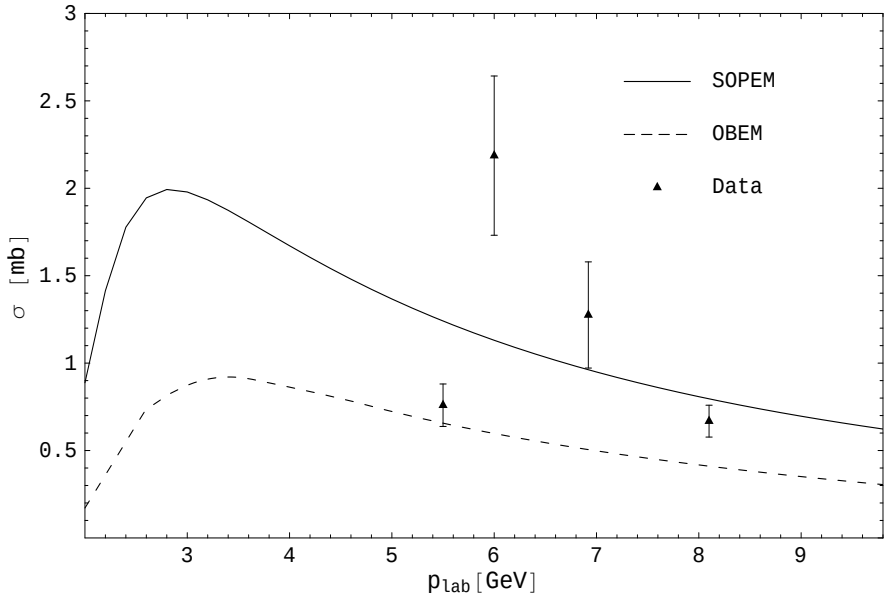

Figure 3.5: Comparison of the scalar one pion exchange model (SOPEM) and the OBEM of Huber & Aichelin [2] to experimental results [34, 48–50] for the reaction $pp \to \Delta^{++}\Delta^{0}$.

3.4.3 $pn \to \Delta^{+}\Delta^{0}$

Fig. 3.8 shows the one data point available for the reaction $pn \to \Delta^{+}\Delta^{0}$ plotted with the SOPEM ($g_{\pi N\Delta} = 4.8212$) and the Huber & Aichelin OBEM. The Huber & Aichelin OBEM, once again predicts a smaller total cross section over all incident momenta. More data is needed for any conclusions to be drawn from this reaction.

Table 3.2: χ^2 per degree of freedom analysis for $NN \to \Delta\Delta$ reactions

		χ^2 per degree of freedom
Reaction	**Model**	**p_{lab} up to 9.8 GeV**
$pp \to \Delta^{++}\Delta^{0}$	SOPEM	8.0
	OBEM	6.8
$pn \to \Delta^{++}\Delta^{-}$	SOPEM	15.0
	OBEM	17.3
$pn \to \Delta^{+}\Delta^{0}$	Only one data point available	

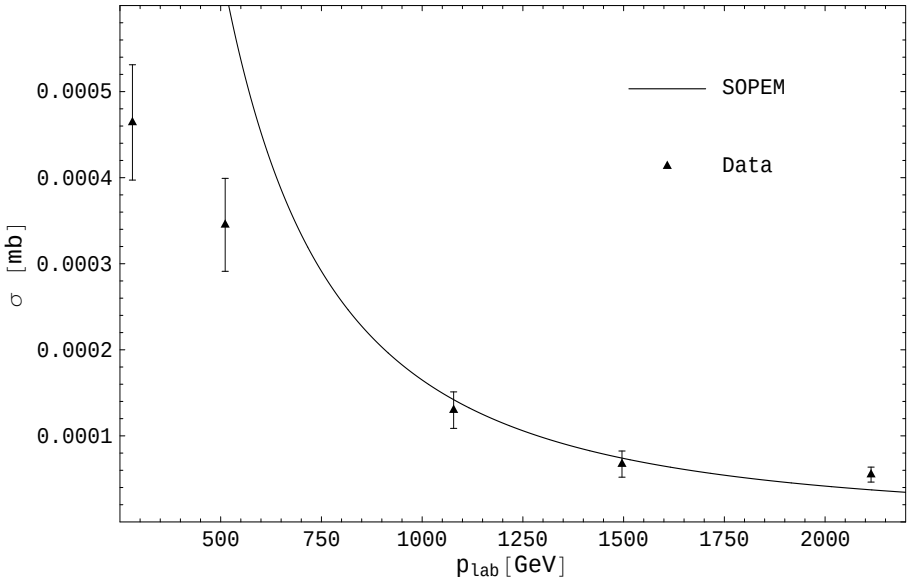

Figure 3.6: Comparison of the scalar one pion exchange model (SOPEM) to experimental results [34, 48] for the reaction $pp \rightarrow \Delta^{++}\Delta^{0}$.

3.4.4 Overall Analysis

The results of a χ^2 analysis done for each of the theoretical models with respect to the experimental data is presented in Table 3.2. The analysis is broken down for all available data and for incident momentums up to 9.8 GeV, the maximum momentum for which the Huber & Aichelin OBEM parameterizations are defined.

Overall, the Huber & Aichelin OBEM does slightly better than the SOPEM in predicting total cross sections for two Δ-resonance production from two nucleon interactions. Both models fail to predict the momentum at which the peak in the cross sections occur. An important point to make is that the lack of a large experimental data set limits the conclusiveness of this analysis.

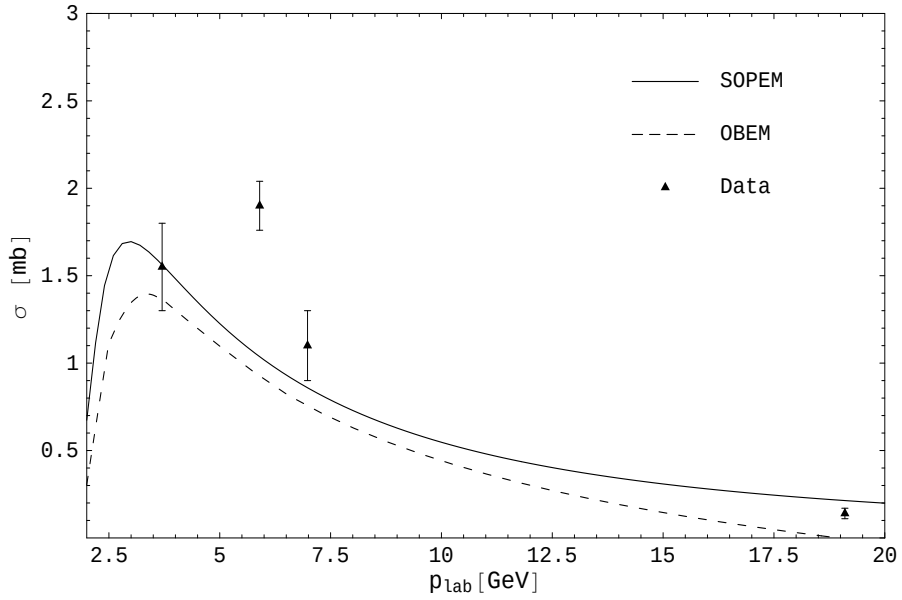

Figure 3.7: Comparison of the scalar one pion exchange model (SOPEM) and the OBEM of Huber & Aichelin [2] to experimental results [34, 48–50] for the reaction $pn \to \Delta^{++}\Delta^{-}$.

3.5 Conclusions

The production of Δ-resonances is an important topic when considering hadronic reactions. It plays in important role in the production of pions and other mesons. We presented a simple scalar quantum field theory using one pion exchange of nucleon-nucleon interactions and compared it to the state-of-the-art in Δ-resonance production models.

The OBEM of Huber & Aichelin was summarized. The model used either a pseudoscalar coupling of the pion or the tensor and vector coupling of the ρ-meson to mediate the force in the reactions of interest. For single Δ-resonance production, the Huber & Aichelin OBEM proved to be the better fit to the experimental data over the entire range of the data compared to the scalar one pion exchange model (SOPEM) we introduced here. The SOPEM, however, proved to be the better fit in both the region of incident momentum below 5 GeV and the region of large incident momentum ($p_{lab} \gtrsim 400$ GeV). Although the SOPEM works well in these regions, that does not mean it should be viewed as a faithfull description of the physical processes because it is widely accepted that these

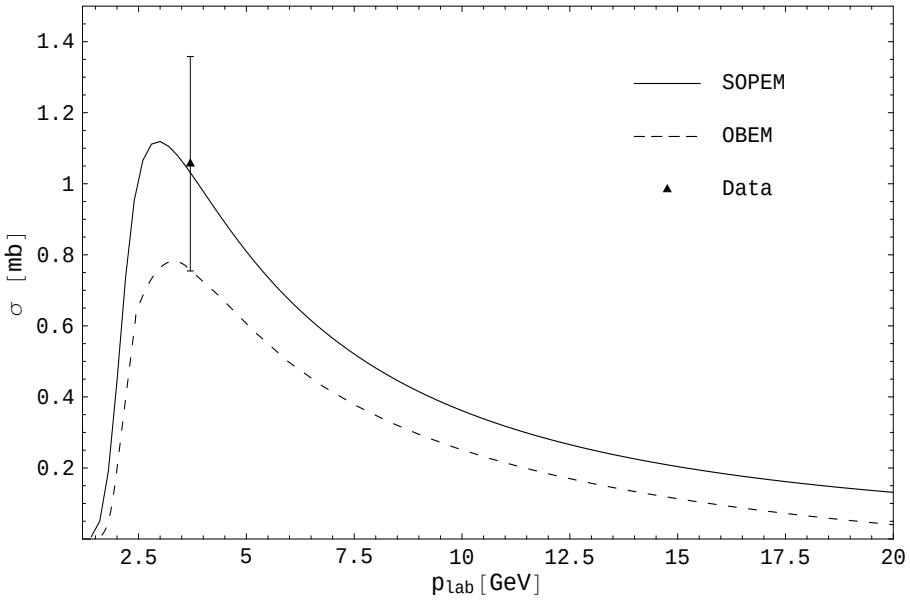

Figure 3.8: Comparison of the scalar one pion exchange model (SOPEM) and the OBEM of Huber & Aichelin [2] to experimental results [34] for the reaction $pn \to \Delta^+\Delta^0$.

fields are not scalar fields. There are spin and angular momentum effects that are important for certain processes. The SOPEM can therefore be viewed as a sophisticated parameterization that can be adjusted to fit the data well by fitting the coupling constant to a specific data set.

For the double Δ-resonance production reactions, the OBEM of Huber & Aichelin was the best fit to the data where it was defined. The parameterizations given for the OBEM, unfortunately, were only defined up to $\sqrt{s} = 4.50$ GeV ($p_{lab} \approx 9.8$ GeV). In general, we plotted the OBEM up to $p_{lab} = 20$ GeV. This corresponded to the point at which the cross sections became negative and therefore unphysical.

Although the Huber & Aichelin OBEM was the best fit to the experimental data for double Δ-resonance production, it predicted the peak in the total cross section at an incident momentum 3 GeV smaller than the experimental data reported. The SOPEM suffered from this same behavior. The small experimental data sets available for these reactions, however, make a conclusion about what to blame for the inconsistency very

difficult.

The region of incident momentum below 5 GeV has consequences for galactic cosmic ray (GCR) transport codes. These GCR transport codes use the Boltzmann transport equation along with some approximations to take an incident GCR flux (which is composed of mainly hydrogen along with heavier elements [9]) and transport it through some material (i.e. atmosphere, spacecraft walls, etc.) to determine the radiation spectrum on the other side of the material. The incident momentum of 5 GeV is of special significance because this is roughly the value of the incident momentum at which the GCR flux drops by an order of magnitude compared to the peak flux [9]. Therefore an accurate description of the physical processes in this momentum range is important to accurately model the space radiation environment and its affects on astronauts and sensitive electronics.

Given the importance of intermediate resonance states to particle production, additional work needs to be done in this area for applications to radiation transport codes. The SOPEM may be a good description of single Δ-resonance production in the momentum region of the peak, since the coupling constant for each reaction was fit to this region. The applicability of the model to other resonance reactions has not been investigated and should be looked into carefully. A more detailed analysis of the coupling constant and how it varies for each reaction should also be performed to help determine the applicability of the SOPEM.

Chapter 4

Nuclear Fragmentation

4.1 Introduction

Understanding nuclear interactions of heavy-ions is of fundamental importance to many applied technologies. The use of heavy-ions in radiation therapy (i.e.. at Lawrence Berkeley National Laboratory or the Heavy Ion Medical Accelerator in Chiba (HIMAC), Japan) relies heavily on understanding how heavy-ion beams are modified by interactions as the beam is delivered to the site of interest and how these changes affect the final quality of the radiation delivered. Nuclear interactions of heavy-ions are of fundamental importance to the safe exploration of space, as well. Outside the safety of Earth's atmosphere and magnetic field, there is a nearly isotropic background of high energy, fully ionized heavy-ions. The same heavy-ions that are utilized for precise medical treatments can also have dangerous health effects, possibly leading to the death of an individual in extreme cases. The effects of heavy-ions on microelectronics is also of interest. As transistor devices have decreased in size, the device current of the microelectronic is lowered. As a consequence, less energetic particles, which are more plentiful, can generate not only single event upsets but also multi-bit upsets where multiple logical bits in a transistor have their state changed. The errors caused by single event upsets and especially multi-bit upsets can have adverse affects on computer systems integral to space operations.

Nuclear fragmentation, the process through which energetic heavy-ions interact with target nuclei and either the projectile, target or both nuclei break apart, is a significant contributor to the nuclear interactions of heavy-ions. In addition, the possibility of multiple heavy-ion fragments being created makes this an interesting physical process. From a radiation shielding point of view, this is a troubling process and must be accounted for when determining mission risk to astronauts and sensitive electronics.

To account for the nuclear fragmentation effects of galactic cosmic rays on spacecraft shields and determine the effect of the radiation, a nuclear fragmentation cross section database is used by radiation transport codes. An accurate understanding of the nuclear fragmentation process is therefore important to accurately determine the biological effect of cosmic radiation on astronauts. In addition, to determine the uncertainty associated with the biological effects of cosmic radiation, the uncertainty of models used to generate the nuclear fragmentation database used in radiation transport codes must be quantified. The purpose of this work is to determine deficiencies in the models of nuclear fragmentation used in radiation transport codes.

The two models investigated herein are the NASA nuclear fragmentation model NUCFRG2 [51] and the quantum multiple scattering fragmentation model QMSFRG [52]. As a comparison to the models, an extensive experimental database of nuclear fragmentation cross sections was compiled and is discussed below. I will systematically investigate the differences between the two models as compared to the experimental database and identify weaknesses and strengths of the models. In addition, the effect of model differences on NASA's deterministic radiation transport code HZETRN [53] results for particle flux, absorbed dose and dose equivalent is analyzed.

4.2 NUCFRG2

The NUCFRG2 model is based on the abrasion-ablation model first proposed in 1973 by Bowman, Swiatecki and Tsang [54]. In this model the nuclear fragmentation process proceeds through two stages. The first is the abrasion stage in which the projectile and

target nuclei overlap and matter is sheared away. The remaining deformed nuclei is left in an excited state and decays through particle emission to a ground state and this is called the ablation stage. The original model was improved upon to include Coulomb trajectory corrections and the NUCFRG2 model includes improved surface energy corrections, transmission factors and the addition of light-ion production in the final fragment spectrum [51].

I present below a rough outline of the NUCFRG2 model and refer the reader to the original NUCFRG2 NASA Technical Paper for a detailed description [51].

4.2.1 NUCFRG2 Fragmentation Model

For a given impact parameter at infinity (b), a distance of closest approach (r) for two ions, defined by

$$b^2 = r(r - \frac{Z_P Z_T e^2}{E_{tot}}), \tag{4.1}$$

exists at which the interaction takes place. In Equation 4.1, E_{tot} is the total kinetic energy in the center-of-mass system (when the system is well separated), r is the relative distance between the charge centers, Z_P and Z_T are the atomic number of the projectile and target nuclei, respectively, and e is the electric charge.

When r is small, the nuclear densities overlap and mass is removed from the projectile and target. This removal of mass from either the projectile or target is called fragmentation. This is modeled in NUCFRG2 by the two-step abrasion-ablation process. In the abrasion stage, matter is sheared away while the nuclear densities of the projectile and target overlap. The residual nuclei (called prefragments) are left in an excited state and decay through heavy particle emission to a ground state configuration.

Nuclear Abrasion

NUCFRG2 only uses projectile fragmentation to model the process of heavy-ion collisions. During the abrasion stage of the projectile fragmentation, the number of nucleons abraded is given as [51]

$$\Delta A_{abr} = A_p F[1 - e^{-\frac{C_T}{\lambda}}], \tag{4.2}$$

where A_P is the projectile mass number. λ is the mean free path in nuclear matter, given as [51]

$$\lambda = \frac{16.6}{E^{.26}}, \tag{4.3}$$

with E, the projectile energy, in units of MeV/nucleon. In Equation 4.2, C_T is the target chord that maximizes the interaction potential projected onto the impact plane and F is the fraction of projectile nucleons in the interaction zone (the region of overlap between the projectile and target). Details of C_T and F are contained in the NUCFRG2 NASA Technical Paper [51].

Nuclear Ablation

During the ablation stage of projectile fragmentation, the prefragment is left in a highly unstable state. NUCFRG2 assumes a sudden approximation for the charge ratio of nucleons left in the prefragment to be equal to that of the charge ratio projectile prior to interaction. This approximation is clearly only appropriate at high energies where the projectile does not have time to react to the target. A crude visualization of this is to think of the projectile as a spheroid with a channel gouged out of it.

NUCFRG2 assumes that a nucleon is removed for every 10 MeV of excitation energy given by

$$\Delta A_{abl} = \frac{E_s + E_x}{10} + \Delta A_{spc}, \tag{4.4}$$

where ΔA_{spc} are the nucleons in the interaction zone not removed through abrasion. From Equation 4.2, one sees ΔA_{spc} must be given as

$$\Delta A_{spc} = A_P F e^{-\frac{C_T}{\lambda}}, \tag{4.5}$$

with E_s being the semiempirical surface excitation energy (in units of MeV) and is given by

$$E_s = 0.95 f \Delta S. \tag{4.6}$$

The excess surface area (ΔS) in units fm^2 is given by

$$\Delta S = 4\pi r_P^2 [1 + P - (1 - F)^{2/3}]. \tag{4.7}$$

f is a semiempirical parameter found to be

$$f = 1 + 5F + [1500 - 320(A_P - 12)]F^3. \tag{4.8}$$

The coefficient to the F^3 term is limited to being non-negative, otherwise it does not contribute to the surface excitation energy.

E_x in Equation 4.4 is given as

$$E_x = \begin{cases} 13C_l[1 + \frac{1}{3}(C_t - 1.5)] & 50\% \text{ of the time} \\ 0 & 50\% \text{ of the time.} \end{cases} \tag{4.9}$$

The double-valued nature of E_x is caused by the simple assumption that on half of the single particle collisions, the energy is transferred to excitation while the remaining half of events leave the projectile in an unexcited state. C_l and C_t are the longest chord length in the projectile surface interface and the longest chord transverse the projectile velocity, respectively.

The charge distributions of the final fragments are parameterized by Rudstam [55] as

$$\sigma(A_F, Z_F) = F_1 exp\Big[- R\big|Z_F - SA_F + TA_F^2\big|^{\frac{3}{2}}\Big]\sigma(\Delta A), \tag{4.10}$$

with the parameters $R = 11.8/A_F^{0.45}$, $S = 0.486$ and $T = 3.8 \times 10^{-4}$ all taken from Rudstam [55]. F_1 is a normalization factor [51]

4.3 QMSFRG

The formalism used in the quantum multiple scattering fragmentation (QMSFRG) model for nuclear fragmentation is based on the multiple scattering series as formulated by Glauber [56] for two heavy-ions. The multiple scattering series is solved using the impulse and eikonal approximations [52] to obtain a closed-form solution to the abrasion stage cross section spectrum. QMSFRG assumes the fragmentation reaction occurs through an abrasion stage producing a pre-fragment, which does is outside the region of overlap, and a fireball fragment produced from the projectile-target overlap region. Following the abrasion stage, an ablation stage occurs where the pre-fragment becomes the final projectile fragment through nuclear de-excitation. The ablation stage is described by a stochastic process using a Master equation for de-excitation through particle emission [52].

Table 4.1: QMSFRG Cross Sections reported in Ref. [52] published 2007

2100 MeV/u $^{16}O +^{1} H \rightarrow$	QMSFRG (mb)	Interpolation (mb)	Percent Error
n	284.1	292.4	2.96
p	310.2	312	.58
^{2}H	40.3	41.3	2.48
^{3}H	17.3	16.7	3.47
^{3}He	17.3	16.7	3.47
^{4}He	168.9	172.0	1.84
$^{16}O +^{12} C \rightarrow$			
n	2697	2717	.74
p	2902	2906	.14
^{2}H	459.6	503.1	9.46
^{3}H	140.4	130.7	6.91
^{3}He	103.7	95.4	8.00
^{4}He	457.7	438	4.30
$^{16}O + Cu \rightarrow$			
n	6459	6493	.53
p	6941	6944	.04
^{2}H	817.4	872.1	6.69
^{3}H	250.3	225.2	10.03
^{3}He	194.7	174.5	10.37
^{4}He	695.6	639.5	8.06
		RMS Error	5.68%

In addition to abrasion and ablation processes, QMSFRG also utilizes cluster knockout, electromagnetic dissociation for the production of nucleons, and a coalescence model of light-ion formation.

4.3.1 QMSFRG Interpolation

The version of QMSFRG used in the analysis of this paper is not the standard version. Access to standard QMSFRG through a machine executable file or source code was not available. Without access to source code, a QMSFRG produced cross section table that used linear interpolation over eight energy points (25, 75, 150, 300, 600, 1200, 2400, 7200 MeV/nucleon) and mixing with respect to atomic density fraction for interpolation/extrapolation over six target isotopes (^{1}H, ^{12}C, ^{16}O, ^{27}Al, ^{40}Ca, ^{56}Fe) was used.

Table 4.2: QMSFRG Cross Sections reported in Ref. [57] published 2001

600 A MeV	QMSFRG (mb)	Interpolation (mb)	Percent Error
$^{20}\mathrm{Ne} + ^{12}\mathrm{C} \rightarrow Z$			
9	93	96	3.23
8	125	114	8.8
7	96	96	0
6	125	127	1.6
5	58	39	32.76
$^{20}\mathrm{Ne} + \mathrm{Al} \rightarrow Z$			
9	117	125	6.84
8	158	143	9.49
7	121	119	1.65
6	153	155	1.31
5	66	46	30.3
$^{20}\mathrm{Ne} + \mathrm{Cu} \rightarrow Z$			
9	134	148	10.45
8	206	161	21.84
7	131	135	3.05
6	185	178	3.78
5	54	53	1.85
		RMS Error:	13.75%

Table 4.1 shows the published version of some QMSFRG fragmentation cross sections (labeled QMSFRG in the table) from Reference [52]. This was published in 2007 and is the most recent paper found with published values of QMSFRG cross sections explicitly provided.

Table 4.2 shows the published version of some QMSFRG fragmentation cross sections (labeled QMSFRG in the table) from Reference [57]. This is a much older paper and the possibility exists that the QMSFRG code has changed since publication.

Without access to source code along with version information, I am unable to decouple the error introduced from interpolation from the error due to the QMSFRG model.

Additionally, the results from 2001 [57] (Table 4.2) are summed over isotopes for a given value of Z. This summation, when compared to an isotopic analysis such as that presented in Ref. [52], tends to average out the error and specific isotopic inconsistencies that might have shown up in a more rigorous RMS error analysis are blurred away.

In summary, to definitively determine the error caused by the interpolation/extrapolation code compared to the full QMSFRG version would require published cross sections, over a range of energies, incident beams and targets with isotopic resolution of many different fragments.

4.4 Model Validation

In order to determine the validity of the nuclear fragmentation models NUCFRG2 and QMSFRG, I needed to assemble a database of experimental nuclear fragmentation cross sections. The experimental database created consists of over 300 experiments with 25 distinct projectile isotopes from ^{10}B to ^{58}Ni, a projectile kinetic energy range of 90 A MeV to 5000 A MeV and both elemental and compound targets ranging from hydrogen to uranium [57–82]. An overview of the experimental database is shown in Table 4.3.

A large component of the experimental database consists of work conducted by Zeitlin, Guetersloh, Heilbronn, *et al.* of Lawrence Berkeley National Laboratory [57–62] with collaborators at the Heavy Ion Medical Accelerator in Chiba (HIMAC) at the National Institute of Radiological Sciences in Japan and Brookhaven National Laboratory's Alternating Gradient Synchrotron.

4.4.1 Validation Metrics

A validation metric is defined herein as a measure of the accuracy of a model as a representation of the physical process it describes within the intended region of applicability of the model. In the case of QMSFRG and NUCFRG2, both are nuclear fragmentation cross section models used as inputs into the deterministic galactic cosmic ray transport code HZETRN [53]. Only projectile fragmentation of isotopes up to ^{58}Ni and to projectile kinetic energies on the order of 50 A MeV and larger are considered in this analysis. Only projectile elements up to nickel are considered because after this point there is drop off in cosmic ray abundance of three orders of magnitude [9]. The energy is restricted to above 50 A MeV due to the trend for the reaction cross sections for nucleus-nucleus interactions

Table 4.3: Overview of the experimental database assembled for validation.

Projectile	Energy Range (MeV/nucleon)	Distinct Energies	Targets
^{58}Ni	338	1	H
^{56}Fe	330-5000	17	H,He,Li,Be,C,Al, S,Cu,Ag,Sn,Ta,Pb,U
^{52}Cr	343	1	H
^{48}Ti	1000	1	H,C,Al,Cu,Sn,Pb
^{40}Ca	357-763	4	H
^{40}Ar	90-650	11	H,Be,C,Al,KCl, Cu,Ag,Sn,Pb
^{36}Ar	213-1650	11	H,Be,C,Al,Cu,Ag,Sn,Pb
^{35}Cl	650-1000	2	H,C,Al,Cu,Sn,Pb
^{32}S	365-1149	6	H,C
^{28}Si	290-1296	14	H,C,Al,Cu,Ag,Sn,Pb
^{27}Al	582	1	H,He
^{24}Mg	309-1455	7	H,C,Al,Cu,Ag,Sn,Pb
^{23}Na	401-461	2	H,C
^{22}Ne	377-894	3	H
^{20}Ne	290-1057	7	H,C,Al,Cu,Ag,Sn,Pb
^{21}O	557	1	C
^{20}O	585	1	C
^{19}O	635	1	C
^{18}O	573	1	C
^{17}O	629	1	C
^{16}O	290-2100	10	H,He,Be,C,Al,Cu,Ag,Sn,Pb
^{14}N	290-516	4	H,He,C,Al,Cu,Sn,Pb
^{12}C	290-3660	27	H,He,Be,C,CH_2,H_2O, Al,Cu,Ag,Sn,Pb
^{11}B	326-561	5	H,He,C,Al,Cu,Sn,Pb
^{10}B	400	1	H,C,Al

to fall very quickly below 50 A MeV [83].

In this paper, three different metrics are utilized. The first is the chi-squared per datum (χ^2/n). χ^2 is defined as

$$\chi^2 = \frac{(\sigma_{model} - \sigma_{exp})^2}{(\delta\sigma_{exp})^2}, \tag{4.11}$$

where σ_{model} and σ_{exp} are the model and experimental cross sections respectively, while

Table 4.4: Overall model results for comparison to all experimental data for the three validation metrics. The Fraction Within Tolerance (FWT) uses a tolerance of 25% relative error.

Validation Metric	**NUCFRG**	**QMSFRG**
χ^2/n	448.01	325.73
RMS Error (%)	159.67	118.55
FWT	0.631	0.685

$\delta\sigma_{exp}$ is the experimental cross section uncertainty.

The second metric utilized herein is the Root-Mean-Square (RMS) error. For a set of n experimental and model cross sections,

$$\text{RMS error} = \sqrt{\sum_{i=1}^{n} \epsilon_i^2}, \tag{4.12}$$

where ϵ_i is the relative error defined as

$$\epsilon = \frac{\sigma_{model} - \sigma_{exp}}{\sigma_{exp}}. \tag{4.13}$$

The final metric used in this analysis is based on the idea of a tolerance test. The fraction of model cross sections within a defined tolerance of the experimental result including the error bars from the experiment is calculated. This test is named the Fraction Within Tolerance (FWT). For the analysis, a tolerance of 25% relative error as defined in Equation 4.13 was chosen.

4.4.2 Overall Results

The results of this analysis for the complete experimental database are shown in Table 4.4. QMSFRG is, in general, a better description of the experiments contained in the database with an RMS error of about 119% compared to the 160% of NUCFRG2.

Table 4.5 shows the results of the analysis for 7 common targets within the experimental database. The QMSFRG interpolation is the better model, using the FWT metric, for all

Table 4.5: Results for model comparison to the complete experimental database grouped by experimental target. The Fraction Within Tolerance (FWT) uses a tolerance of 25% relative error.

	NUCFRG	QMSFRG	NUCFRG	QMSFRG
Target	χ^2/n	χ^2/n	FWT	FWT
Hydrogen	501.51	311.18	0.70	0.69
Helium	5638.46	3957.17	0.55	0.80
Carbon	1210.49	1197.07	0.56	0.63
Aluminum	338.29	189.5	0.71	0.78
Copper	77.44	68.24	0.71	0.76
Tin	75.25	83.56	0.81	0.84
Lead	67.51	95.33	0.74	0.66

targets except hydrogen and lead. The QMSFRG interpolation result for lead is not as conclusive as one might like. This is due to the issue of the version of QMSFRG available to us for analysis utilizes target isotope mixing for interpolation and extrapolation over targets from a standard cross section table as discussed in Section 4.3.1. The heaviest target isotope contained in the database is ^{56}Fe. One expects the error introduced through target isotope mixing to increase the farther from ^{56}Fe the target is. NUCFRG2 does fairly poorly for light targets (C, He) in contrast to the results for hydrogen. The difference between NUCFRG2 results for light targets versus hydrogen targets is due to NUCFRG2 using a semi-empirical parameterization for fragmentation on hydrogen targets, that based on the work of Silberberger, Tsao, and Shapiro [84].

Table 4.6 illustrates the analysis of the results for three energy regions of the experimental database. NUCFRG2 severely underperforms in the E $\leq$ 300 A MeV energy region compared to its average FWT. Both models do the best in the 300 $<$ E $\leq$ 1000 A MeV energy region. The QMSFRG interpolation version performs the poorest in the E $>$ 1000 A MeV.

The NUCFRG2 and the QMSFRG interpolation version were investigated as a function of the charge removed from the projectile with the results shown in Table 4.7. With respect to FWT, NUCFRG2 outperforms the QMSFRG interpolation version for 9 out of the 17 values investigated. For small values of the charge removed the QMSFRG interpolation

Table 4.6: Results for model comparison to the complete experimental database separated into three energy regions. The Fraction Within Tolerance (FWT) uses a tolerance of 25% relative error.

	NUCFRG	QMSFRG	NUCFRG	QMSFRG
ENERGY	χ^2/n	χ^2/n	FWT	FWT
E $\leq$ 300	2431.3	2725.5	0.52	0.65
300 $<$ E$\leq$1000	104.64	56.06	0.69	0.73
E $>$ 1000	343.52	109.1	0.56	0.60

version is the better fit. For large values (Z $>$ 11) of the charge removed, NUCFRG2 performs the best. Both models have an anomalously large values of FWT for charge removal values of 6, 10 and 14 compared to the overall trend for the model.

For Table 4.8, with regard to FWT, NUCFRG2 is the better model for $Z_{frag} \geq 20$. Another trend stands out when analyzing the results grouped by individual fragment charge. Beginning near $Z_{frag} = 13$, NUCFRG2 appears to perform more poorly with odd fragment charges compared to even fragment charges.

Table 4.9 show the results of the analysis grouped by projectile element. NUCFRG2, using FWT as the metric for comparison, performs better than the QMSFRG interpolation routine for the heavy projectiles (nickel, iron, chromium, and titanium), while the QMSFRG interpolation version is the better description of the majority of the remaining dataset. This finding is consistent with the previous discusion of NUCFRG2 being the better description for heavy fragment production and the QMSFRG interpolation version being the better description for light fragment production.

4.4.3 Model Comparison to Berkeley Group Results

Figures C.40 through C.59 (found in Appendix C) show correlation graphs for NUCFRG2 and QMSFRG interpolation version compared to all the Berkeley Group's currently available experimental data. Each data point in these graphs represents the model cross sections for a given fragment charge compared to the experimental result.

Figures C.40 and C.41 show the results for NUCFRG2 and the QMSFRG interpolation

Table 4.7: Results for model comparison to the complete experimental database grouped by charge removed from the projectile. The Fraction Within Tolerance (FWT) uses a tolerance of 25% relative error.

	NUCFRG	QMSFRG	NUCFRG	QMSFRG
Z_{frag}	χ^2/n	χ^2/n	FWT	FWT
Z_p -1	260.48	74.92	0.77	0.78
Z_p -2	148.91	101.64	0.79	0.82
Z_p -3	1179.07	273.27	0.69	0.87
Z_p -4	50.61	62.43	0.71	0.80
Z_p -5	61.35	21.73	0.71	0.79
Z_p -6	1396.67	409.00	0.91	0.91
Z_p -7	18.02	17.03	0.78	0.76
Z_p -8	24.15	21.20	0.62	0.74
Z_p -9	34.49	34.77	0.69	0.62
Z_p -10	208.77	121.64	0.85	0.83
Z_p -11	3777.25	1765.23	0.59	0.65
Z_p -12	107.49	23.53	0.78	0.58
Z_p -13	12.78	12.64	0.71	0.67
Z_p -14	16.75	20.04	0.85	0.77
Z_p -15	22.73	34.49	0.63	0.63
Z_p -16	43.59	46.02	0.60	0.40
Z_p -17	72.64	33.59	0.00	0.17

version respectively for 289 and 391 A MeV carbon-12 beams incident on the six standard targets H, C, Al, Cu, Sn, and Pb [59]. Fragment charge cross sections for Z = 5–3 are shown. Figure C.40 shows NUCFRG2 doing very well for all targets except hydrogen with an FWT of .81 for all six targets. Figure C.41 shows a lack of charge dependence for the QMSFRG interpolation version results for all targets giving an FWT of .61.

Experimental results for nitrogen-14 beams at 290 A MeV and 400 A MeV [62] are shown compared to the models in Figures C.42 and C.43. The QMSFRG interpolation version shown in Figure C.43 does very well for this experimental data set with an FWT of .97 while the NUCFRG2 model (shown in Figure C.42) has much less overall correlation with the experimental data with an FWT of .50.

Figures C.44 and C.45 show the analysis for using oxygen-16 beams at 290, 400, 600 and 1000 A MeV on the 6 standard targets used by the Berkeley Group. Fragment of charges Z

Table 4.8: Results for model comparison to the complete experimental database grouped by the charge of the produced fragment. The Fraction Within Tolerance (FWT) uses a tolerance of 25% relative error.

	NUCFRG	QMSFRG	NUCFRG	QMSFRG
Z_{frag}	χ^2/n	χ^2/n	FWT	FWT
25	38.37	38.94	0.97	0.89
24	41.64	39.23	0.92	0.9
23	20.39	18.34	0.90	0.93
22	21.6	15.79	0.91	0.87
21	29.33	24.53	0.83	0.78
20	15.73	18.56	0.96	0.91
19	28.3	17.26	0.76	0.82
18	15.8	28.29	0.79	0.62
17	33.16	25.04	0.75	0.72
16	21.45	8.89	0.75	0.94
15	29.13	9.9	0.72	0.86
14	88.07	17.31	0.77	0.76
13	23.81	17.52	0.73	0.84
12	17.62	13.97	0.88	0.89
11	43.31	26.73	0.71	0.83
10	28.71	30.22	0.83	0.76
9	637.81	24.78	0.45	0.80
8	28.29	26.39	0.83	0.77
7	29.7	27.96	0.69	0.75
6	49.5	19.37	0.43	0.85
5	2203.74	571.45	0.48	0.49
4	1358.15	371.51	0.32	0.37
3	933.87	542.44	0.29	0.27
2	1031.93	549.51	0.06	0.68
1	54981.8	21988.05	0.05	0.05

= 5–7 were measured [62]. As in the case of the carbon beam, NUCFRG2 is giving a larger cross section for all fragments compared to the experimental results (Figure C.44) resulting in an FWT of .82. The QMSFRG interpolation model does slightly better as shown in Figure C.45 with an FWT of .88. There also is a trend for the QMSFRG interpolation version to begin to underpredict cross sections as targets become more massive.

Results for the analysis of the NUCFRG2 model and the QMSFRG interpolation version are shown in Figures C.46 and C.47, respectively, using neon-20 projectile beams

Table 4.9: Results for model comparison to the complete experimental database grouped by projectile element. The Fraction Within Tolerance (FWT) uses a tolerance of 25% relative error.

	NUCFRG	QMSFRG	NUCFRG	QMSFRG	NUCFRG	QMSFRG
Projectile	χ^2/n	χ^2/n	RMS (%)	RMS (%)	FWT	FWT
Ni	73.1	158.0	22.9	44.0	0.83	0.58
Fe	35.0	31.8	40.5	41.7	0.82	0.77
Cr	82.8	166.2	27.5	99.7	0.82	0.45
Ti	46.6	38.3	108.2	27.9	0.79	0.71
Ca	28.2	3.7	27.0	21.4	0.73	0.95
Ar	87.0	45.9	117.3	194.5	0.54	0.62
S	36.5	42.7	69.0	92.3	0.50	0.70
Si	55.2	14.2	36.0	21.9	0.64	0.87
Al	72.9	53.1	42.9	22.8	0.69	0.81
Mg	106.9	18.8	45.9	23.9	0.54	0.80
Na	170.2	85.6	38.2	25.2	0.50	0.60
Ne	484.7	32.9	30.0	24.6	0.68	0.82
N	145.1	53.3	55.2	27.7	0.51	0.83
O	3458.1	3211.3	254.0	157.9	0.49	0.63
C	135.6	124.5	93.7	60.7	0.39	0.37
B	204.7	333.5	150.9	132.8	0.40	0.47

at 290, 400 and 600 A MeV incident on the six standard targets for fragments of charge Z = 5–9 [57, 62]. NUCFRG2 does well representing the data for the hydrogen target, but performs poorly for all other targets. For the neon beams, NUCFRG2 has an FWT of .77. NUCFRG2 also begins to exhibit a distinct lack of energy dependence compared to the experimental results. The lack of energy dependence is evident in the lack of vertical separation of the cross sections compared to the horizontal separation for a fragment at different energies. The QMSFRG interpolation version does just as well as NUCFRG2 with an FWT of .78. The increasing relative error as the mass of the target increases is seen again. The QMSFRG interpolation version is also giving a much smaller cross section for Z=5 fragments as seen for the data points very close to the horizontal axis for carbon, aluminum, copper, tin and lead targets.

Figures C.48 and C.49 show the comparison of the models to the experimental data for a magnesium-24 beam at an energy of 400 A MeV [62]. The comparison for NUCFRG2

(Figure C.48) show a very scattered comparison giving an FWT of .58. The results of the comparison for the QMSFRG interpolation model are shown in Figure C.49. QMSFRG does a fair job of representing the experimental data with an FWT of .71. Again, the issue of increasing relative error with increasing target mass is present.

The comparison for silicon-28 beams at energies of 290, 400, 600, 800, 1200 A MeV [60] with NUCFRG2 and the QMSFRG interpolation version is shown in Figures C.50 and C.51 respectively. NUCFRG2 performs best for the hydrogen target compared to the heavier targets and suffers from the lack of energy dependence as mentioned above in the discussion of the neon projectiles for all heavier targets, resulting in an FWT of .65. The QMSFRG interpolation version is a very good description of this data set with a .92 FWT but, again, suffers from the underprediction of the cross sections for increasing target mass.

Results for the analysis of the NUCFRG2 model and QMSFRG interpolation version are shown in Figures C.52 and C.53, respectively, compared to 650 and 1000 A MeV ^{35}Cl beams on the six standard targets for fragments of charge Z = 5-16 [61]. Unlike previous lighter projectile beams, NUCFRG2 begins to underpredict the cross sections for production of all fragments. For the larger mass targets, NUCFRG2 is a fairly good representation of the cross section data. A FWT value of .79 for the whole chlorine data set is found. The QMSFRG interpolation version is a very good representation of this data set with a .91 FWT.

Figures C.54 and C.55 show the results of the comparison for the NUCFRG2 model and the QMSFRG interpolation version with experimental data for ^{40}Ar beams of 290, 400 and 600 A MeV energies [61]. NUCFRG2 (see Figure C.54) tends to give cross sections that are too small compared to the experimental results. NUCFRG2 still gives a fairly good FWT value of .68 for this data set. The QMSFRG interpolation version gives a FWT value of .81 and shows good correlation in Figure C.55.

The experimental results for a 1000 A MeV ^{48}Ti beam incident on the 6 elemental targets H, C, Al, Cu, Sn and Pb [61] for fragment production cross sections with charge Z = 5–21 are compared with NUCFRG2 results in Figure C.56 and the QMSFRG inter-

polation version in Figure C.57. NUCFRG2 does a good job describing the data with a FWT of .79 while the QMSFRG interpolation version has a FWT of .71. Both models, however, do poorly for fragments with Z $\leq$ 8 giving cross sections that are approximately 40% too small for all targets except hydrogen.

Results for the analysis of the NUCFRG2 model and QMSFRG interpolation version are shown in Figures C.58 and C.59, respectively, compared to 400, 500, 600, 800, 1000 and 5000 A MeV ^{56}Fe beams on the six standard targets for fragments of charge Z = 10-25 [58]. It was found that the NUCFRG2 model is an excellent description of this experimental data set having a FWT of .92. A lack of energy dependence for a given fragment charge, however, is still seen. The QMSFRG interpolation version was found to have a FWT value of .83 for this data set.

4.4.4 Model Comparison to Iancu *et al.*

In this section, the experimental cross sections of Iancu *et al.* for ^{40}Ar projectile fragmentation given in reference [75] are compared to the theoretical models. Fragment cross sections for charges Z = 7-17 are reported for a beam energy of 400 A MeV on H, C, Al, Cu, Ag and Pb targets. Results for both the NUCFRG2 model and the QMSFRG interpolation version compared to the experimental cross sections are shown in Figures C.60 through C.65 for the charged fragment cross sections for each target.

Figure C.60 shows the results for ^{40}Ar $+^{1}$ H $\rightarrow$ Z_{frag}. Both NUCFRG2 and the QMSFRG interpolation version are a good qualitative representation of this data and quantitatively they both have a FWT of 1.00.

The experimental data for C, Al, Cu, Ag and Pb targets, shown in Figures C.61 - C.65, display a pronounced even-odd effect that is mirrored well by the QMSFRG interpolation version. The even-odd effect is the enhancement of even charged fragments compared to nearest neighbor odd charged fragments. The NUCFRG2 model, however, does not display this behavior.

In addition, for C, Al, Cu, Ag and Pb targets the QMSFRG interpolation version gives

cross sections which are approximately 30% too large for fragment charges of Z $\leq$ 15. Both of the models perform comparably for the ^{40}Ar projectile data of Iancu *et al.* [75] with NUCFRG2 have an RMS error of 44% and an FWT of .69, while the QMSFRG interpolation version had an RMS error of 41% and an FWT of .67.

4.4.5 Model Comparison to Flesch *et al.*

A comparison of the experimental projectile fragmentation of ^{28}Si producing fragments of charge Z = 6 - 13 by Flesch *et al.* reported in Reference [73] is shown in Figures C.66–C.71. Figure C.66 shows the results for NUCFRG2 and the QMSFRG interpolation version compared to the experimental data for the reaction $^{28}\mathrm{Si} + ^{1}\mathrm{H} \rightarrow \mathrm{Z}_{frag}$. The even-odd effect for results on hydrogen targets is not as pronounced as compared to heavier targets. The QMSFRG interpolation version has an even-odd effect that is much too exaggerated compared to the experimental data giving an RMS error of 46% and a FWT of .38. NUCFRG2 has an RMS error of 42% and an FWT of .75.

For the rest of the data, Figures C.67 - C.71, NUCFRG2 does fairly poorly from a qualitative standpoint as it fails to represent the pronounced even-odd effect in the experimental data. For the whole data set, NUCFRG2 has an RMS error of 42% and an FWT value of .55.

The QMSFRG interpolation model results for C, Al and Cu targets does a very good job of representing the Z = odd fragments, except for Z = 13. It tends to give too large of a cross section compared to the data, expect for Z = 6 and Z = 12 fragments. For Ag and Pb targets, the QMSFRG interpolation model does very well representing the most fragments with Z $\leq$ 11, but increasingly gives a cross section which is too small compared to the experimental values for fragments of charge Z = 11 and Z = 12.

Over the whole data set, QMSFRG is showing an increase in the cross section for Z = 13 compared to Z = 12 cross section that is not consistent with the data set. NUCFRG2, however, gives an overly drastic decrease in the cross section for Z = 13 compared to Z = 12, that does not fit the data well.

The QMSFRG interpolation version does better in representing this data set, having a RMS error of 26% and an FWT of .80. This is consistent with the results for all silicon projectiles in the experimental database shown in Table 4.9.

4.4.6 Model Comparison to Korejwo *et al.* [78, 79]

Figures C.72 and C.73 show the results of a correlation analysis for NUCFRG2 and the QMSFRG interpolation version, respectively, compared with experimental isotopic cross sections from ^{12}C fragmentation on hydrogen [78, 79]. Fragment isotopes from helium to carbon from 1870, 2690 and 3660 A MeV ^{12}C beams are analyzed.

Overall, NUCFRG2 has an RMS error of 151% and a FWT value of .70. The disproportionality of these values is due to the NUCFRG2 values for ^{8}B fragments, which, for the each of the three energies shown in Figure C.72 has a relative error of about 600%. This is not terribly surprising since ^{8}B is a fairly neutron-deficient nucleus and NUCFRG2 is not expected to do well with the production of fragments far from the stability. If these three cross sections are removed from the analysis of the RMS error for NUCFRG becomes 64%.

The QMSFRG interpolation version has an RMS error of 59% and a FWT of .38 for the whole data set. With a FWT of .44 for both the 1870 and 2690 A MeV beams, the QMSFRG interpolation version performs more poorly for the 3660 A MeV beam with a FWT of .24.

4.5 Nuclear fragmentation effects on galactic cosmic ray transport

A proper understanding of how heavy-ions interact with material is of fundamental importance to the problem of radiation shielding for spaceflight. Nuclear fragmentation cross sections databases are an important input to galactic cosmic ray transport codes and therefore it is of interest to analyze how differences in nuclear fragmentation cross sections

affect radiation transport code results.

For this analysis, the 2005 version of the deterministic radiation transport HZETRN developed at NASA Langley Research Center [53], was utilized, with either NUCFRG2 or QMSFRG as the fragmentation cross section database. The version of HZETRN used for this analysis employed linear interpolation over energy for nuclear fragmentation cross sections for NUCFRG2 in addition to the interpolation over energy and mixing with respect to atomic density fraction for target interpolation/extrapolation for QMSFRG, as discussed in Section 4.3.1. A 190 isotope grid was used for the initial galactic cosmic ray spectrum with isotopes from neutrons to ^{58}Ni.

Figures C.74 - C.76 shows the results for the percent difference in flux versus energy for each charge group in the isotope database used in HZETRN at a depth of 10, 50 and 300 g/cm^2, respectively, in polyethylene. Polyethylene is investigated because it is being considered as a future shielding material due to its large hydrogen content. Percent difference for flux simply means the value of flux from HZETRN using NUCFRG2 minus the value of the flux using QMSFRG scaled to NUCFRG2. Therefore positive values in Figures C.74 - C.76 means NUCFRG2 is contributing more flux for a given charge compared to QMSFRG. As expected, the flux difference becomes exaggerated with depth. This effect is due to the increased likelihood of interactions as the radiation penetrates more deeply into the material.

The results for percent difference in flux as a function of energy is shown in Figures C.77 - C.80 for carbon, nitrogen, oxygen, and iron fragments at 13 different depths in polyethylene. Carbon, nitrogen, oxygen and iron are emphasized here because they are important components of galactic cosmic rays. Carbon, nitrogen and oxygen together make up a fairly large fraction of the heavy-ion component of the galactic cosmic ray flux [9]. Iron is especially important because it has a relative abundance one to two orders of magnitude larger than ions comparative mass and charge [85]. A large relative abundance and charge makes iron important from the point of view of the radiation dose delivered since dose is proportional to Z^2, where Z is the charge of the ion.

For carbon, nitrogen and oxygen, as seen in Figures C.77 - C.79, the QMSFRG interpolation version predicts more flux compared to NUCFRG2 resulting in an increase in flux of approximately 50% at a depth of 300 g/cm^2 at all energies. Iron, on the other hand, has a larger flux by about 80% for NUCFRG2 compared to the interpolation version of QMSFRG.

Figures C.81 and C.82 show the results for dose and dose equivalent, respectively, versus material depth for polyethylene and aluminum as calculated using HZETRN. Dose is a measure of how much energy is deposited per unit mass of material and dose equivalent is the dose multiplied by a radiation weighting factor for a given type of ionizing radiation. Dose equivalent is used to allow for the different biological effectiveness of different types of radiation. This is due to the increased biological damage that $\alpha-$particles cause. The results using the QMSFRG interpolation version (labeled QMSFRG) are shown as a red dashed line and the results using NUCFRG2 are shown with a solid black line. For both aluminum and polyethylene, the difference between the two models is so small that the lines lie basically on top of each other for both dose and dose equivalent.

To help quantify how model differences affect dose and dose equivalent, Figures C.83 and C.84 show the dose difference and dose equivalent difference between NUCFRG2 and the QMSFRG interpolation version. For both dose and dose equivalent, the model differences in the fragmentation cross sections only lead to a maximum difference of about 1.5%. While there are significant differences in the flux for a given element between the two models, as used in HZETRN, there is an averaging effect that is occurring for dose and dose equivalent. As can be seen in Figure C.76, there is approximately the same density of lines below and above the horizontal axis which leads to this averaging effect.

4.6 Conclusions

Overall, a few areas in which each model can be improved have been identified. For NUCFRG2, there is a distinct lack of energy dependence for a given elemental fragment. In addition, for fragments of charge $Z_{frag} \leq 13$, NUCFRG2 represents the data poorly

for odd charged fragments compared to even charged fragments. NUCFRG2 also fails to produce the even-odd effect seen in elemental fragment production. The even-odd effect is due to nuclear shell structure effects on stability of the nucleus. Quantitatively, however, NUCFRG2 performs fairly well compared to the QMSFRG interpolation version and actually outperforms the QMSFRG interpolation version for large values of the charge removed from the projectile.

The QMSFRG interpolation version does well representing the even-odd effect seen in the experimental data and also performs well for small values of the charge removed from the projectile. A systematic increasing relative error with increasing target mass was observed. The determination of whether this is due to the extrapolation and interpolation with respect to atomic density of the targets or actual QMSFRG model deficiency is not possible without access to either source code or a machine executable version of the full QMSFRG model. This inability to decouple the error introduced by interpolation and extrapolation from the error intrinsic to the physical model is an area that will need future attention.

The affect that nuclear fragmentation model differences has on radiation shielding analysis using the deterministic radiation transport code HZETRN was also analyzed. For a given element, it was found that the flux can be significantly affected by nuclear fragmentation model differences and the discrepancy in flux due to nuclear fragmentation model differences increases as the depth of the material increases. For biological metrics such as dose and dose equivalent, an averaging effect was found lead to very little difference in dose or dose equivalent.

Chapter 5

Conclusions

To accurately model space radiation interactions, the NASA deterministic radiation transport code HZETRN requires accurate cross section databases of particle interactions. This work focused on developing and evaluating these cross section databases. A scalar quantum field theory of pion exchange, called the scalar one pion exchange model (SOPEM), was introduced in an attempt to describe nucleon-nucleon interactions over the large range of energies important to space radiation. The need for computationally efficient radiation transport codes relies partially on the use of simple cross section formulas for particle interactions. With this in mind, using the very simple SOPEM to obtain simple cross section formulas for nucleon-nucleon interactions seemed like a reasonable starting place.

The scalar one pion exchange model is first compared to a full quantum field theory of the one pion exchange with spin and isospin dependence included for the case of proton-proton elastic scattering. A simple parameterization developed by Bertsch and Das Gupta [18] was also used as a comparison for proton-proton elastic scattering. Both total and invariant differential cross sections were developed for the two models and compared to experimental data to determine the validity and applicability of the models. The scalar one pion exchange model performed fairly well, being the best description of the total cross section at low energy and performing only slightly worse than the parameterization for the invariant differential cross section data. The fully spin and isospin dependent one

pion exchange model performed moderately well for the total cross section data, but was the worst description of the differential cross section data.

With the comparison to proton-proton elastic scattering completed, the scalar one pion exchange model is applied to single and double Δ-resonance production from nucleon-nucleon interactions. The production of pions via an intermediate Δ-resonance is an important process at the energies of interest for space radiation [2–4]. An intermediate resonance production model for pions is currently not used in the NASA meson and muon transport code MESTRN and has been identified as an important update to the code [4].

The scalar one pion exchange model was compared to the one pion exchange model of Dmitriev *et al.* [3] with pseudovector coupling and the one boson exchange model of Huber & Aichelin [2] which utilized ρ-meson exchange in addition to pion exchange. The three models were analyzed with respect to experimental data for Δ-resonance production. None of the theoretical models were a good description of the data for double Δ-resonance production as they predicted a peak in the total cross section at too low of momentum. In addition, a lack of experimental data for double Δ-resonance production made a thorough analysis difficult. For single Δ-resonance production, the scalar one pion exchange model was found to be the best description of the experimental data for incident lab momentum below 5 GeV and above 300 GeV, while the one boson exchange model of Huber & Aichelin performed the best in the middle momentum range. A detailed investigation of how the coupling constant varies for each reaction should be conducted in the future to better determine the applicability of the SOPEM to resonance processes.

In addition to nucleon-nucleon interactions, heavy-ion interactions are important to space radiation shielding. In particular, nuclear fragmentation, the process through which energetic heavy-ions interact with target nuclei and either the projectile, target or both nuclei break apart, is a significant contributor to the nuclear interactions of heavy-ions. With this in mind, I compiled an extensive experimental cross section database. This was then used to determine the validity of two nuclear fragmentation models, NUCFRG2 and QMSFRG, identify model weaknesses and determine the extent nuclear fragmentation

model discrepancy affect the results of HZETRN. NUCFRG2 is a semiempirical abrasion-ablation model and QMSFRG is a non-relativistic quantum multiple scattering model of nuclear fragmentation based on the Glauber formalism.

It was found that NUCFRG2 has a distinct lack of energy dependence for a given elemental fragment. Also, NUCFRG2 performs more poorly for odd charged fragments compared to even charged fragments when $Z_{frag} \leq 13$. NUCFRG2 did represent the experimental data the best for large values of the charge removed from the projectile ($Z_{proj} - Z_{frag} > 11$). It was found, however, that NUCFRG2 fails to produce the even-odd effect seen in elemental fragment production. The even-odd effect is due to shell structure effects on stability of the nucleus. QMSFRG, in contrast, does well representing the even-odd effect. QMSFRG also did well representing the data for small values of the charge removed from the projectile. A systematic increase in the relative error with increasing target mass was observed in QMSFRG. Unfortunately, I did not have access to source code for QMSFRG and only had a pre-made cross section database with a linear interpolation routine over energy and interpolation and extrapolation with respect to atomic density of the target. Therefore, determining whether the increasing relative error with increasing target mass was due to the interpolation and extrapolation routine or was intrinsic to the QMSFRG model was not possible.

Both NUCFRG2 and QMSFRG are used by HZETRN in the analysis of space radiation effects on astronauts and therefore an analysis of how the model differences affect radiation shielding analysis was performed. It was found for a given element, the flux can be significantly affected by differences in the nuclear fragmentation database. However, for biological metrics such as dose and dose equivalent, an averaging effect leads to a difference of only a few percent.

Future research I would like to perform includes defining metrics and tolerances for future nuclear fragmentation and radiation transport analysis and investigating other nuclear fragmentation models suitable for use in HZETRN. In addition, the development of a fully relativistic multiple scattering theory of nuclear fragmentation may be needed.

A relativistic multiple scattering theory would be more appropriate for applications to galactic cosmic ray shielding than the non-relativistic models currently used. I would also like to implement an updated pion production cross section database in MESTRN which includes a resonance production model. Finally, I would like to fully integrate the formalism of MESTRN into the production version of HZETRN, including validation and application to atmospheric studies.

Appendix A

Expansion of the OPEM interaction Lagrangian

This is a derivation of the expansion of the $\bar{\Psi}\boldsymbol{\tau}\cdot\boldsymbol{\pi}\Psi$ term that appears in the interaction Lagrangian of the OPEM (Eq. 2.1).

If we define the pion fields and the Pauli isospin matrices as

$$\pi^{\pm} = \frac{1}{\sqrt{2}}(\pi_1 \mp i\pi_2) \tag{A.1}$$

$$\pi^{0} = \pi_3 \tag{A.2}$$

$$\tau^{\pm} = \frac{1}{\sqrt{2}}(\tau_1 \pm i\tau_2) \tag{A.3}$$

$$\tau^{0} = \tau_3. \tag{A.4}$$

This implies that

$$\begin{aligned} \boldsymbol{\tau}\cdot\boldsymbol{\pi} &= \tau_1\pi_1 + \tau_2\pi_2 + \tau_3\pi_3 \\ &= \tau^{+}\pi^{-} + \tau^{-}\pi^{+} + \tau^{0}\pi^{0}. \end{aligned} \tag{A.5}$$

Using

$$\Psi = \begin{pmatrix} p \\ n \end{pmatrix} \tag{A.6}$$

$$\bar{\Psi} = (\bar{p} \quad \bar{n}), \tag{A.7}$$

allows us to write

$$\begin{aligned} \mathcal{L}_{\pi NN} &= -ig_{\pi NN}\bar{\Psi}\gamma_5 \boldsymbol{\tau}\cdot\boldsymbol{\pi}\Psi \\ &= -ig_{\pi NN}(\bar{p} \quad \bar{n})\gamma_5\Big[\sqrt{2}\begin{pmatrix} 0 & 1 \\ 0 & 0 \end{pmatrix}\pi^- + \sqrt{2}\begin{pmatrix} 0 & 0 \\ 1 & 0 \end{pmatrix}\pi^+ \\ &\quad + \begin{pmatrix} 1 & 0 \\ 0 & -1 \end{pmatrix}\pi^0\Big]\begin{pmatrix} p \\ n \end{pmatrix} \\ &= -ig_{\pi NN}(\sqrt{2}\bar{p}\gamma_5 n\pi^- + \sqrt{2}\bar{n}\gamma_5 p\pi^+ + \bar{p}\gamma_5 p\pi^0 - \bar{n}\gamma_5 n\pi^0). \end{aligned} \tag{A.8}$$

Appendix B

Derivation of t_0 and t_π

This is the derivation of the limits of integration for Equation 2.35. In any reference frame,

$$\begin{aligned} t &\equiv (p_1 - p_3)^2 \\ &= (E_1 - E_3)^2 - (\boldsymbol{p}_1 - \boldsymbol{p}_3)^2. \end{aligned} \tag{B.1}$$

Now look at only the momentum piece:

$$\begin{aligned} (\boldsymbol{p}_1 - \boldsymbol{p}_3)^2 &= |\boldsymbol{p}_1|^2 + |\boldsymbol{p}_3|^2 - 2\boldsymbol{p}_1 \cdot \boldsymbol{p}_3 \\ &= |\boldsymbol{p}_1|^2 + |\boldsymbol{p}_3|^2 - 2|\boldsymbol{p}_1||\boldsymbol{p}_3| \cos\theta \\ &= |\boldsymbol{p}_1|^2 + |\boldsymbol{p}_3|^2 - 2|\boldsymbol{p}_1||\boldsymbol{p}_3|(1 - 2\sin^2\frac{\theta}{2}) \\ &= (|\boldsymbol{p}_1| - |\boldsymbol{p}_3|)^2 + 4|\boldsymbol{p}_1||\boldsymbol{p}_3| \sin^2\frac{\theta}{2}, \end{aligned} \tag{B.2}$$

where θ is the angle between the vectors $\boldsymbol{p}_1$ and $\boldsymbol{p}_3$.

The values used in Equation 2.35 are defined for angles in the CM frame $t_0 \equiv t(\theta_{cm} = 0)$ and $t_\pi \equiv t(\theta_{cm} = \pi)$. Using these values in Equation B.2 one finds,

$$t_0 = (E_{1,cm} - E_{3,cm})^2 - (|\boldsymbol{p}_{1,cm}| - |\boldsymbol{p}_{3,cm}|)^2 \quad \text{(B.3)}$$

$$t_\pi = (E_{1,cm} - E_{3,cm})^2 - (|\boldsymbol{p}_{1,cm}| + |\boldsymbol{p}_{3,cm}|)^2. \quad \text{(B.4)}$$

Now $E_{1,cm}$ and $E_{3,cm}$ need to be cast into functions of s and the masses of the particles.

$$s \equiv (p_1 + p_2)^2 = (p_3 + p_4)^2 \quad \text{(B.5)}$$

$$\sqrt{s} = E_{1,cm} + E_{2,cm} = E_{3,cm} + E_{4,cm}. \quad \text{(B.6)}$$

Now use the relations for the CM reference frame,

$$E_{1,cm}^2 = \boldsymbol{p}_{1,cm}^2 + m_1^2 \quad \text{(B.7)}$$

$$E_{2,cm}^2 = \boldsymbol{p}_{2,cm}^2 + m_2^2, \quad \text{(B.8)}$$

along with $|\boldsymbol{p}_{1,cm}| = |\boldsymbol{p}_{2,cm}|$, to obtain

$$\sqrt{s} = E_{1,cm} + \sqrt{E_{1,cm}^2 - m_1^2 + m_2^2}. \quad \text{(B.9)}$$

Squaring both sides and simplifying yields

$$E_{1,cm} = \frac{s + m_1^2 - m_2^2}{2\sqrt{s}}. \quad \text{(B.10)}$$

By a similar process, the value for $E_{3,cm}$ is given as:

$$E_{3,cm} = \frac{s + m_3^2 - m_4^2}{2\sqrt{s}}. \quad \text{(B.11)}$$

To complete the derivation, $|\boldsymbol{p}_{1,cm}|$ and $|\boldsymbol{p}_{3,cm}|$ need to be rewritten in terms of λ_{12},

λ_{34} and s. From Equation B.6,

$$\begin{aligned} s &= (E_{1,cm} + E_{2,cm})^2 \\ &= E_{1,cm}^2 + E_{2,cm}^2 + 2E_{1,cm}E_{2,cm} \\ &= \boldsymbol{p}_{1,cm}^2 + m_1^2 + \boldsymbol{p}_{1,cm}^2 + m_2^2 + 2\sqrt{(\boldsymbol{p}_{1,cm}^2 + m_1^2)(\boldsymbol{p}_{1,cm}^2 + m_2^2)}, \end{aligned} \tag{B.12}$$

where we have used the fact that $|\boldsymbol{p}_{1,cm}| = |\boldsymbol{p}_{2,cm}|$ to obtain Equation B.12. Simplifying Equation B.12 gives

$$\begin{aligned} 4\boldsymbol{p}_{1,cm}^2 s &= (s - m_1^2 - m_2^2)^2 + 4m_1^2 m_2^2 \\ &= \lambda_{12}. \end{aligned} \tag{B.13}$$

Therefore,

$$|\boldsymbol{p}_{1,cm}| = \sqrt{\frac{\lambda_{12}}{4s}}. \tag{B.14}$$

By a similar process, the value of $|\boldsymbol{p}_{3,cm}|$ is give as:

$$|\boldsymbol{p}_{3,cm}| = \sqrt{\frac{\lambda_{34}}{4s}}. \tag{B.15}$$

Substituting Equations B.10, B.11, B.14 and B.15 into Equations B.3 and B.4 gives us the final results

$$t_0 = \frac{1}{4s}[(m_1^2 - m_2^2 - m_3^2 + m_4^2)^2 - (\sqrt{\lambda_{12}} - \sqrt{\lambda_{34}})^2] \tag{B.16}$$

$$t_\pi = \frac{1}{4s}[(m_1^2 - m_2^2 - m_3^2 + m_4^2)^2 - (\sqrt{\lambda_{12}} + \sqrt{\lambda_{34}})^2] \tag{B.17}$$

Appendix C

Figures

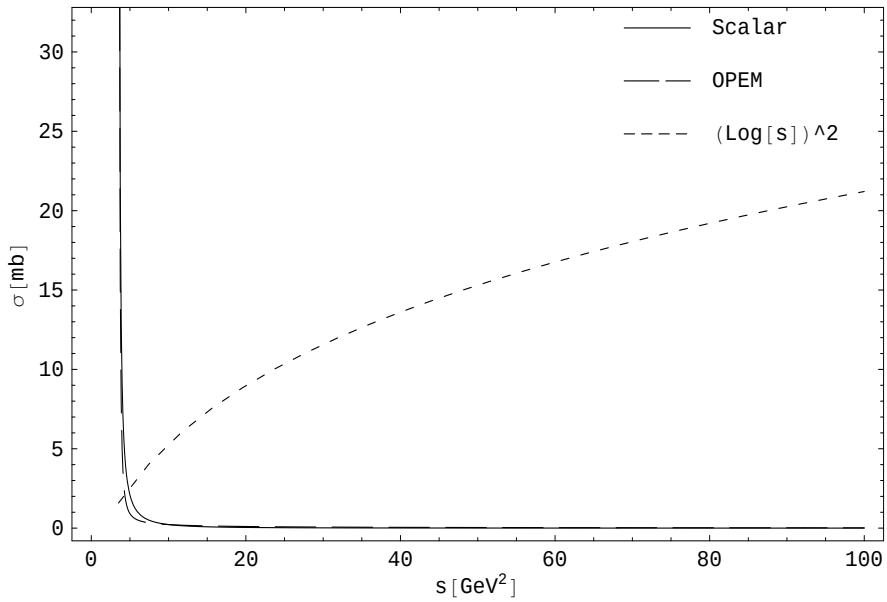

Figure C.1: Comparison of the cross sections for the scalar theory and OPEM to the Froissart bound (98) [17]. Notice that the curves for the scalar theory and the OPEM lie very close to one another.

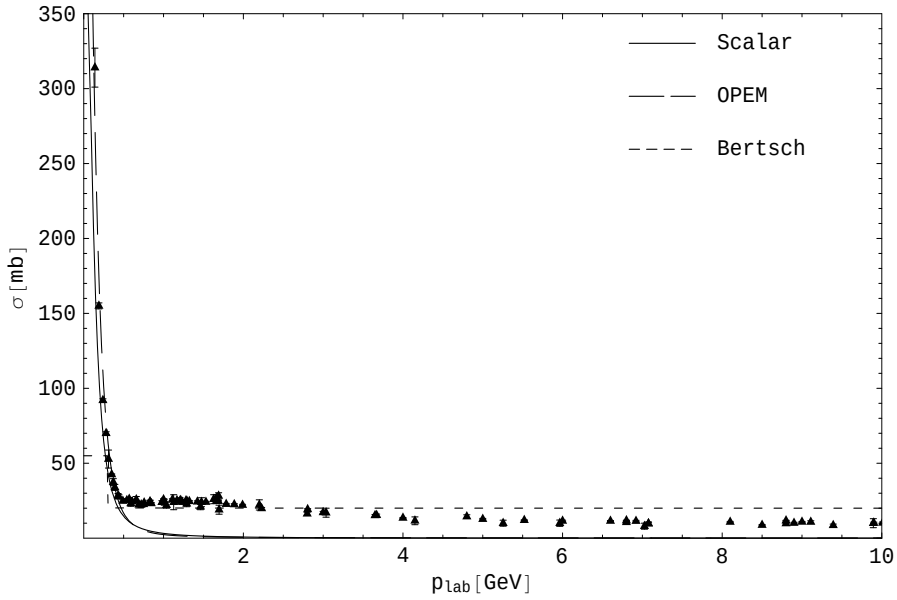

Figure C.2: Comparison of the theoretical curves for OPEM, scalar theory and the parameterization of Bertsch [18] to data from the Particle Data Group [19] in the lab momentum range of $p_{lab} = 0 - 10$ GeV.

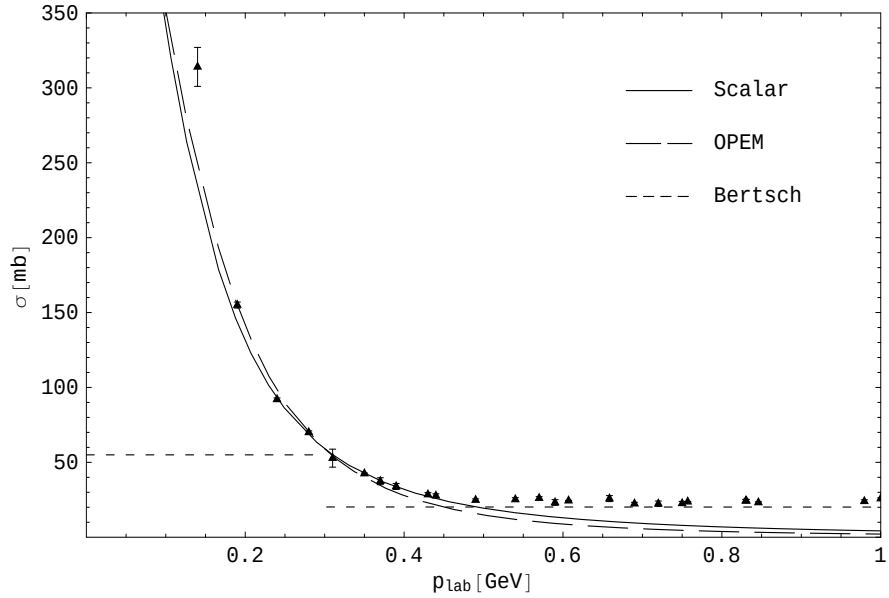

Figure C.3: Comparison of the theoretical curves for OPEM, scalar theory and the parameterization of Bertsch [18] to data from the Particle Data Group [19] in the lab momentum range of $p_{lab} = 0 - 1$ GeV.

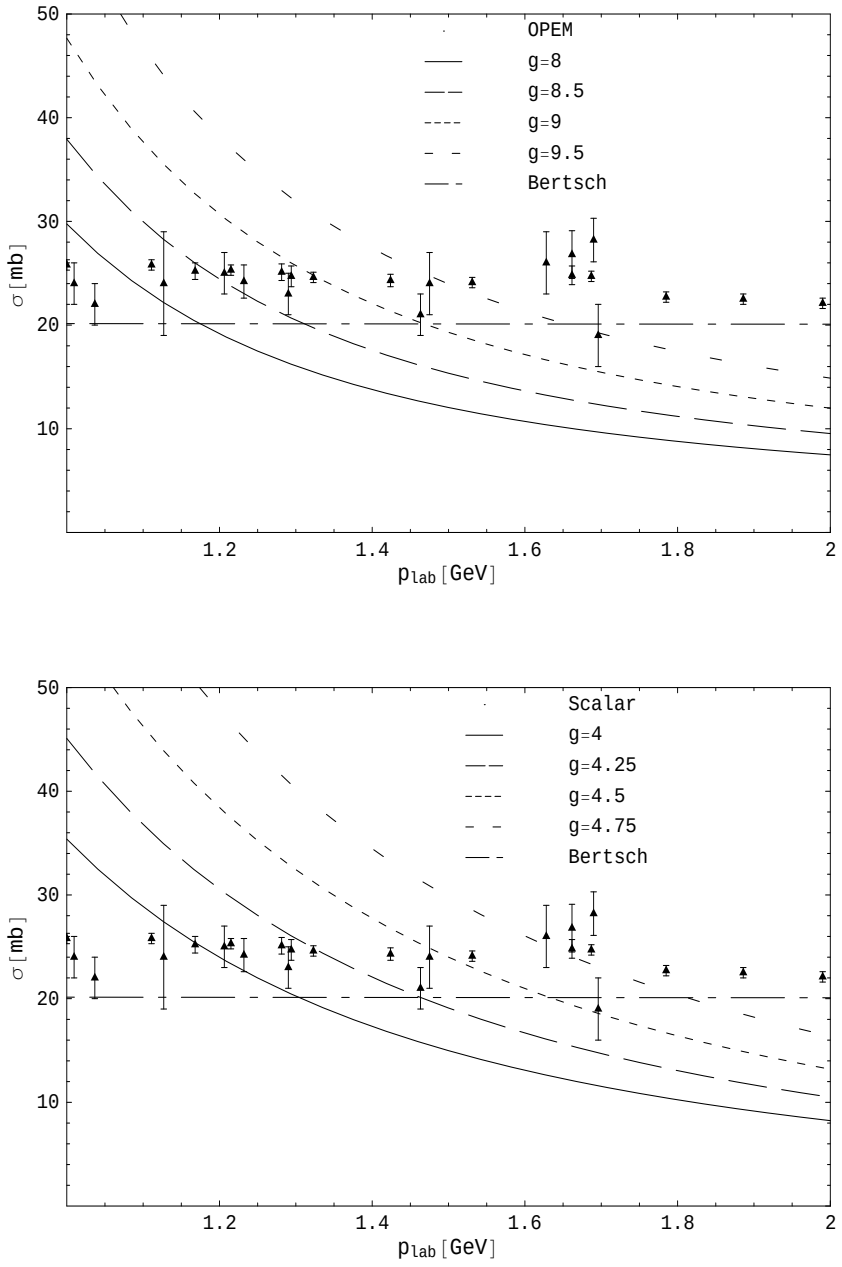

Figure C.4: The OPEM (top) and the scalar theory (bottom) versus the parameterization of Bertsch [18] to data from the Particle Data Group [19] in the lab momentum range of $p_{lab} = 1 - 2$ GeV for a variety of different coupling constants.

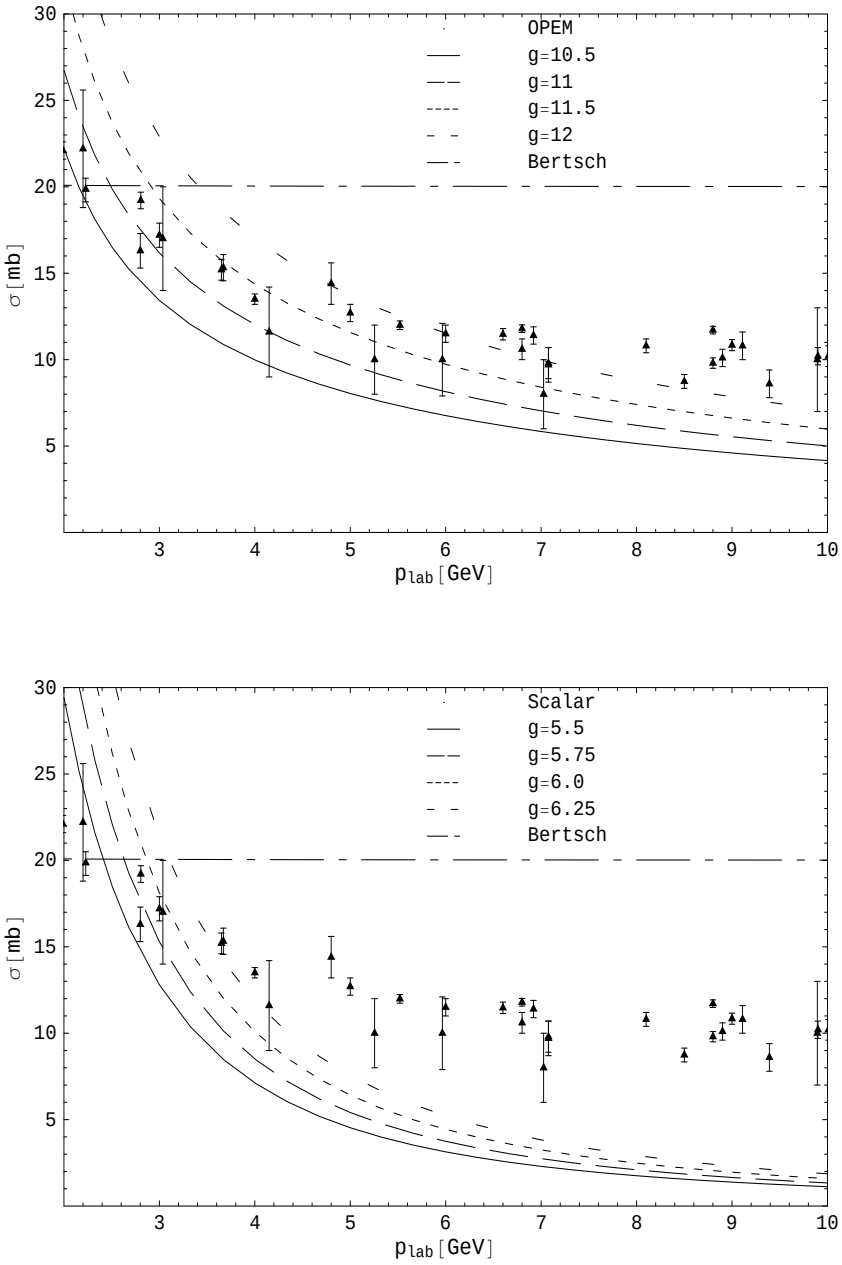

Figure C.5: The OPEM (top) and the scalar theory (bottom) versus the parameterization of Bertsch [18] to data from the Particle Data Group [19] in the lab momentum range of $p_{lab} = 2 - 10$ GeV for a variety of different coupling constants.

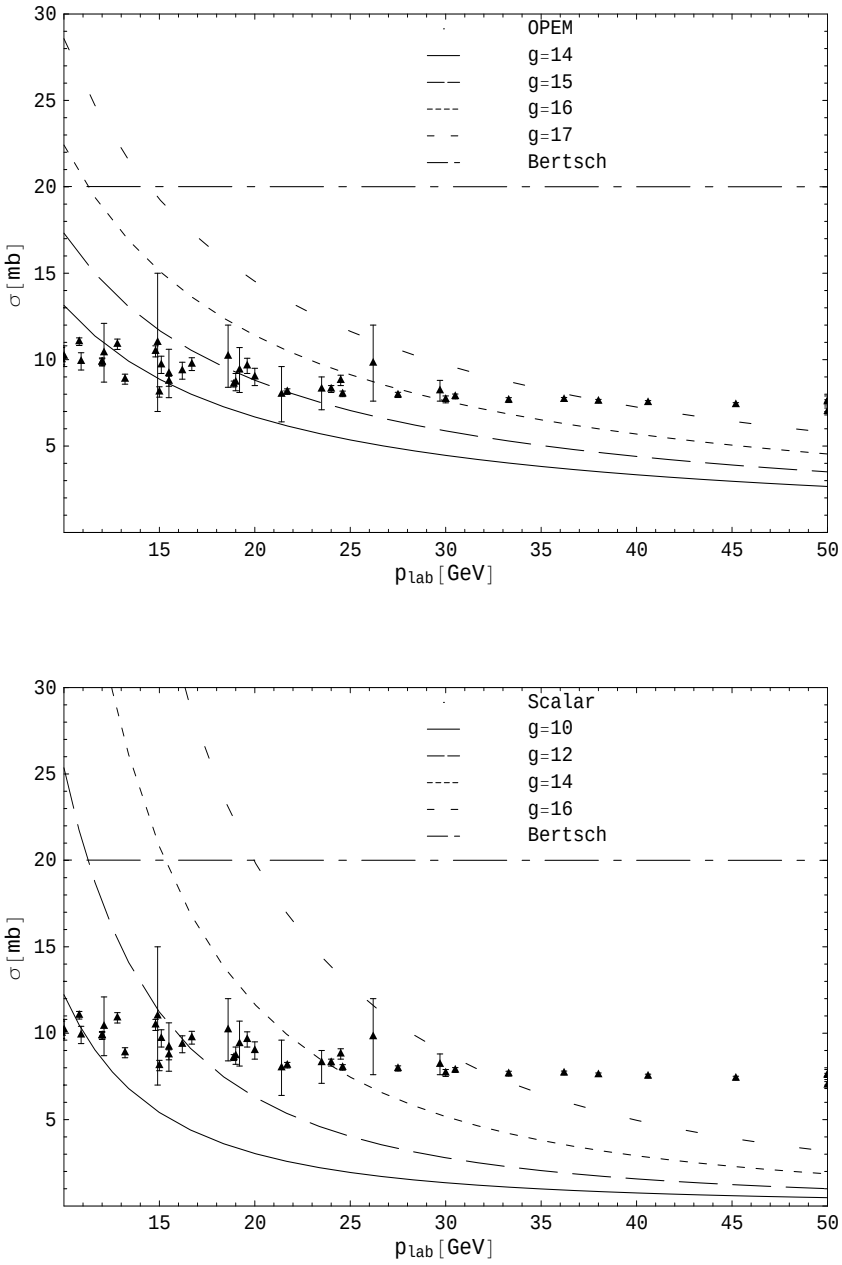

Figure C.6: The OPEM (top) and the scalar theory (bottom) versus the parameterization of Bertsch [18] to data from the Particle Data Group [19] in the lab momentum range of $p_{lab} = 10-50$ GeV for a variety of different coupling constants.

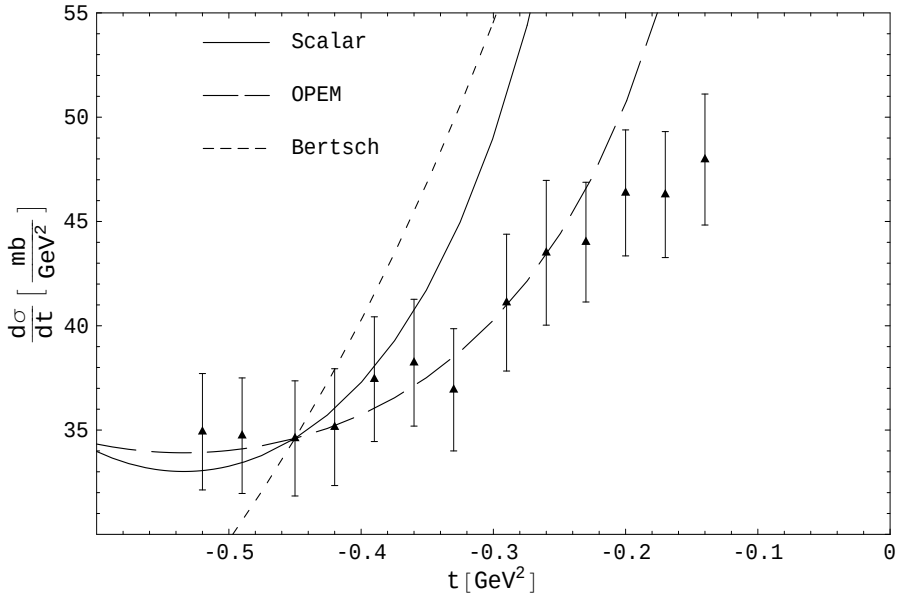

Figure C.7: Comparison of the theoretical curves for OPEM, scalar theory and the parameterization of Bertsch [18] to data from Albrow *et al.* [20] at $p_{lab} = 1.18$ GeV.

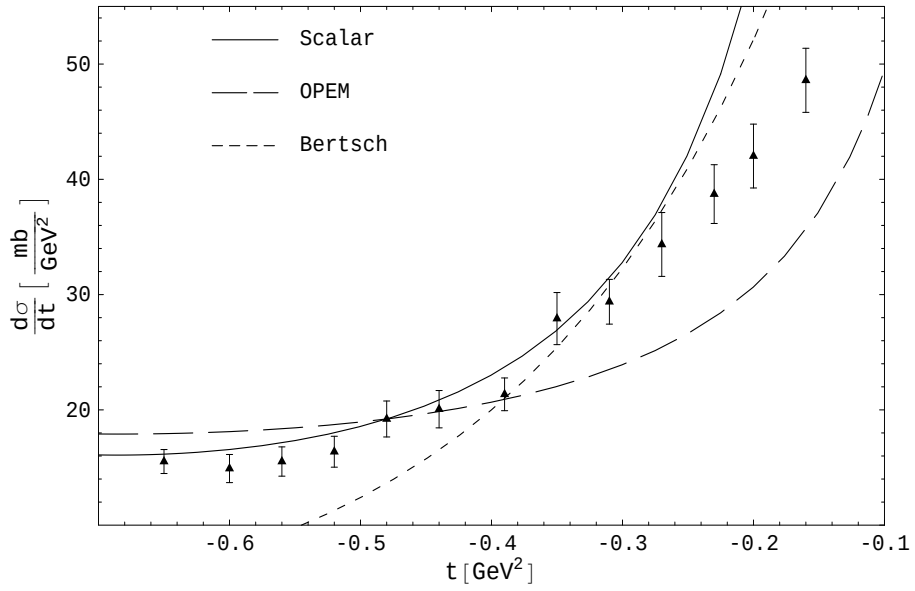

Figure C.8: Comparison of the theoretical curves for OPEM, scalar theory and the parameterization of Bertsch [18] to data from Albrow *et al.* [20] at $p_{lab} = 1.38$ GeV.

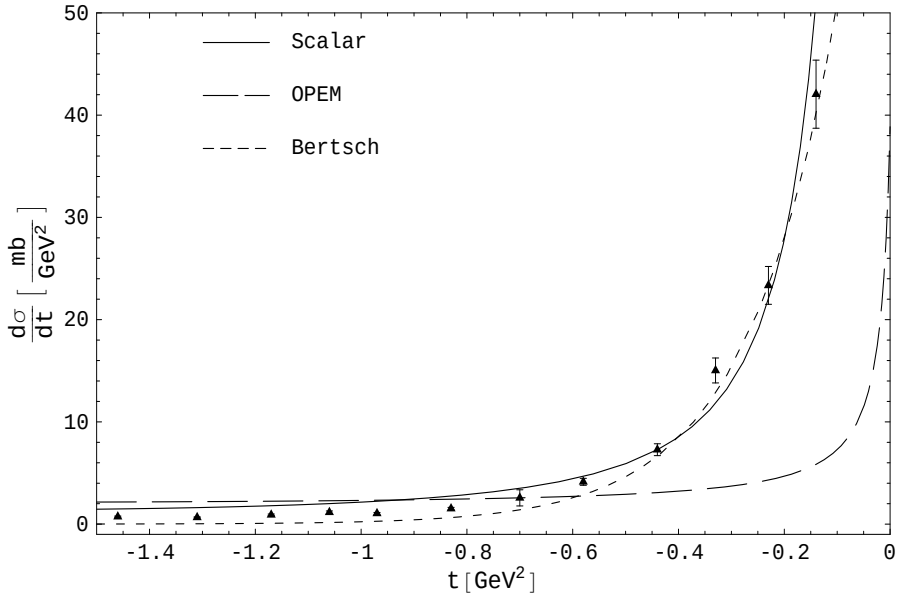

Figure C.9: Comparison of the theoretical curves for OPEM, scalar theory and the parameterization of Bertsch [18] to data from Albrow *et al.* [20] at $p_{lab} = 2.74$ GeV.

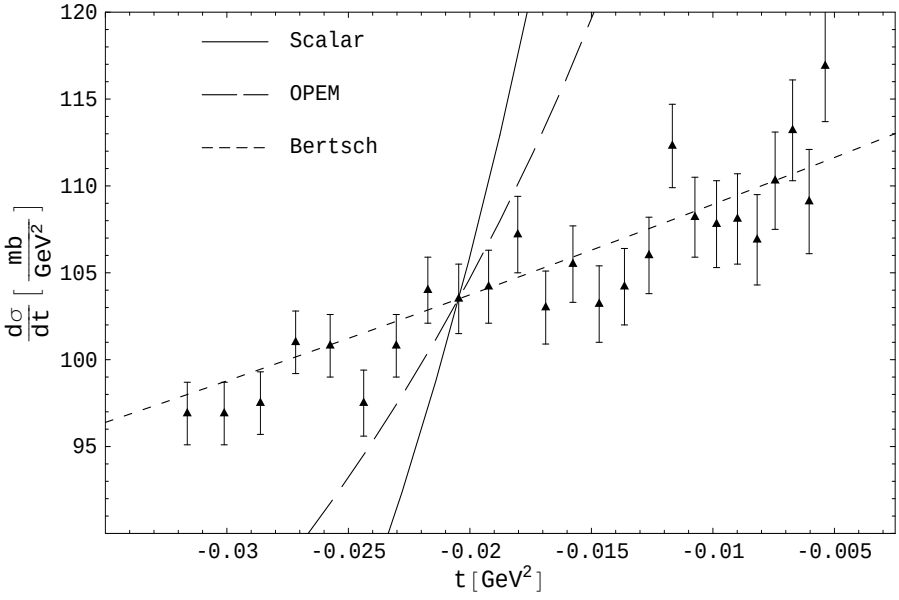

Figure C.10: Comparison of the theoretical curves for OPEM, scalar theory and the parameterization of Bertsch [18] to data from Dobrovolsky *et al.* [21] at $p_{lab} = 1.399$ GeV.

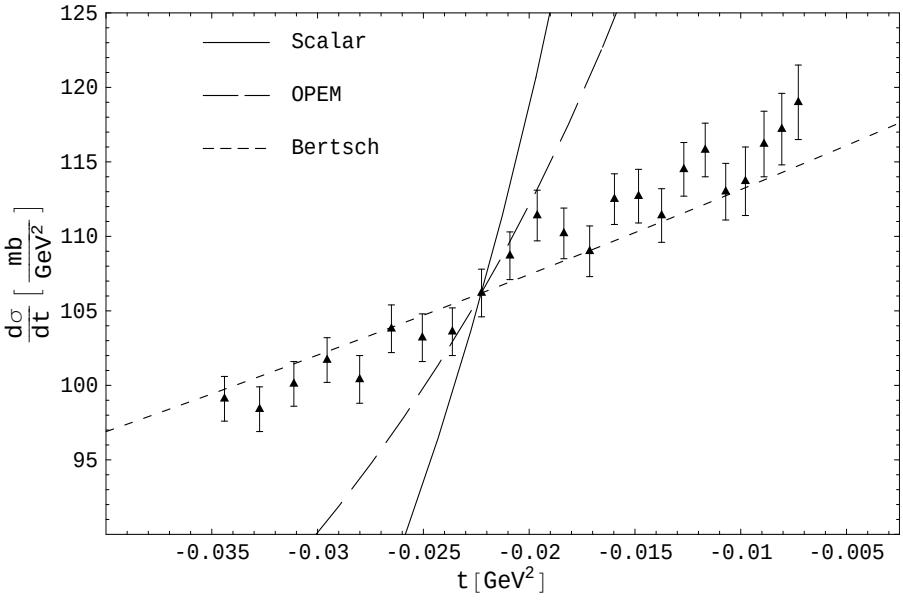

Figure C.11: Comparison of the theoretical curves for OPEM, scalar theory and the parameterization of Bertsch [18] to data from Dobrovolsky *et al.* [21] at $p_{lab} = 1.457$ GeV.

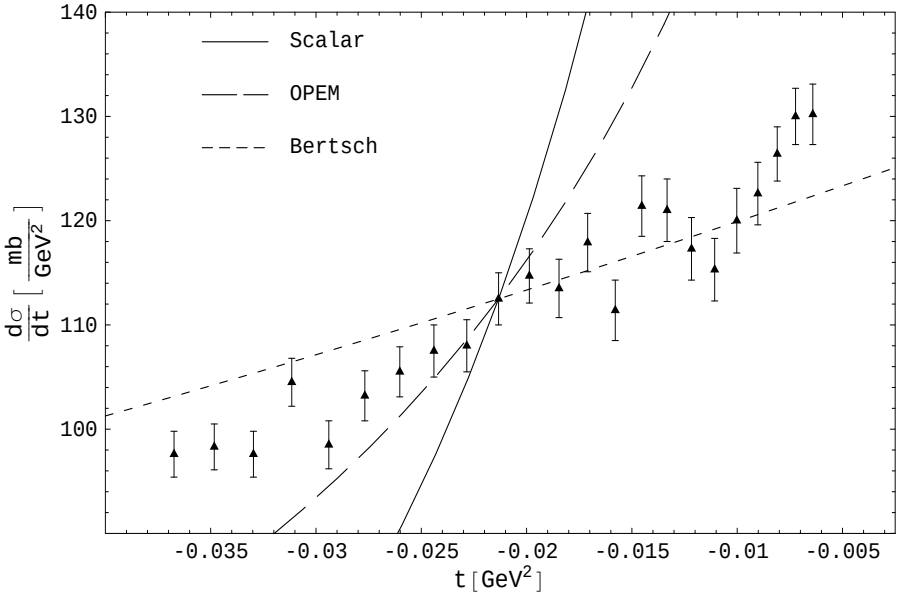

Figure C.12: Comparison of the theoretical curves for OPEM, scalar theory and the parameterization of Bertsch [18] to data from Dobrovolsky *et al.* [21] at $p_{lab} = 1.629$ GeV.

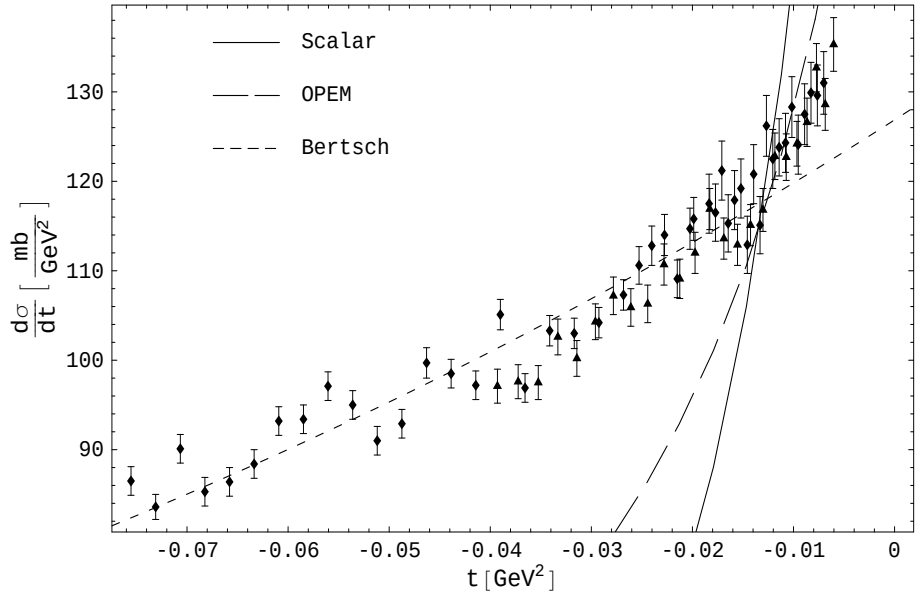

Figure C.13: Comparison of the theoretical curves for OPEM, scalar theory and the parameterization of Bertsch [18] to data from Dobrovolsky *et al.* [21] at $p_{lab} = 1.686$ GeV.

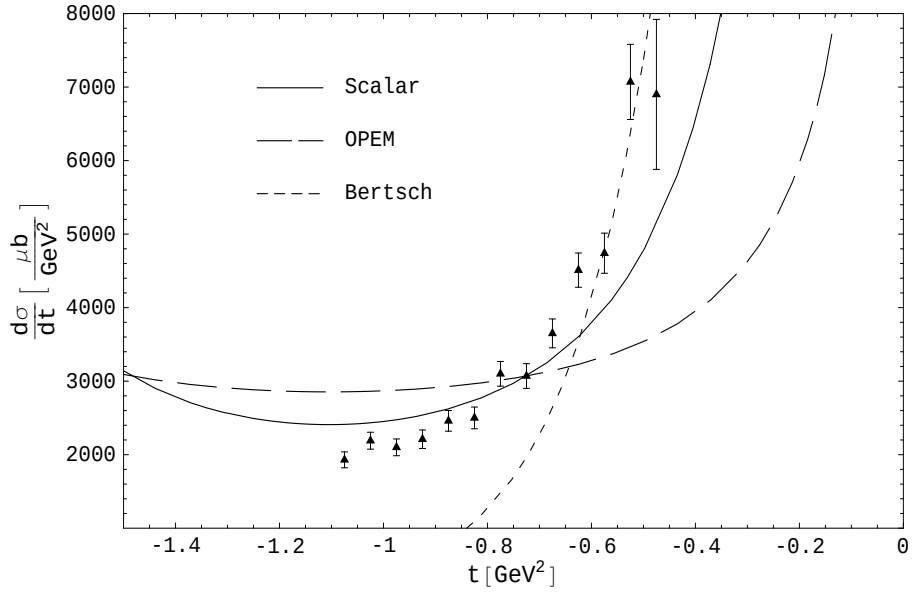

Figure C.14: Comparison of the theoretical curves for OPEM, scalar theory and the parameterization of Bertsch [18] to data from Jenkins *et al.* [22] at $p_{lab} = 1.896$ GeV.

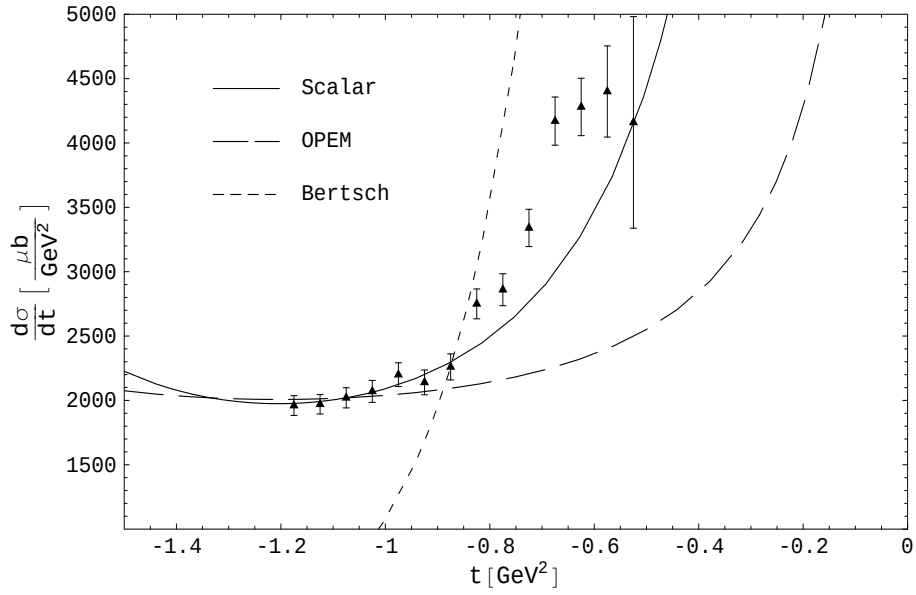

Figure C.15: Comparison of the theoretical curves for OPEM, scalar theory and the parameterization of Bertsch [18] to data from Jenkins *et al.* [22] at $p_{lab} = 2.015$ GeV.

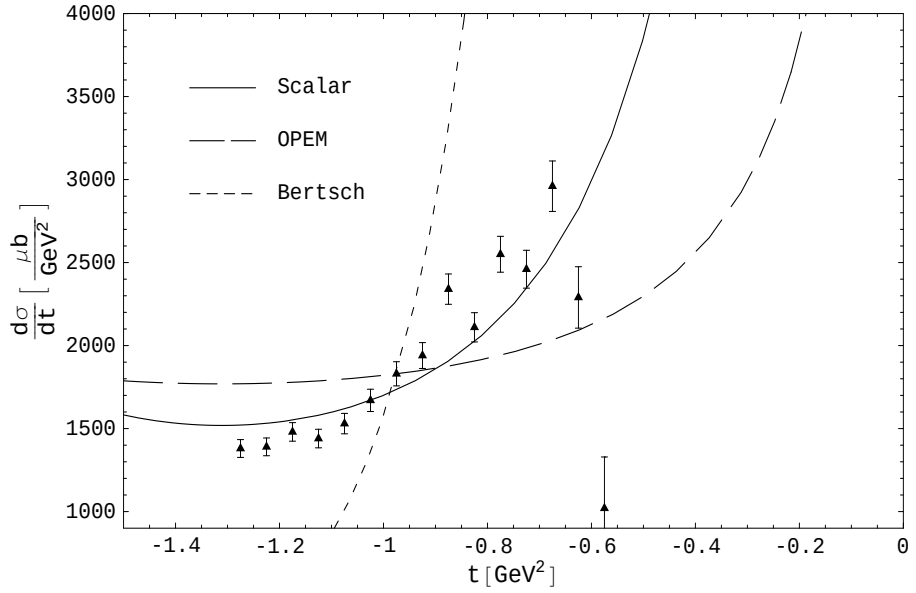

Figure C.16: Comparison of the theoretical curves for OPEM, scalar theory and the parameterization of Bertsch [18] to data from Jenkins *et al.* [22] at $p_{lab} = 2.139$ GeV.

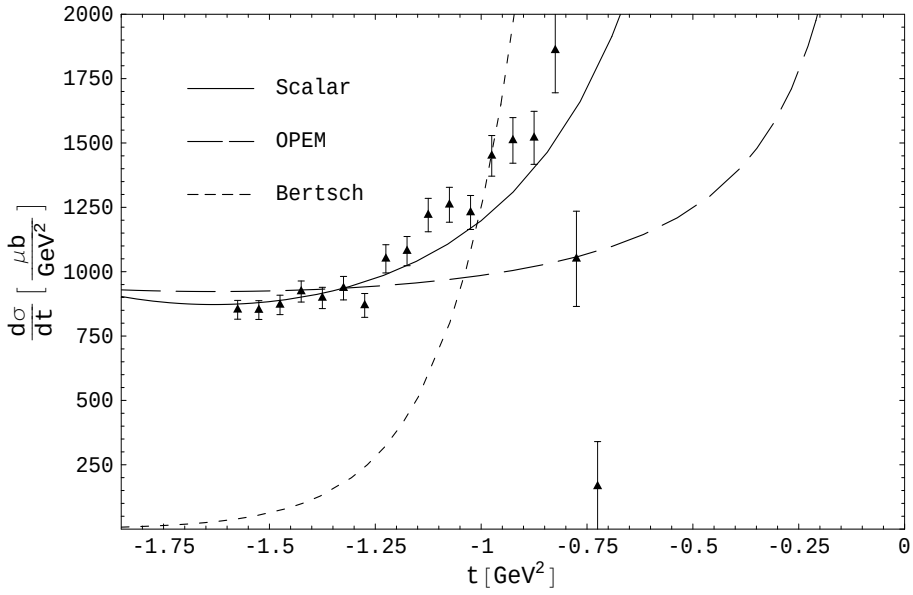

Figure C.17: Comparison of the theoretical curves for OPEM, scalar theory and the parameterization of Bertsch [18] to data from Jenkins *et al.* [22] at $p_{lab} = 2.508$ GeV.

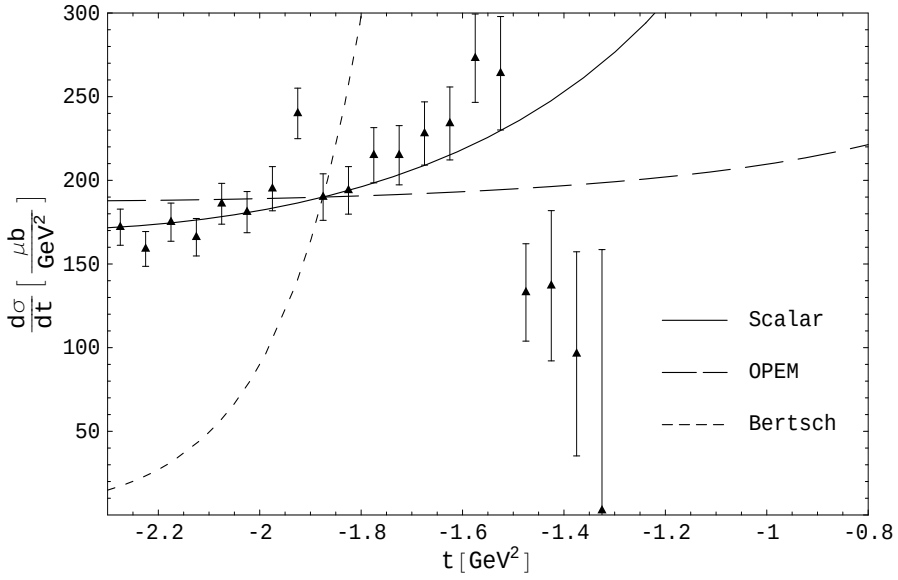

Figure C.18: Comparison of the theoretical curves for OPEM, scalar theory and the parameterization of Bertsch [18] to data from Jenkins *et al.* [22] at $p_{lab} = 3.410$ GeV.

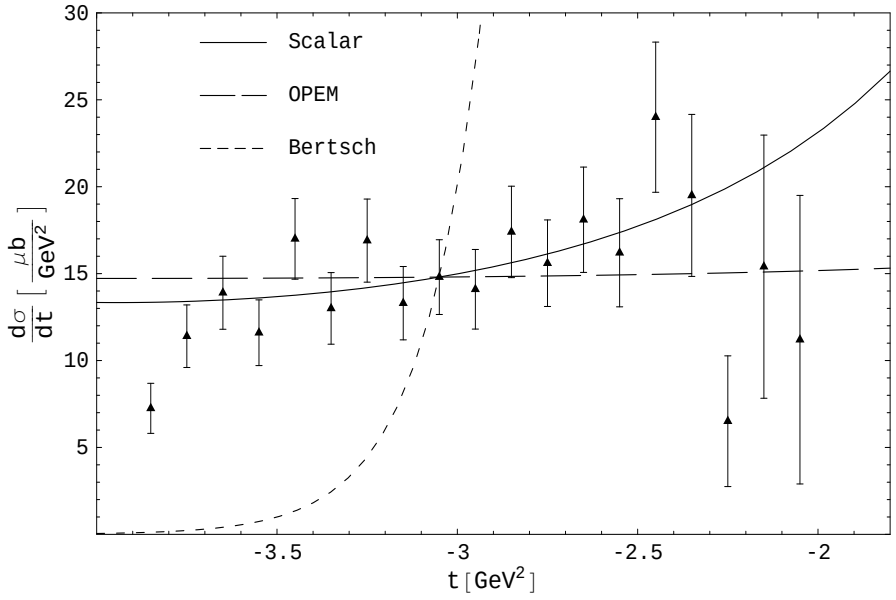

Figure C.19: Comparison of the theoretical curves for OPEM, scalar theory and the parameterization of Bertsch [18] to data from Jenkins *et al.* [22] at $p_{lab} = 5.055$ GeV.

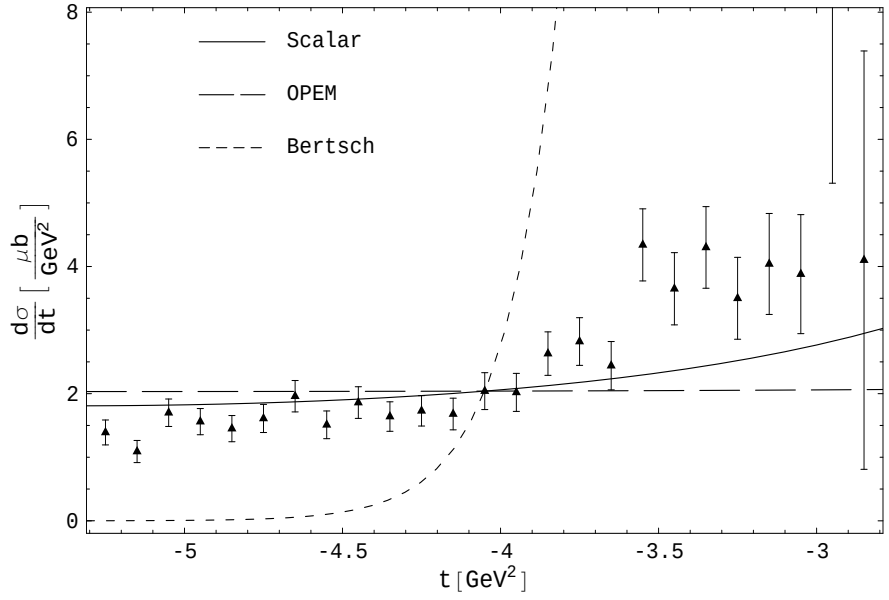

Figure C.20: Comparison of the theoretical curves for OPEM, scalar theory and the parameterization of Bertsch [18] to data from Jenkins *et al.* [22] at $p_{lab} = 6.57$ GeV.

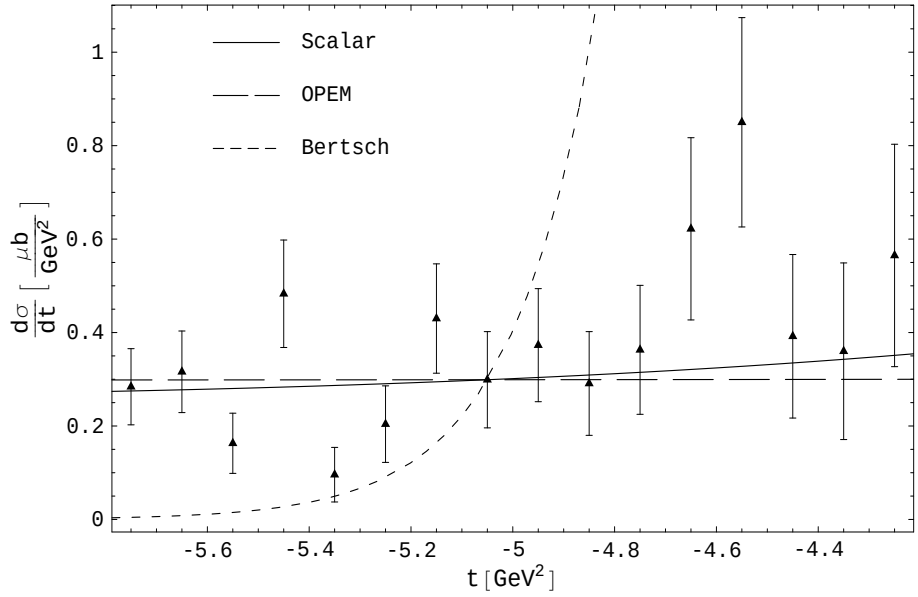

Figure C.21: Comparison of the theoretical curves for OPEM, scalar theory and the parameterization of Bertsch [18] to data from Jenkins *et al.* [22] at $p_{lab} = 8.022$ GeV.

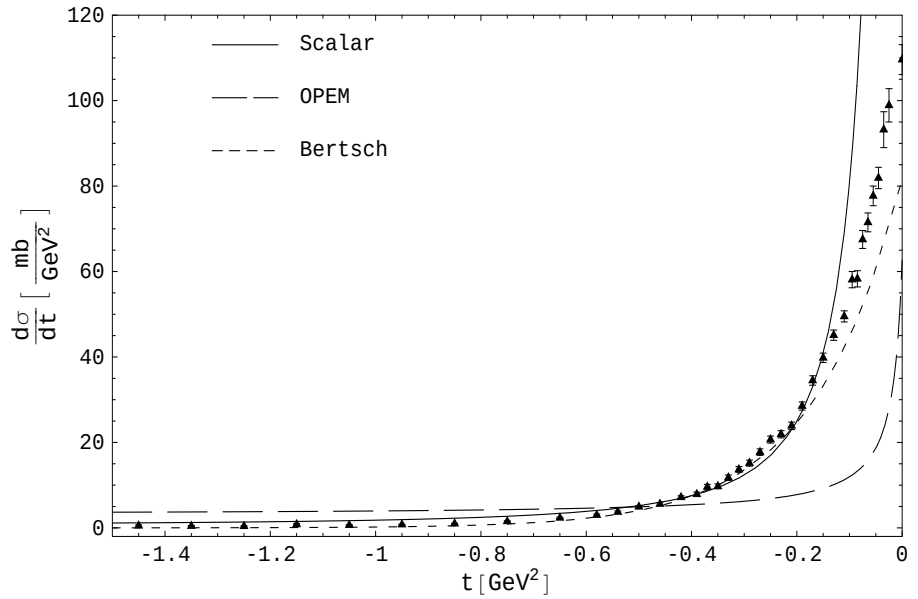

Figure C.22: Comparison of the theoretical curves for OPEM, scalar theory and the parameterization of Bertsch [18] to data from Ambats *et al.* [23] at $p_{lab} = 3.00$ GeV.

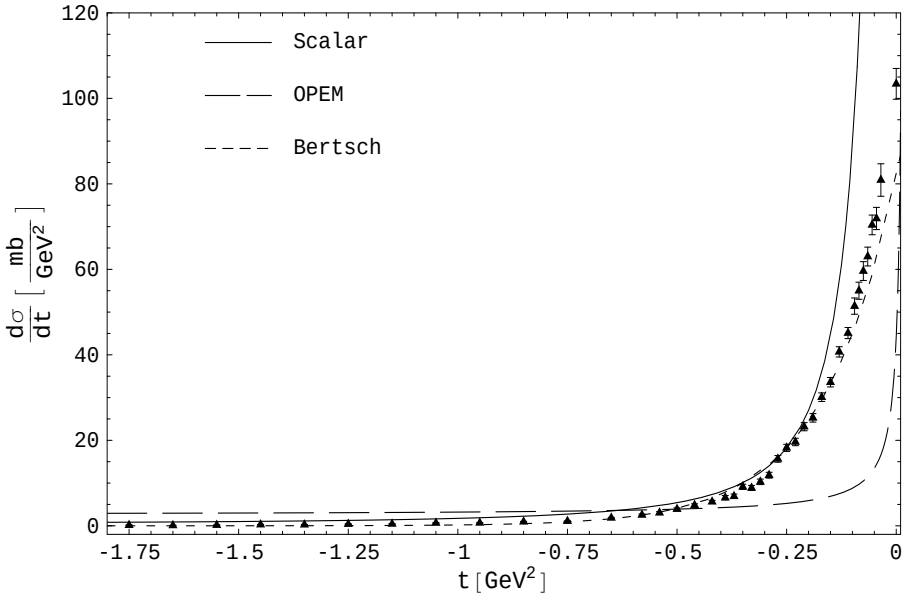

Figure C.23: Comparison of the theoretical curves for OPEM, scalar theory and the parameterization of Bertsch [18] to data from Ambats *et al.* [23] at $p_{lab} = 3.65$ GeV.

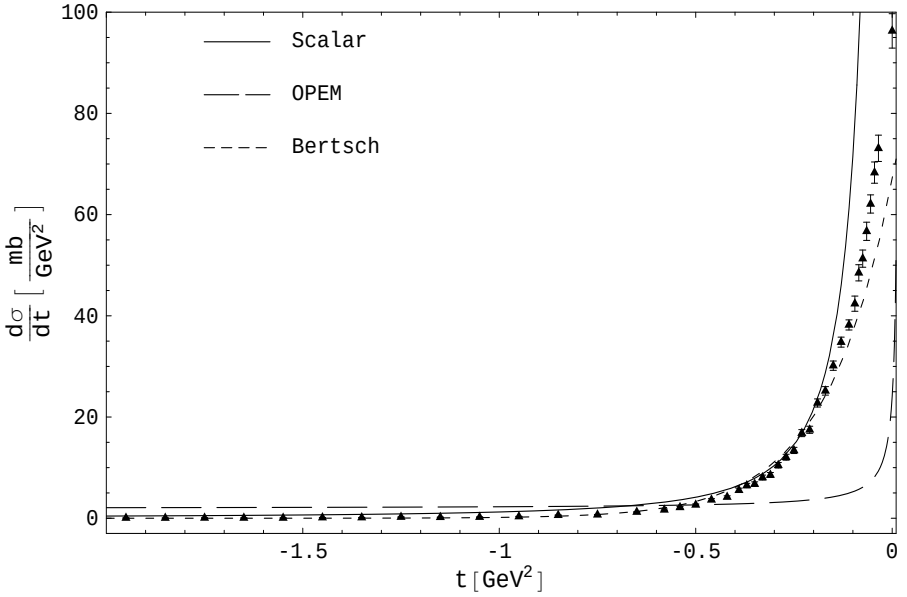

Figure C.24: Comparison of the theoretical curves for OPEM, scalar theory and the parameterization of Bertsch [18] to data from Ambats *et al.* [23] at $p_{lab} = 5.00$ GeV.

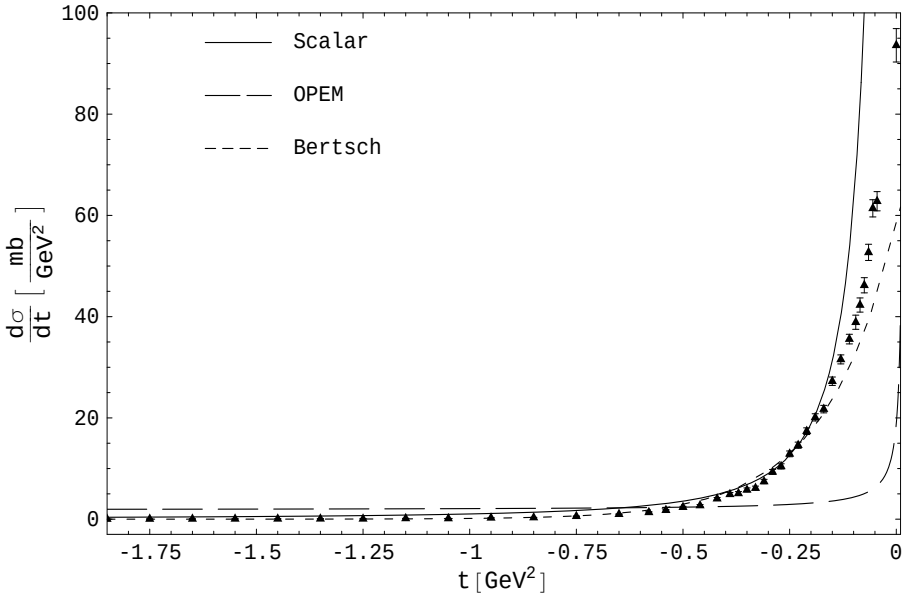

Figure C.25: Comparison of the theoretical curves for OPEM, scalar theory and the parameterization of Bertsch [18] to data from Ambats *et al.* [23] at $p_{lab} = 6.00$ GeV.

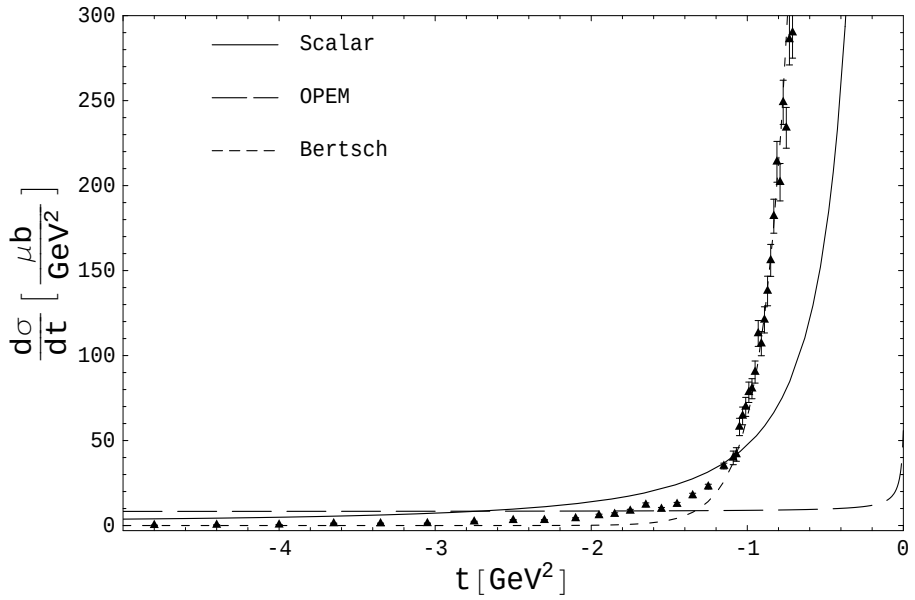

Figure C.26: Comparison of the theoretical curves for OPEM, scalar theory and the parameterization of Bertsch [18] to data from Baglin *et al.* [24] at $p_{lab} = 9.0$ GeV.

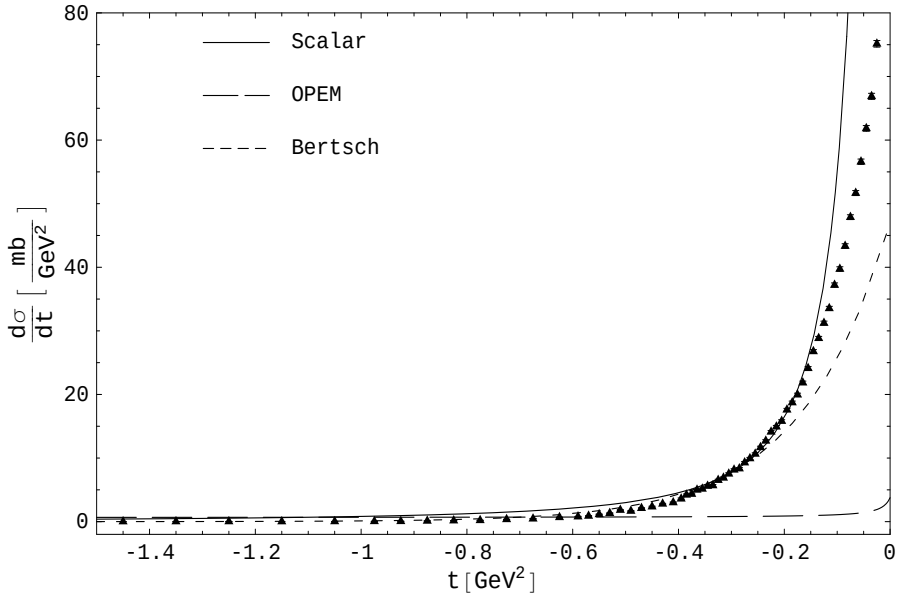

Figure C.27: Comparison of the theoretical curves for OPEM, scalar theory and the parameterization of Bertsch [18] to data from Brandenburg *et al.* [25] at $p_{lab} = 10.4$ GeV.

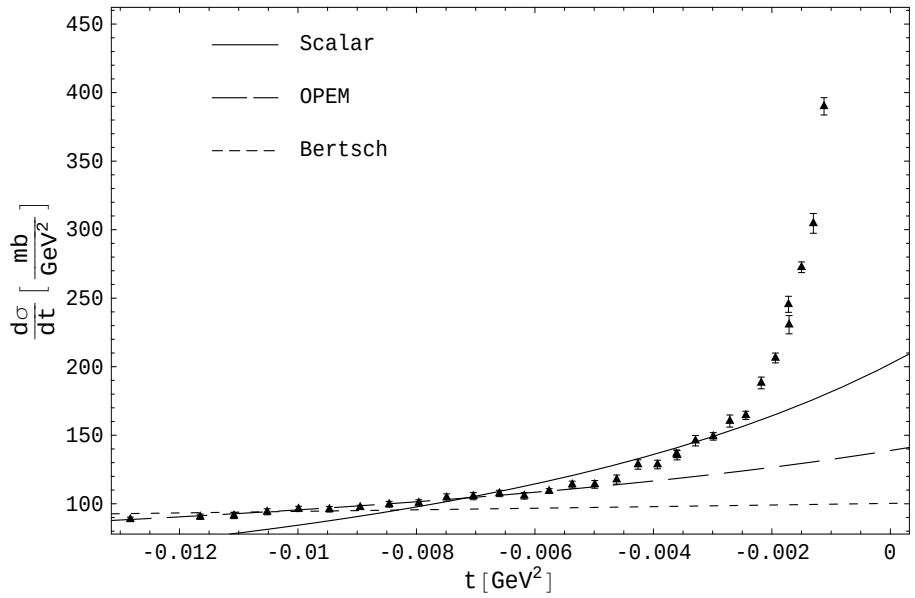

Figure C.28: Comparison of the theoretical curves for OPEM, scalar theory and the parameterization of Bertsch [18] to data from Beznogikh *et al.* [26] at $p_{lab} = 9.43$ GeV.

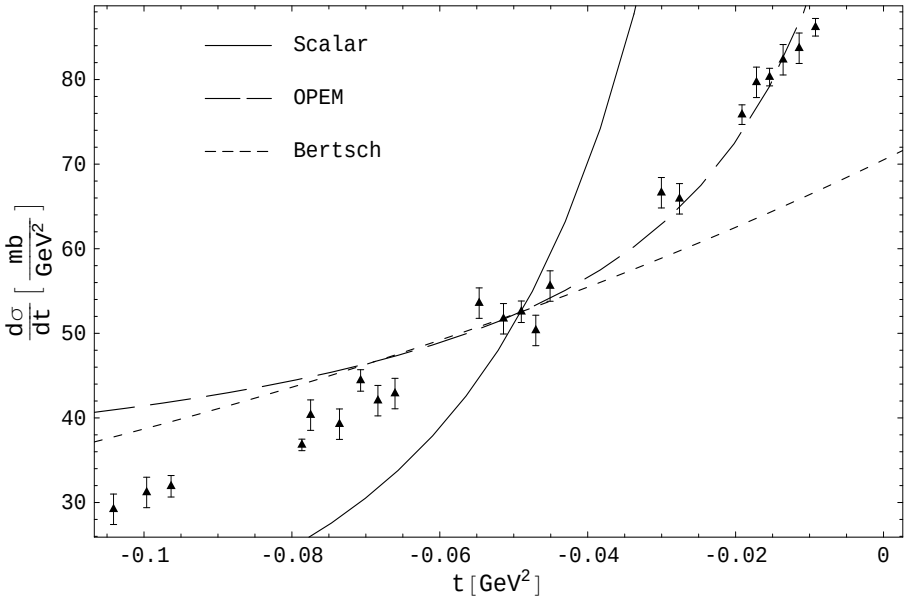

Figure C.29: Comparison of the theoretical curves for OPEM, scalar theory and the parameterization of Bertsch [18] to data from Beznogikh *et al.* [26] at $p_{lab} = 13.16$ GeV.

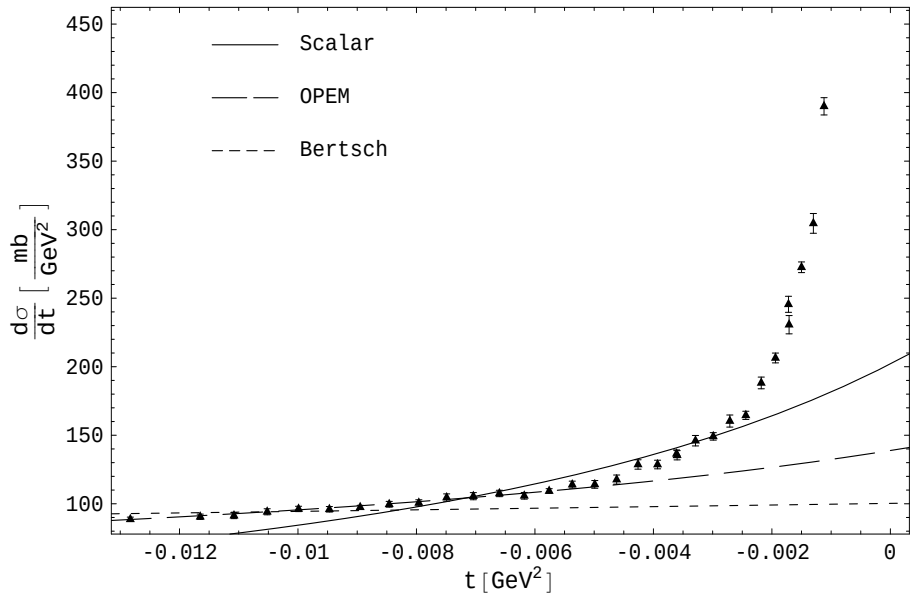

Figure C.30: Comparison of the theoretical curves for OPEM, scalar theory and the parameterization of Bertsch [18] to data from Beznogikh *et al.* [26] at $p_{lab} = 15.52$ GeV.

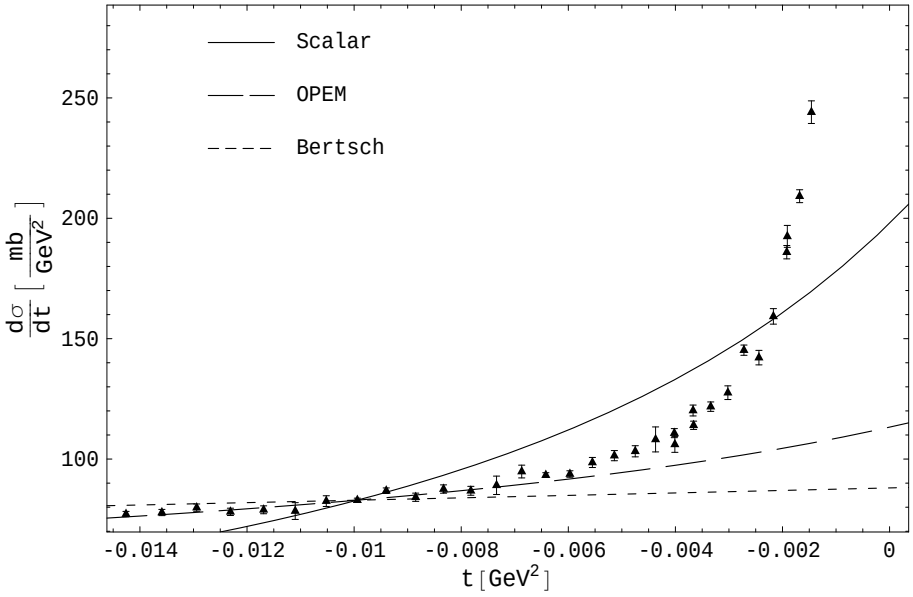

Figure C.31: Comparison of the theoretical curves for OPEM, scalar theory and the parameterization of Bertsch [18] to data from Beznogikh *et al.* [26] at $p_{lab} = 19.23$ GeV.

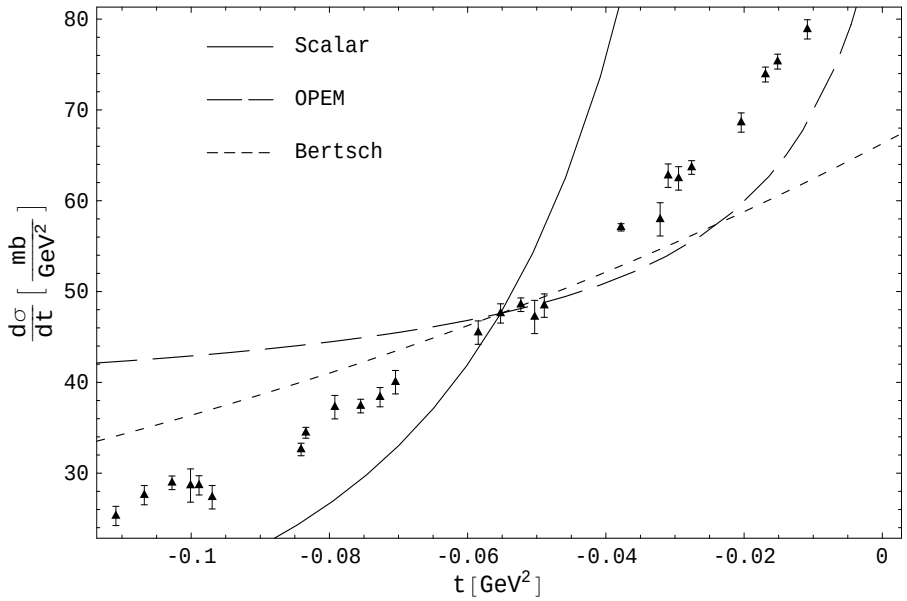

Figure C.32: Comparison of the theoretical curves for OPEM, scalar theory and the parameterization of Bertsch [18] to data from Beznogikh *et al.* [26] at $p_{lab} = 24.56$ GeV.

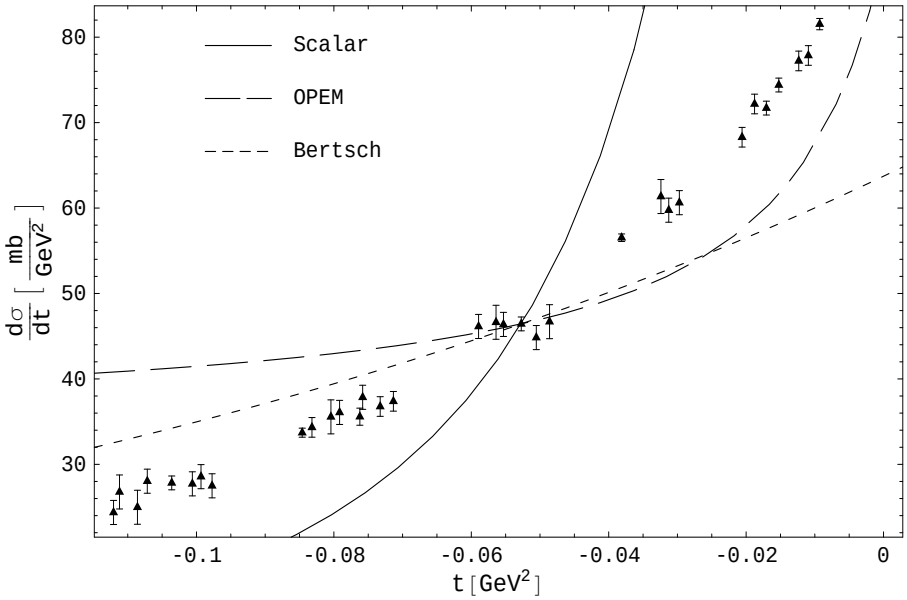

Figure C.33: Comparison of the theoretical curves for OPEM, scalar theory and the parameterization of Bertsch [18] to data from Beznogikh *et al.* [26] at $p_{lab} = 27.53$ GeV.

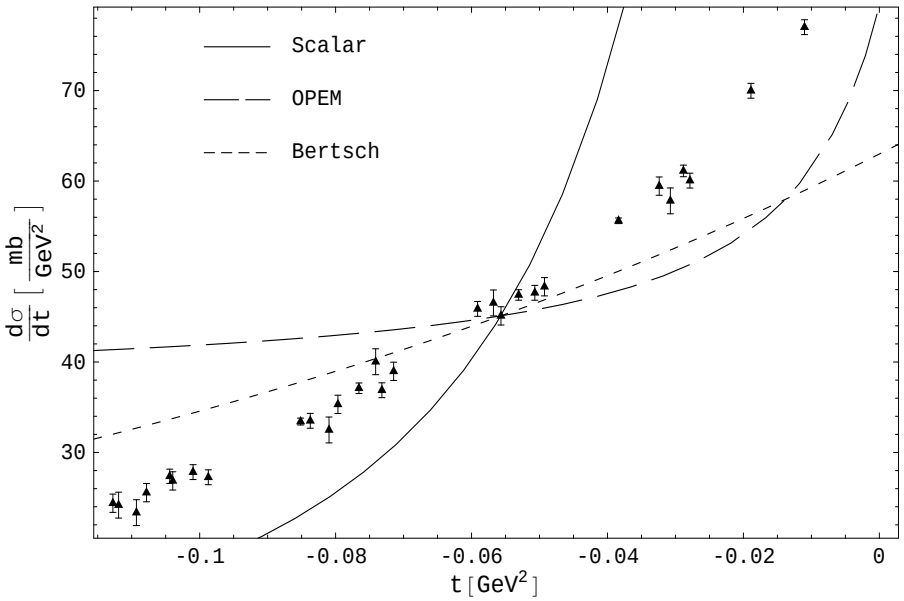

Figure C.34: Comparison of the theoretical curves for OPEM, scalar theory and the parameterization of Bertsch [18] to data from Beznogikh *et al.* [26] at $p_{lab} = 30.45$ GeV.

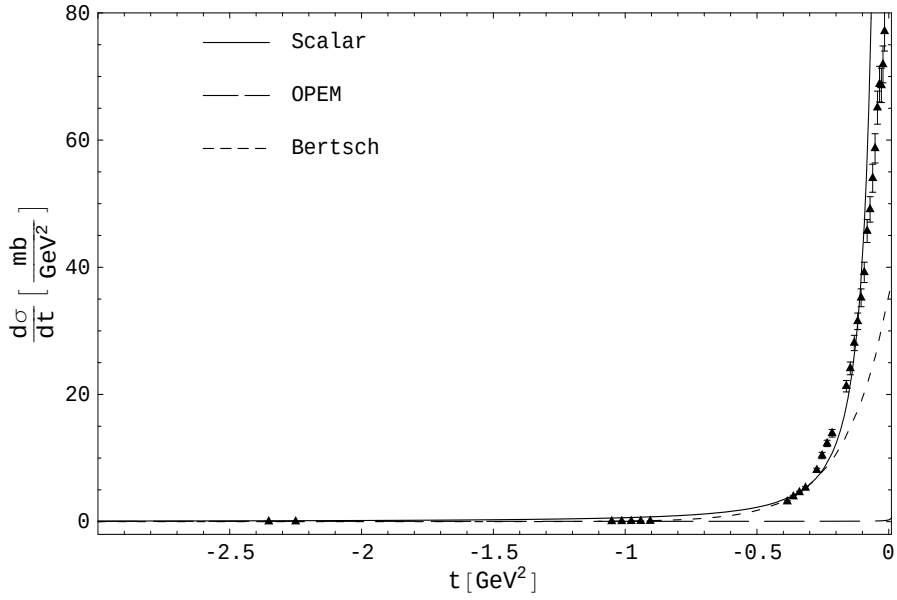

Figure C.35: Comparison of the theoretical curves for OPEM, scalar theory and the parameterization of Bertsch [18] to data from Edelstein *et al.* [27] at $p_{lab} = 9.900$ GeV.

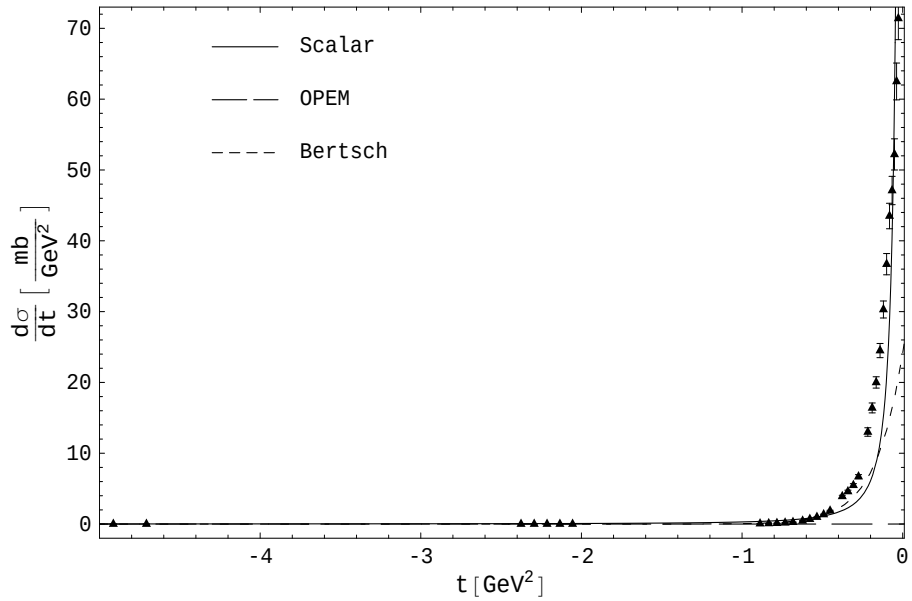

Figure C.36: Comparison of the theoretical curves for OPEM, scalar theory and the parameterization of Bertsch [18] to data from Edelstein *et al.* [27] at $p_{lab} = 15.100$ GeV.

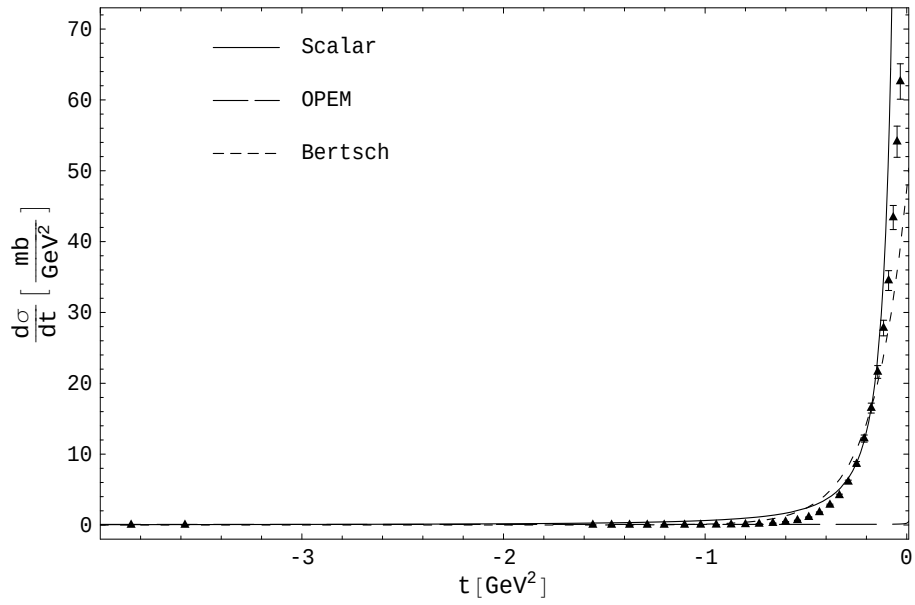

Figure C.37: Comparison of the theoretical curves for OPEM, scalar theory and the parameterization of Bertsch [18] to data from Edelstein *et al.* [27] at $p_{lab} = 20.000$ GeV.

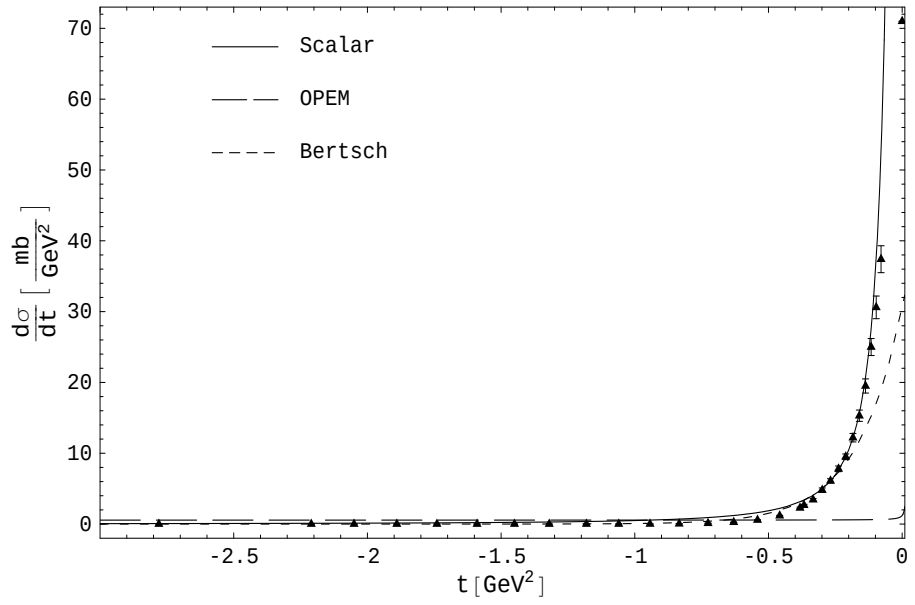

Figure C.38: Comparison of the theoretical curves for OPEM, scalar theory and the parameterization of Bertsch [18] to data from Edelstein *et al.* [27] at $p_{lab} = 29.700$ GeV.

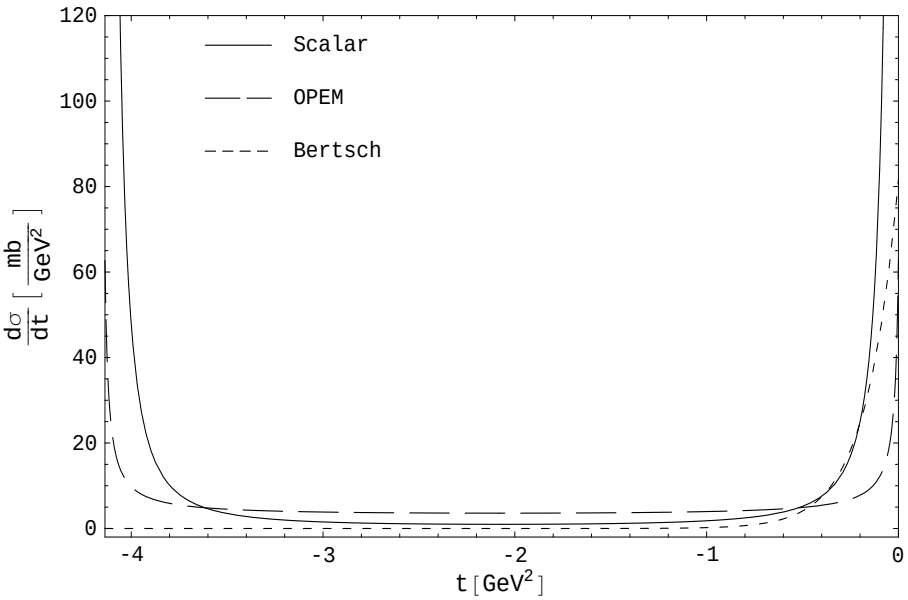

Figure C.39: Comparison of the theoretical curves for OPEM, scalar theory and the parameterization of Bertsch [18] for the full physical range of t at $p_{lab} = 3.00$ GeV.

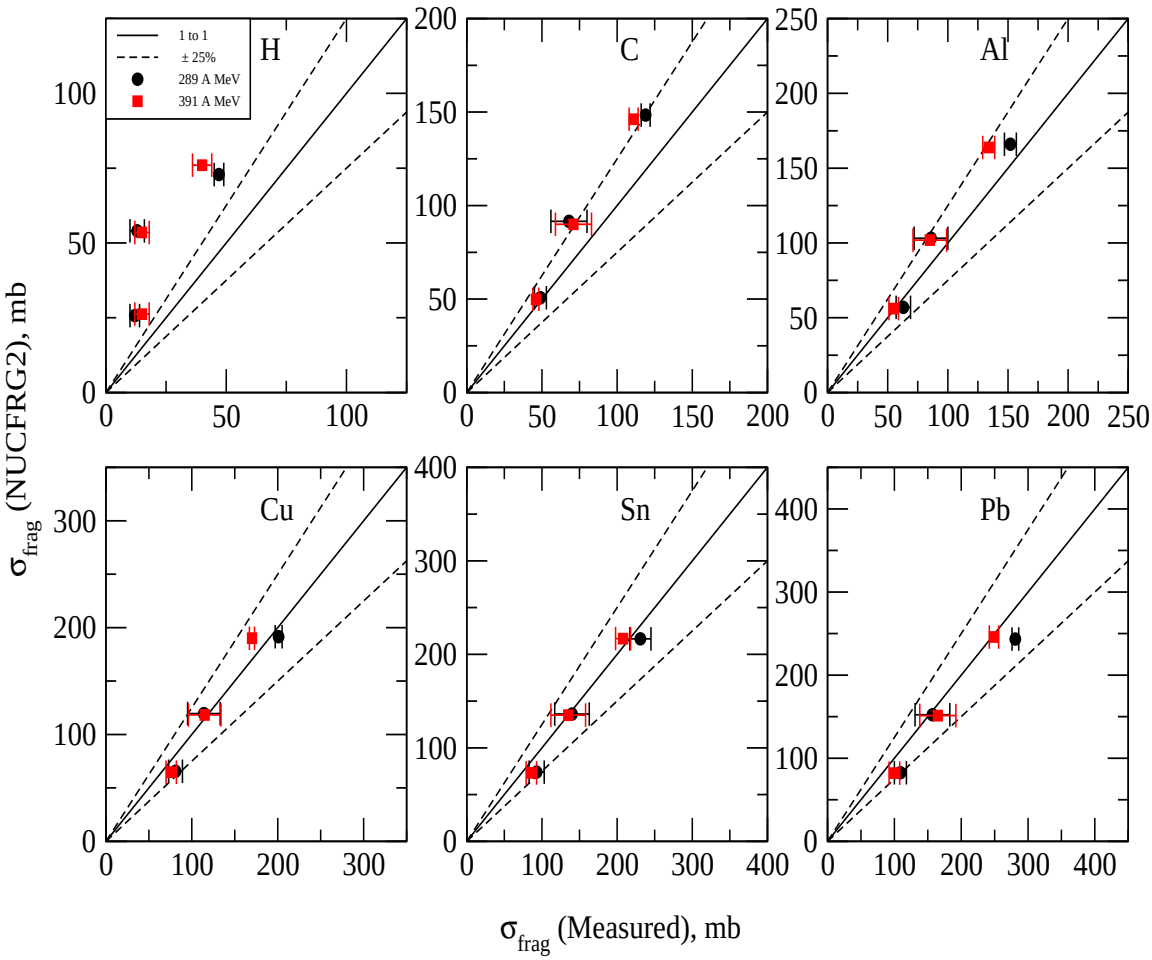

Figure C.40: Comparison of the NUCFRG2 results and the experimental data from Reference [59] for a ^{12}C beam incident on the 6 standard targets H, C, Al, Cu, Sn, Pb.

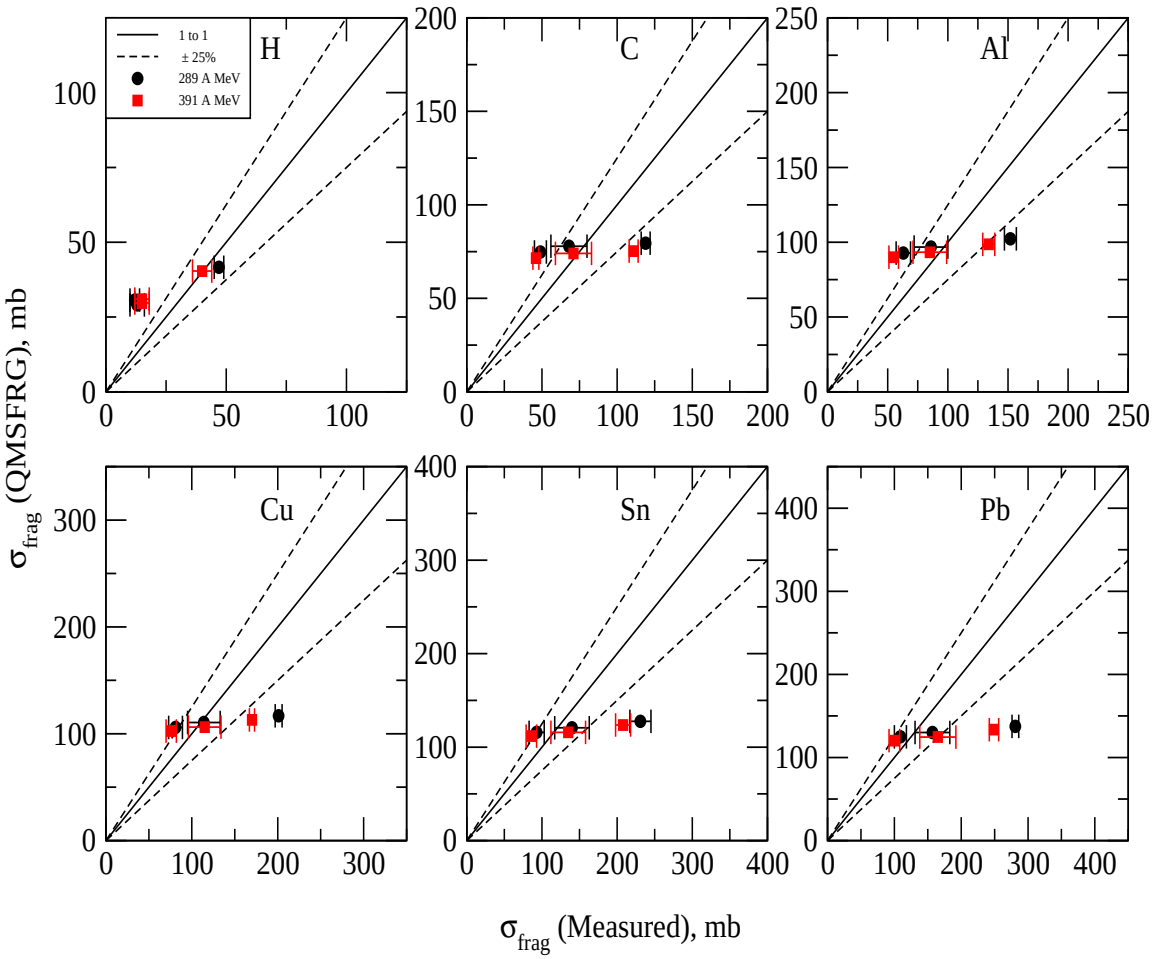

Figure C.41: Comparison of the QMSFRG interpolation results and the experimental data from Reference [59] for a ^{12}C beam incident on the 6 standard targets H, C, Al, Cu, Sn, Pb.

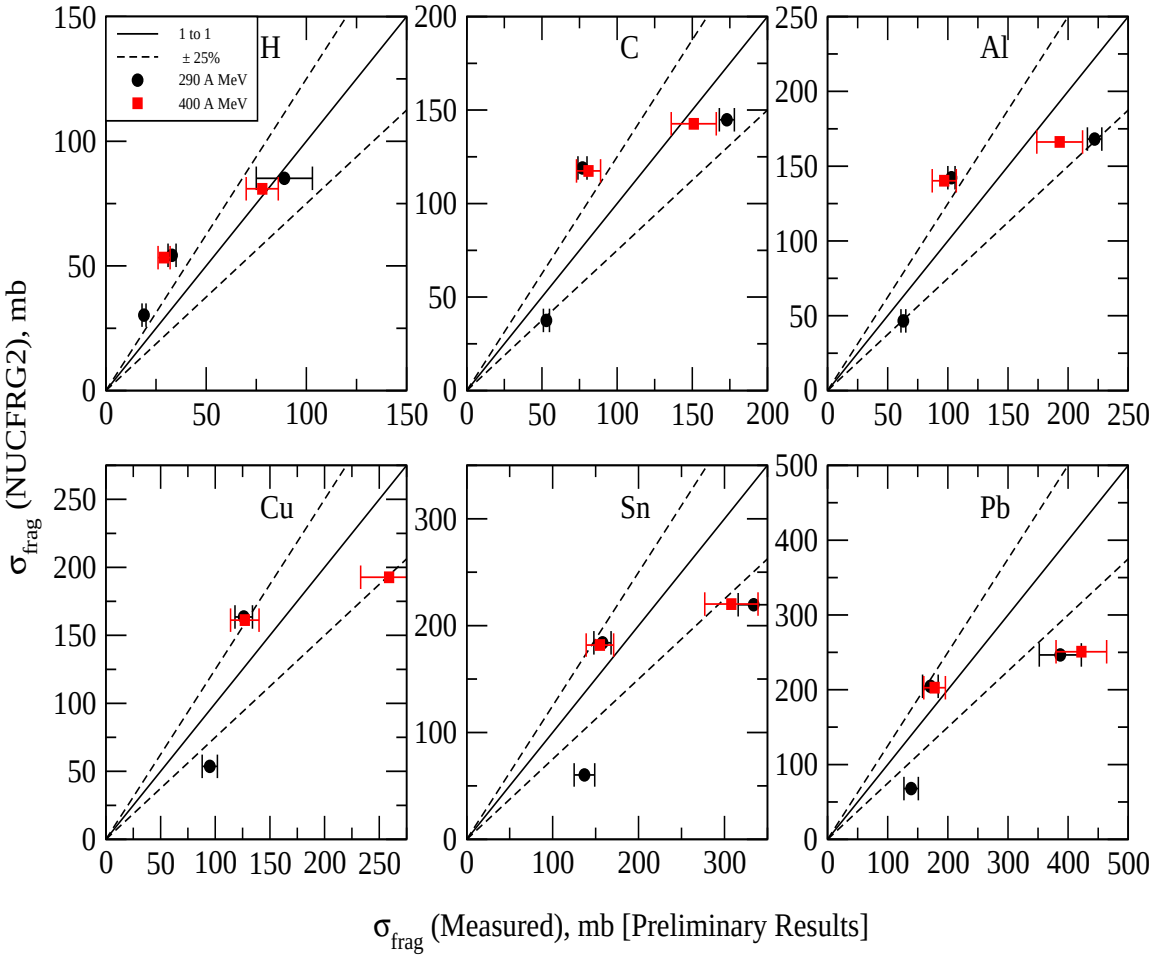

Figure C.42: Comparison of the NUCFRG2 results and the experimental data from Reference [62] for a ^{14}N beam incident on the 6 standard targets H, C, Al, Cu, Sn, Pb.

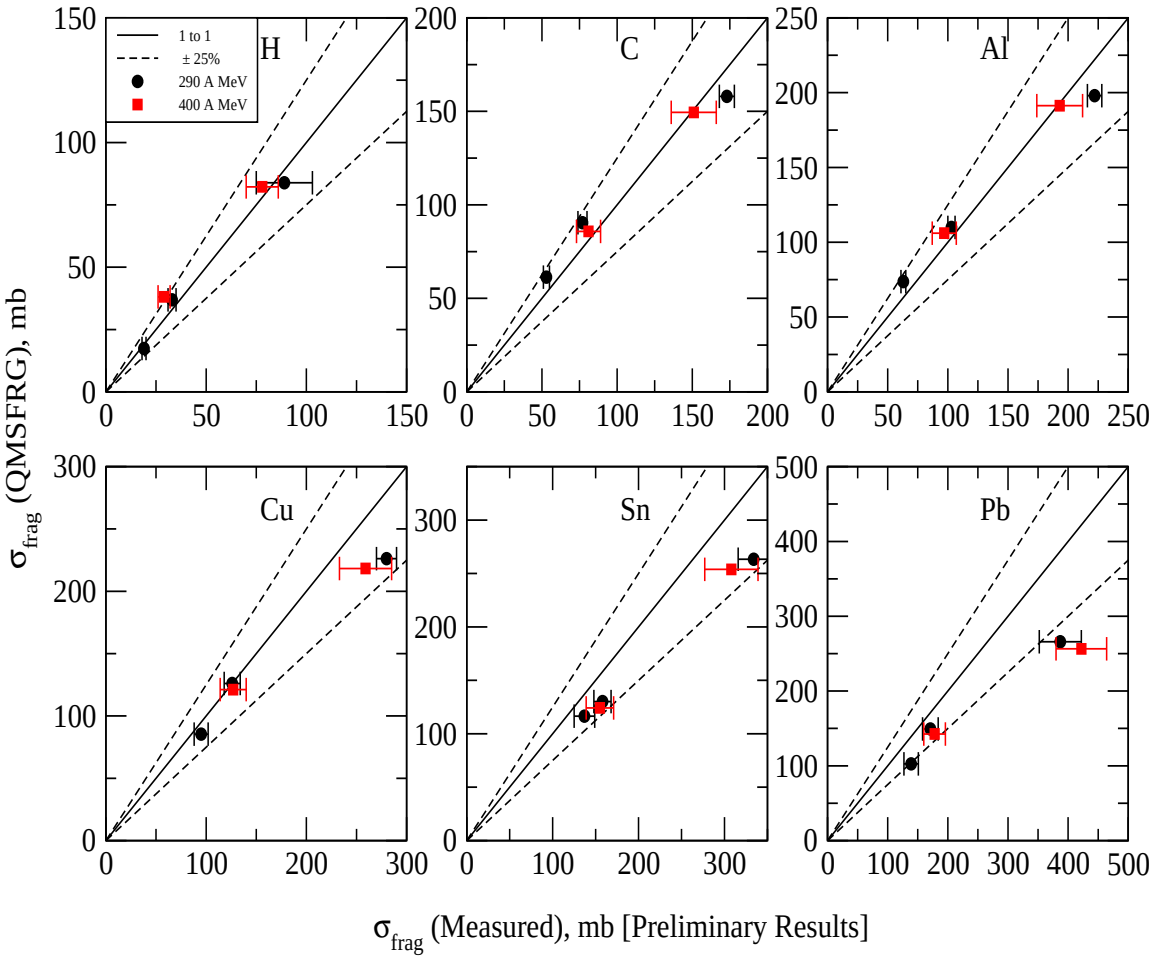

Figure C.43: Comparison of the QMSFRG interpolation results and the experimental data from Reference [62] for a ^{14}N incident beam on the 6 standard targets H, C, Al, Cu, Sn, Pb.

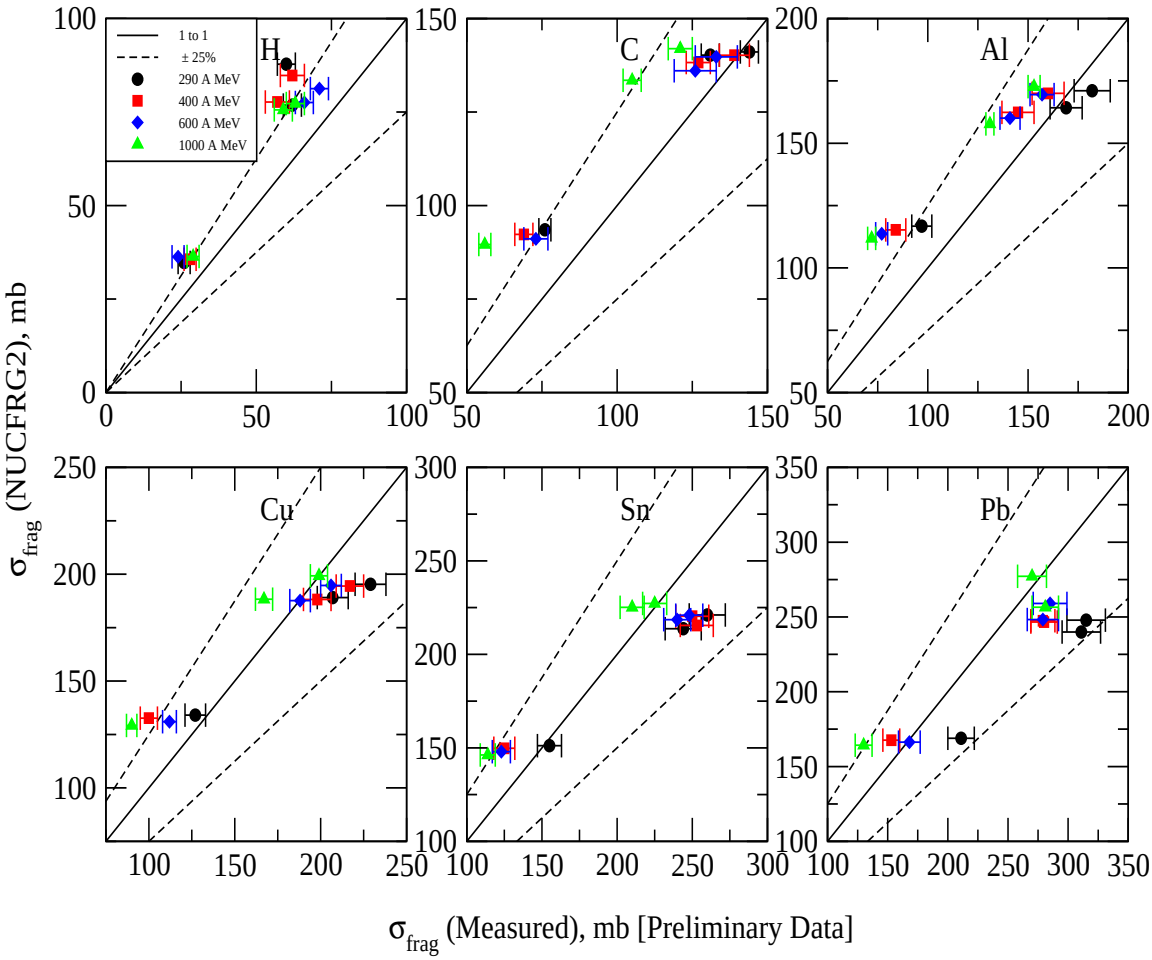

Figure C.44: Comparison of the NUCFRG2 results and the experimental data from Reference [62] for a ^{16}O beam incident on the 6 standard targets H, C, Al, Cu, Sn, Pb.

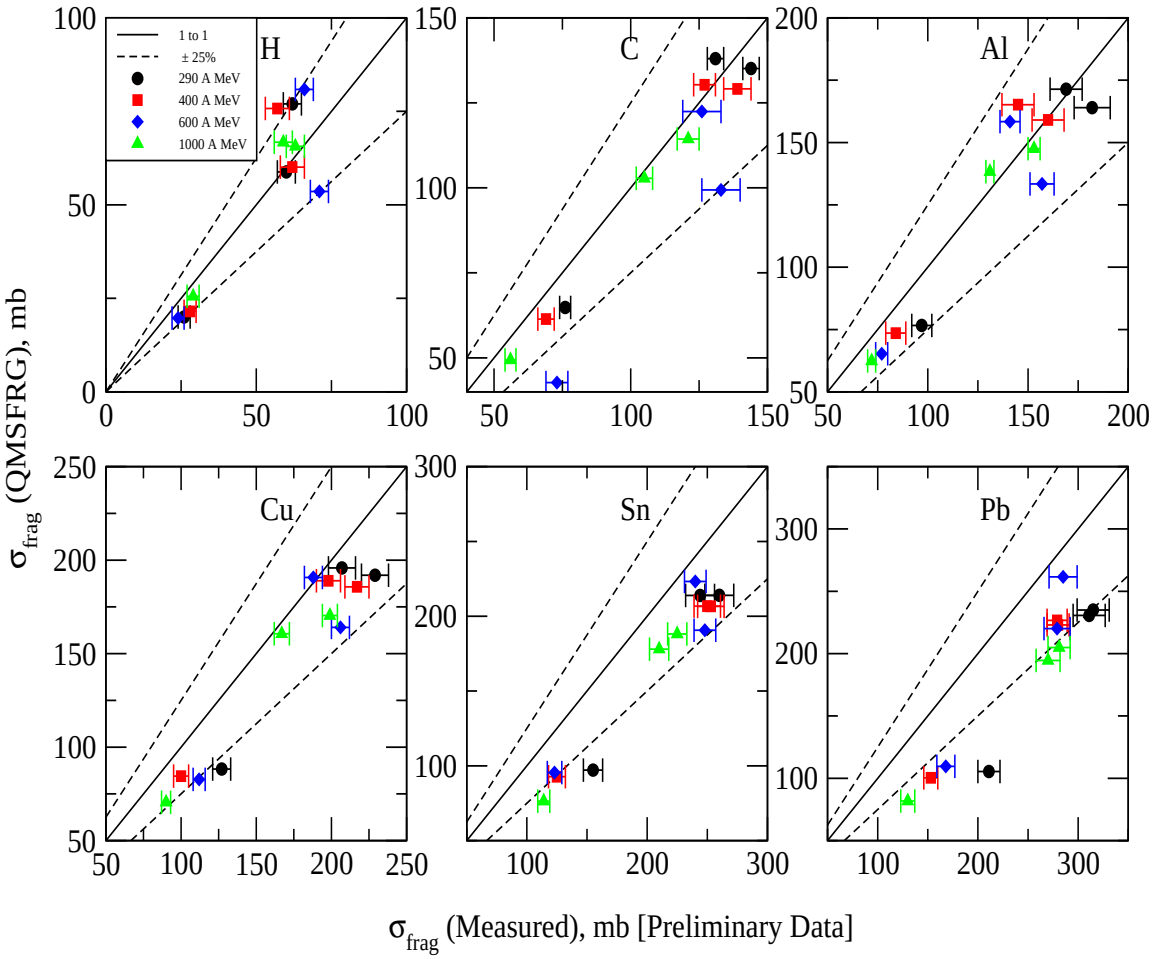

Figure C.45: Comparison of the QMSFRG interpolation results and the experimental data from Reference [62] for a ^{16}O beam incident on the 6 standard targets H, C, Al, Cu, Sn, Pb.

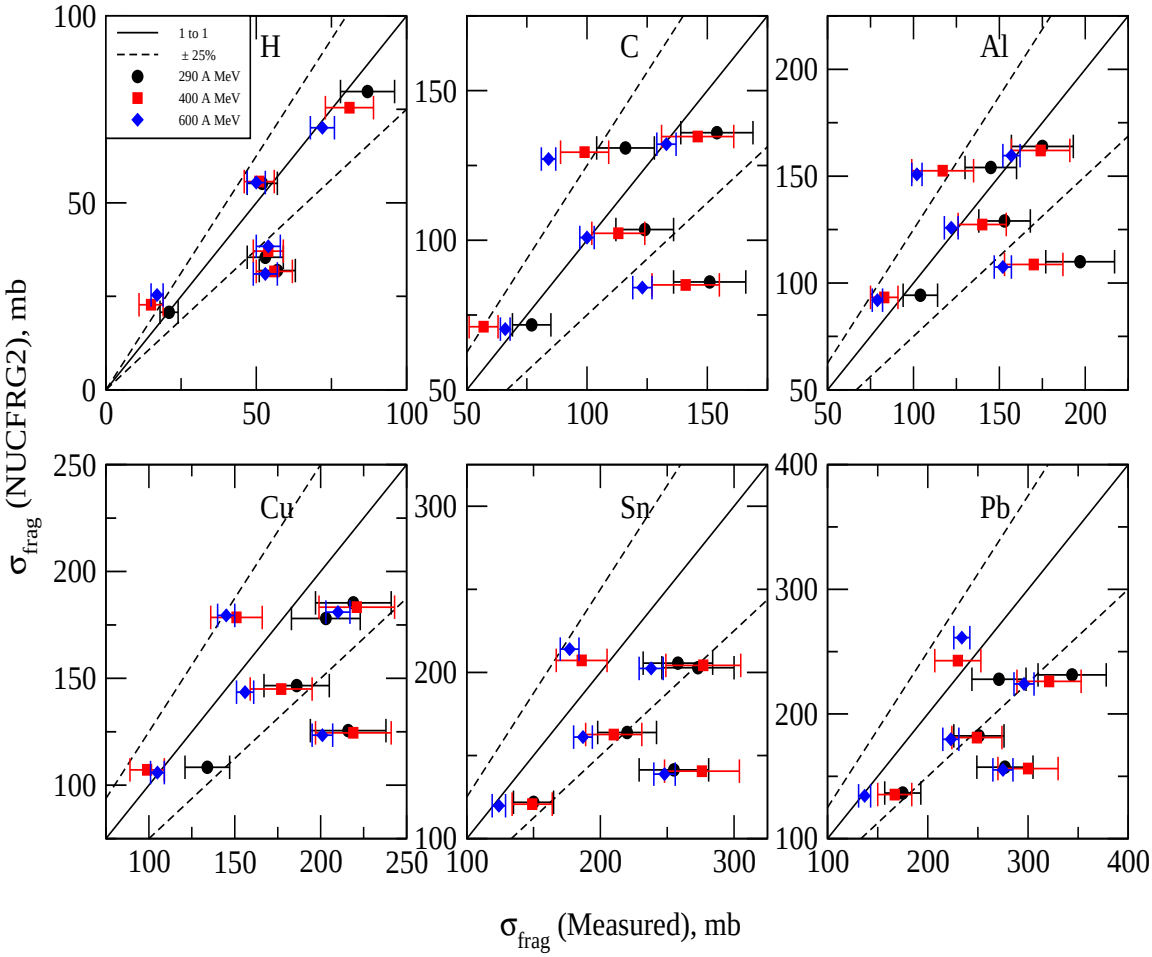

Figure C.46: Comparison of the NUCFRG2 results and the experimental data from References [57] and [62] for a ^{20}Ne beam incident on the 6 standard targets H, C, Al, Cu, Sn, Pb.

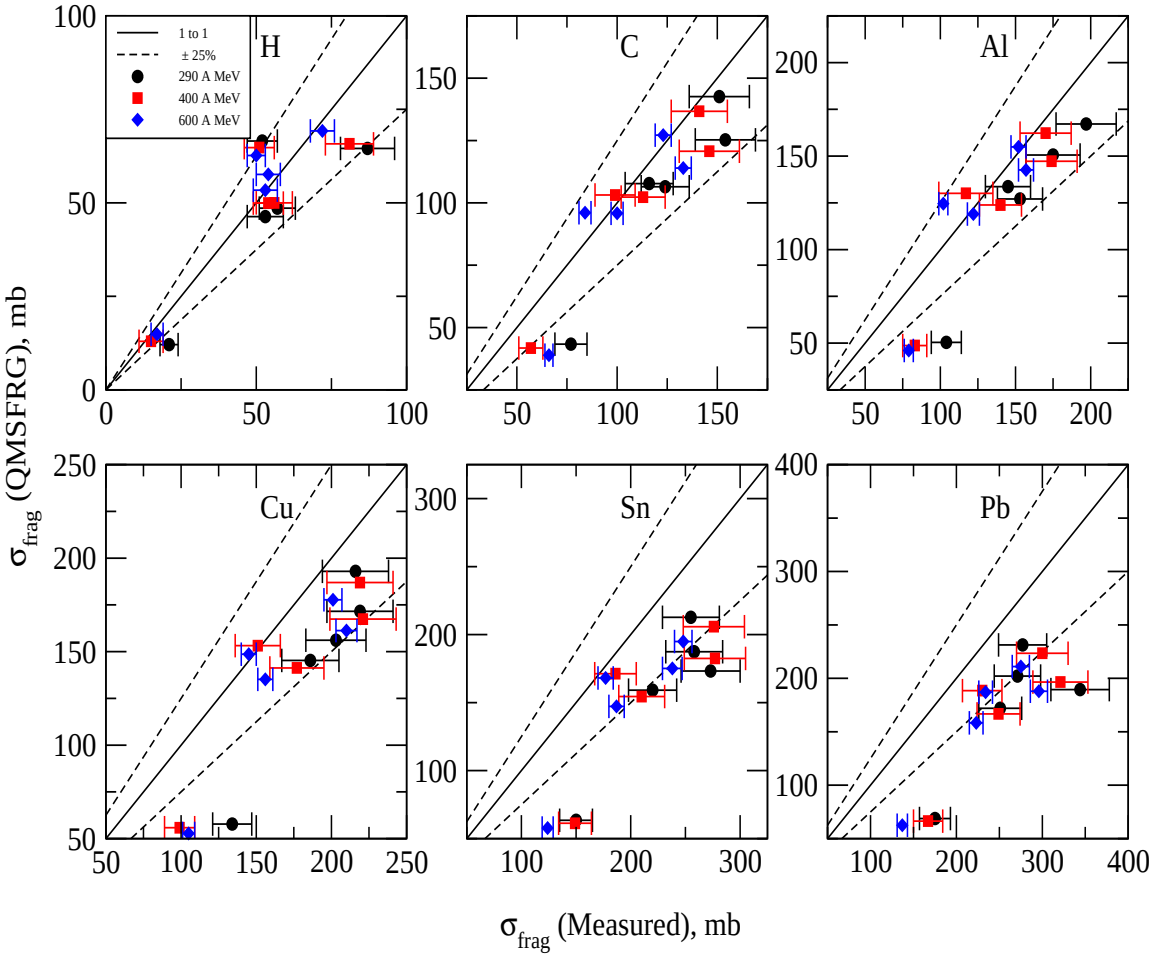

Figure C.47: Comparison of the QMSFRG interpolation results and the experimental data from References [57] and [62] for a ^{20}Ne beam incident on the 6 standard targets H, C, Al, Cu, Sn, Pb.

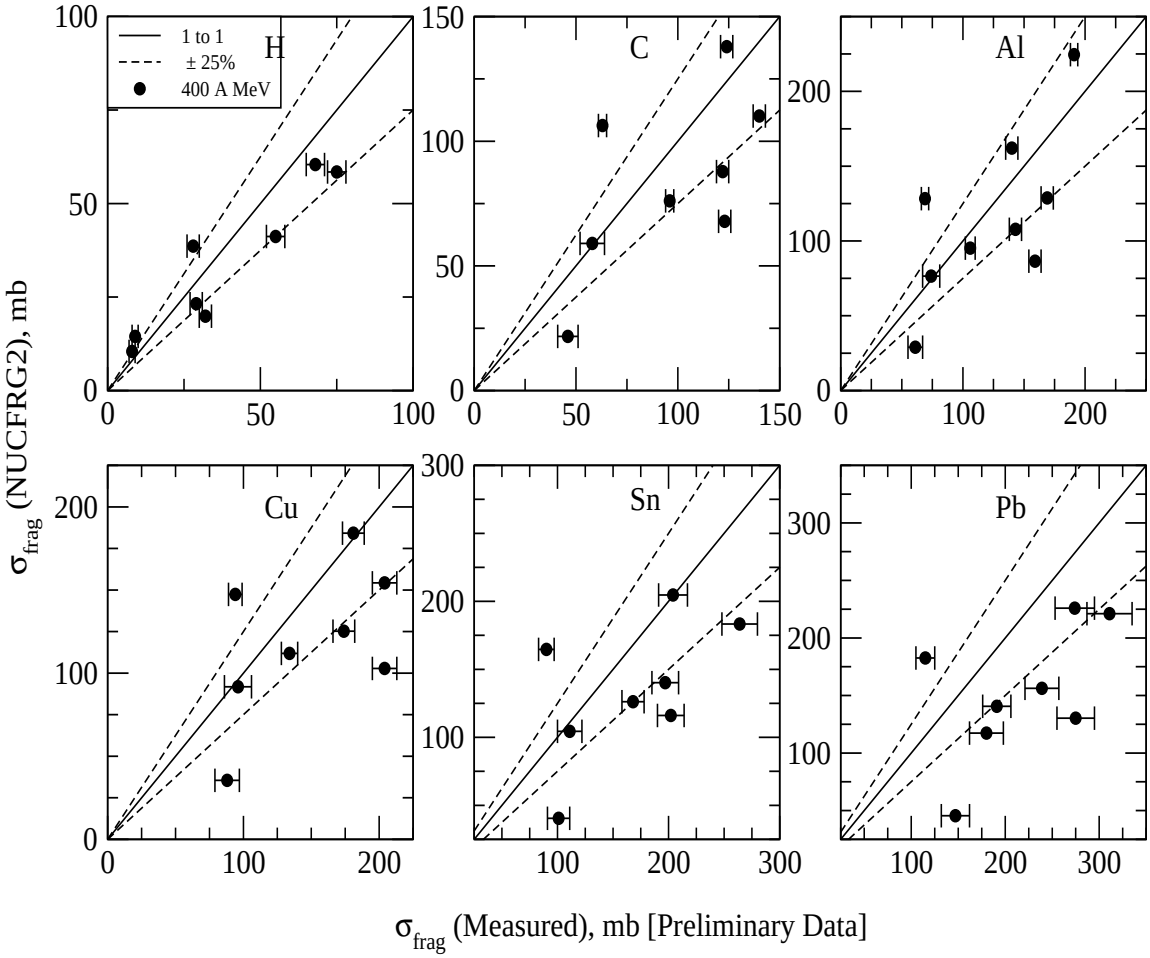

Figure C.48: Comparison of the NUCFRG2 results and the experimental data from Reference [62] for a ^{24}Mg beam incident on the 6 standard targets H, C, Al, Cu, Sn, Pb.

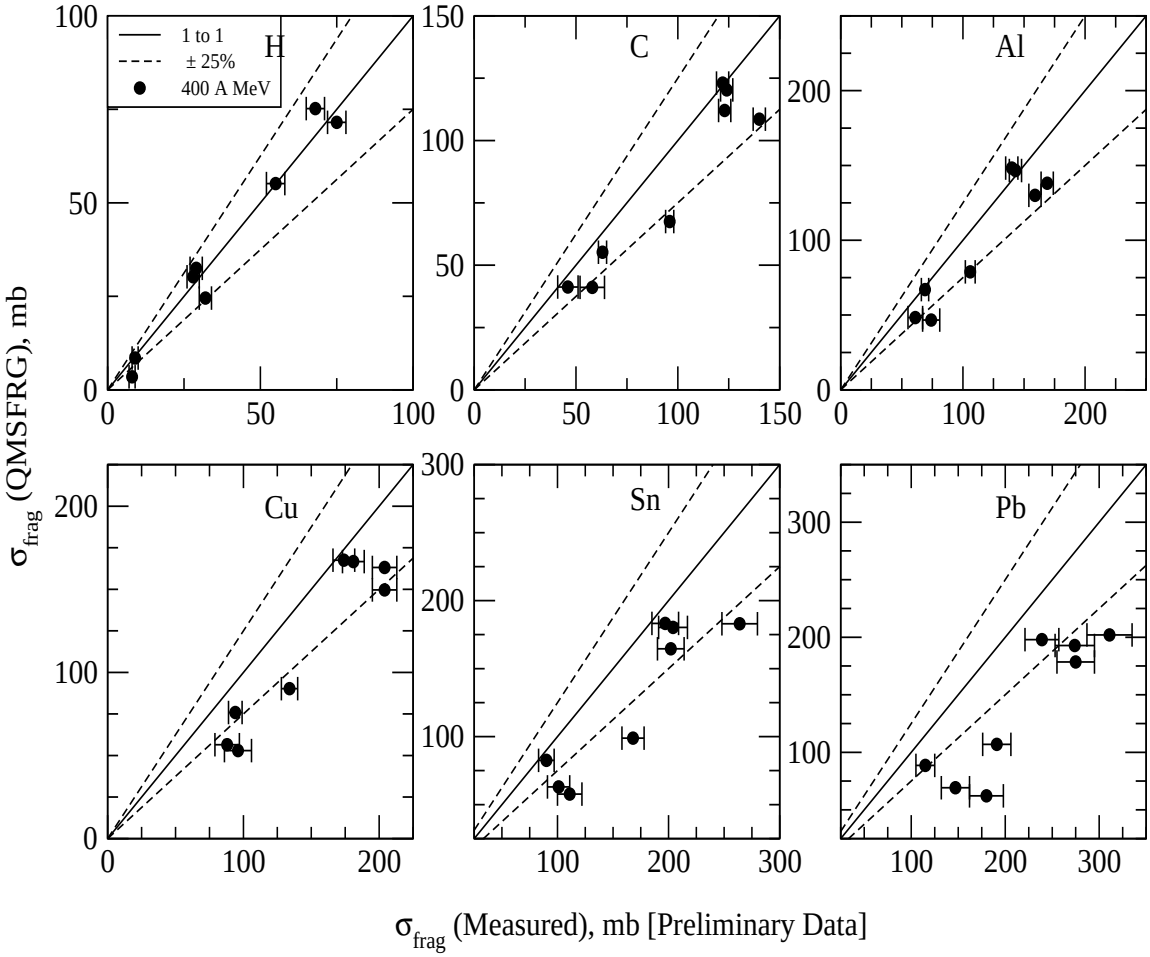

Figure C.49: Comparison of the QMSFRG interpolation results and the experimental data from Reference [62] for a ^{24}Mg beam incident on the 6 standard targets H, C, Al, Cu, Sn, Pb.

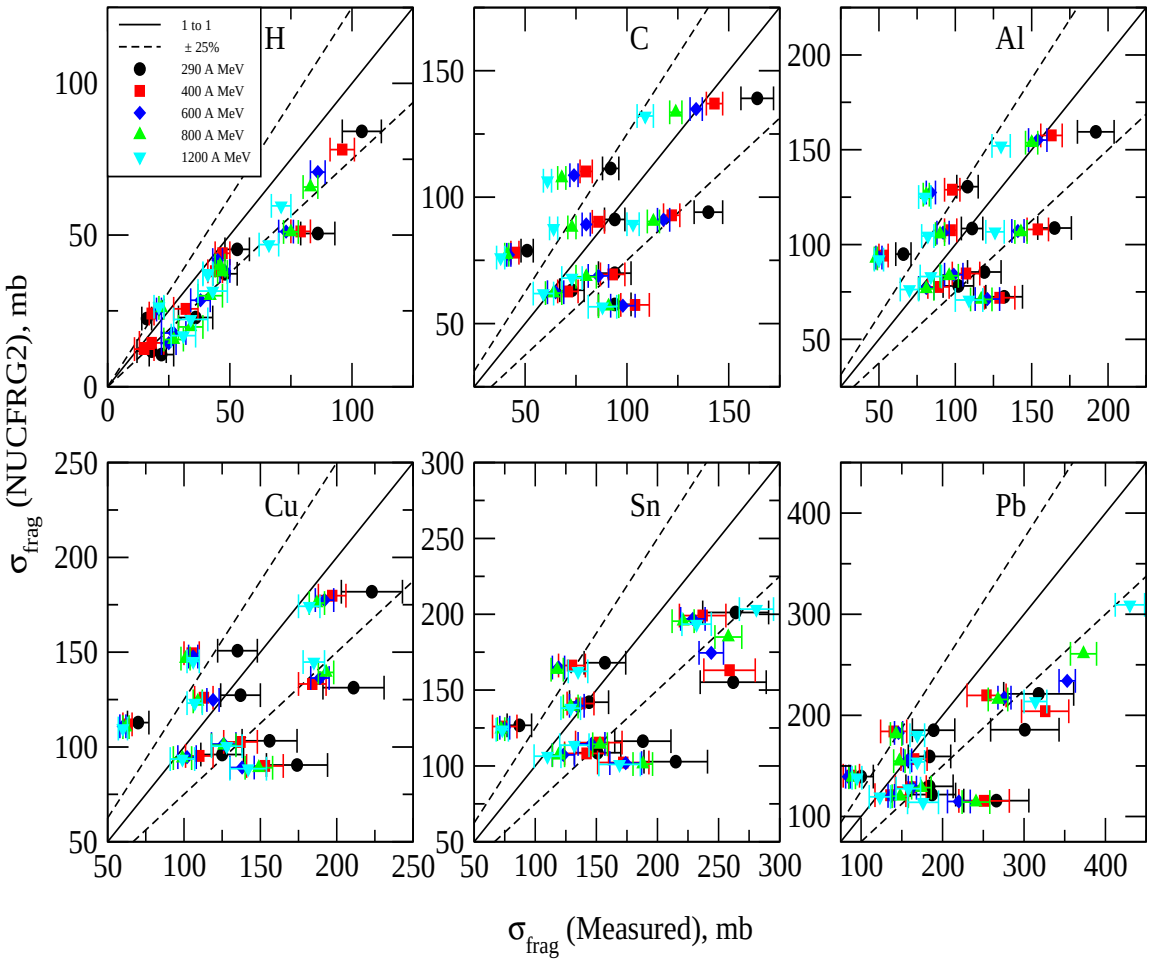

Figure C.50: Comparison of the NUCFRG2 results and the experimental data from Reference [60] for a ^{28}Si beam incident on the 6 standard targets H, C, Al, Cu, Sn, Pb.

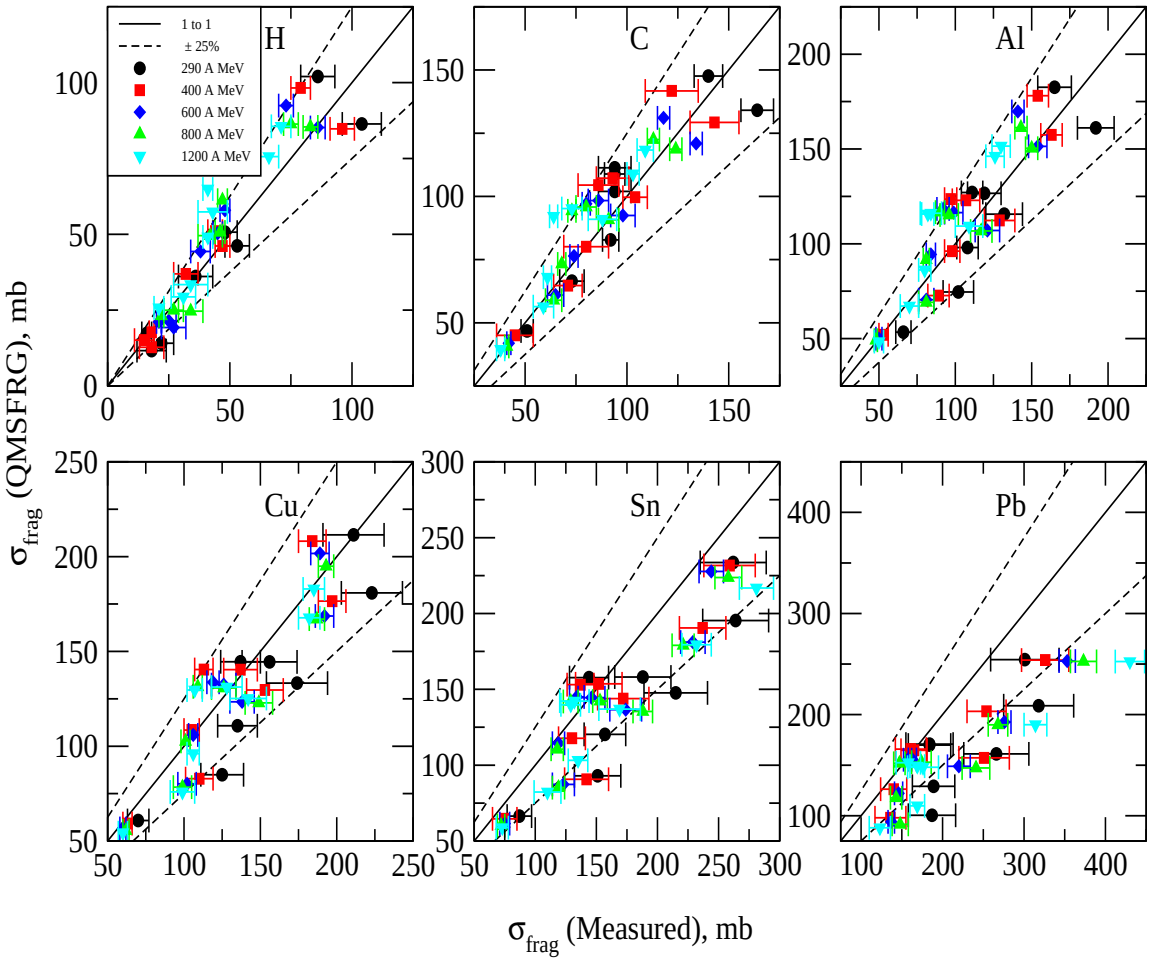

Figure C.51: Comparison of the QMSFRG interpolation results and the experimental data from Reference [60] for a ^{28}Si beam incident on the 6 standard targets H, C, Al, Cu, Sn, Pb.

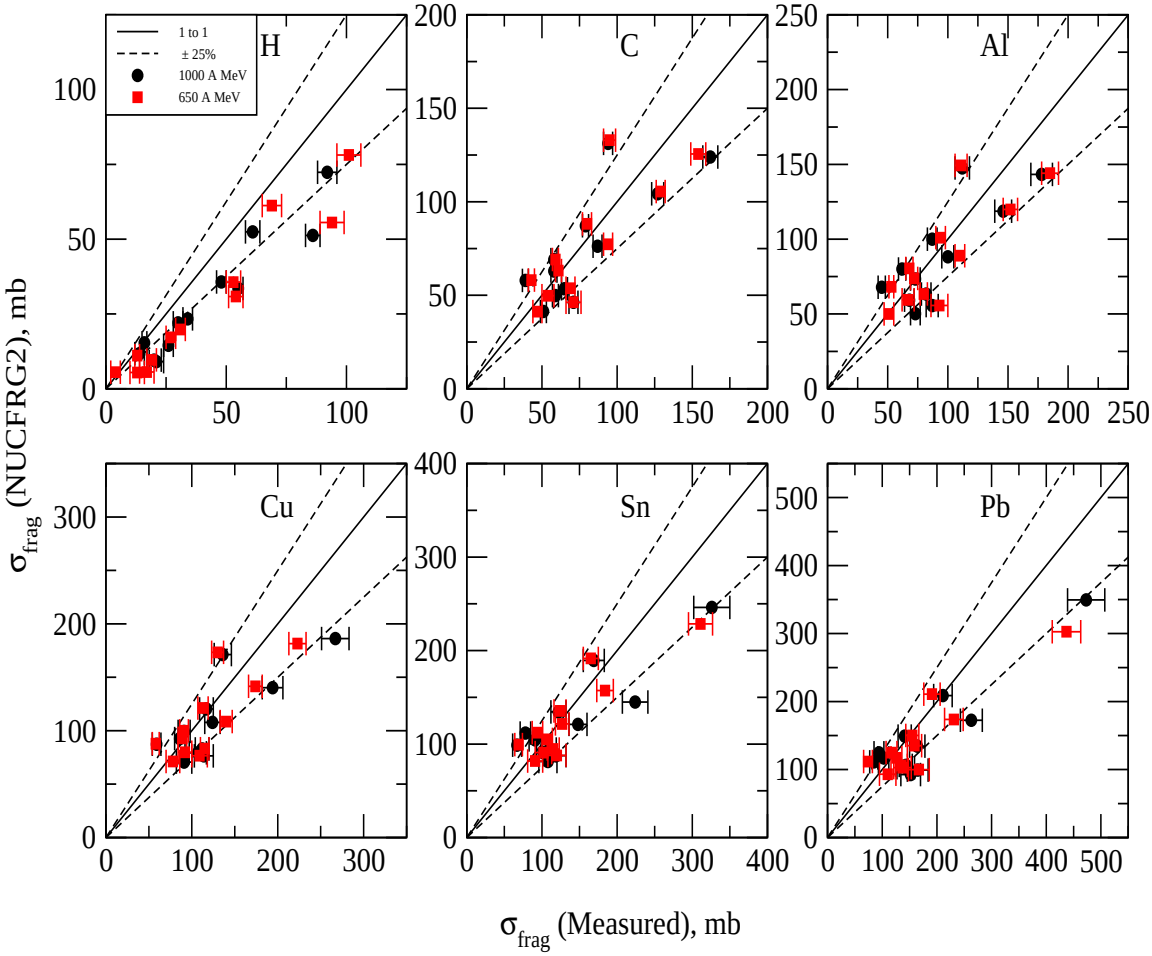

Figure C.52: Comparison of the NUCFRG2 results and the experimental data from Reference [62] for a ^{35}Cl beam incident on the 6 standard targets H, C, Al, Cu, Sn, Pb.

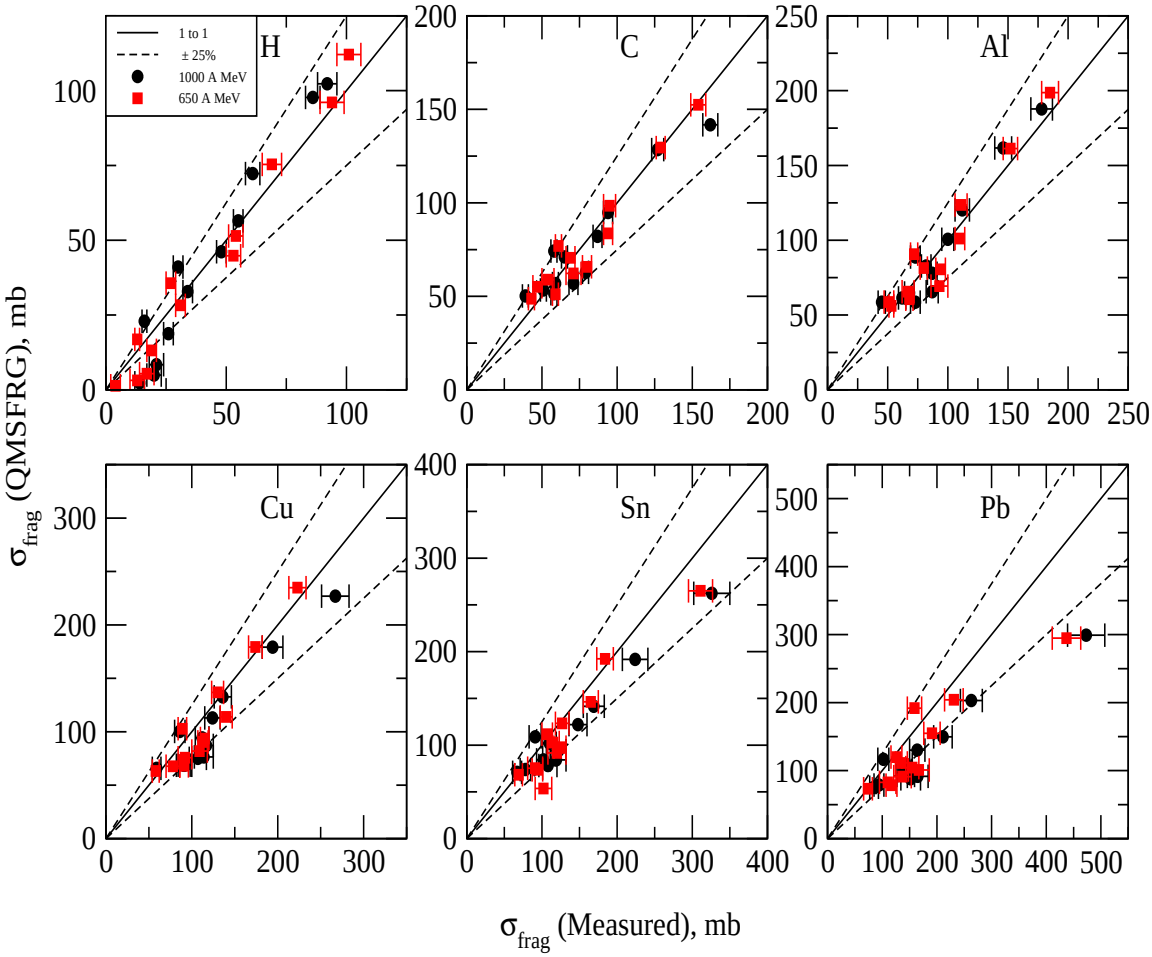

Figure C.53: Comparison of the QMSFRG interpolation results and the experimental data from Reference [62] for a ^{35}Cl beam incident on the 6 standard targets H, C, Al, Cu, Sn, Pb.

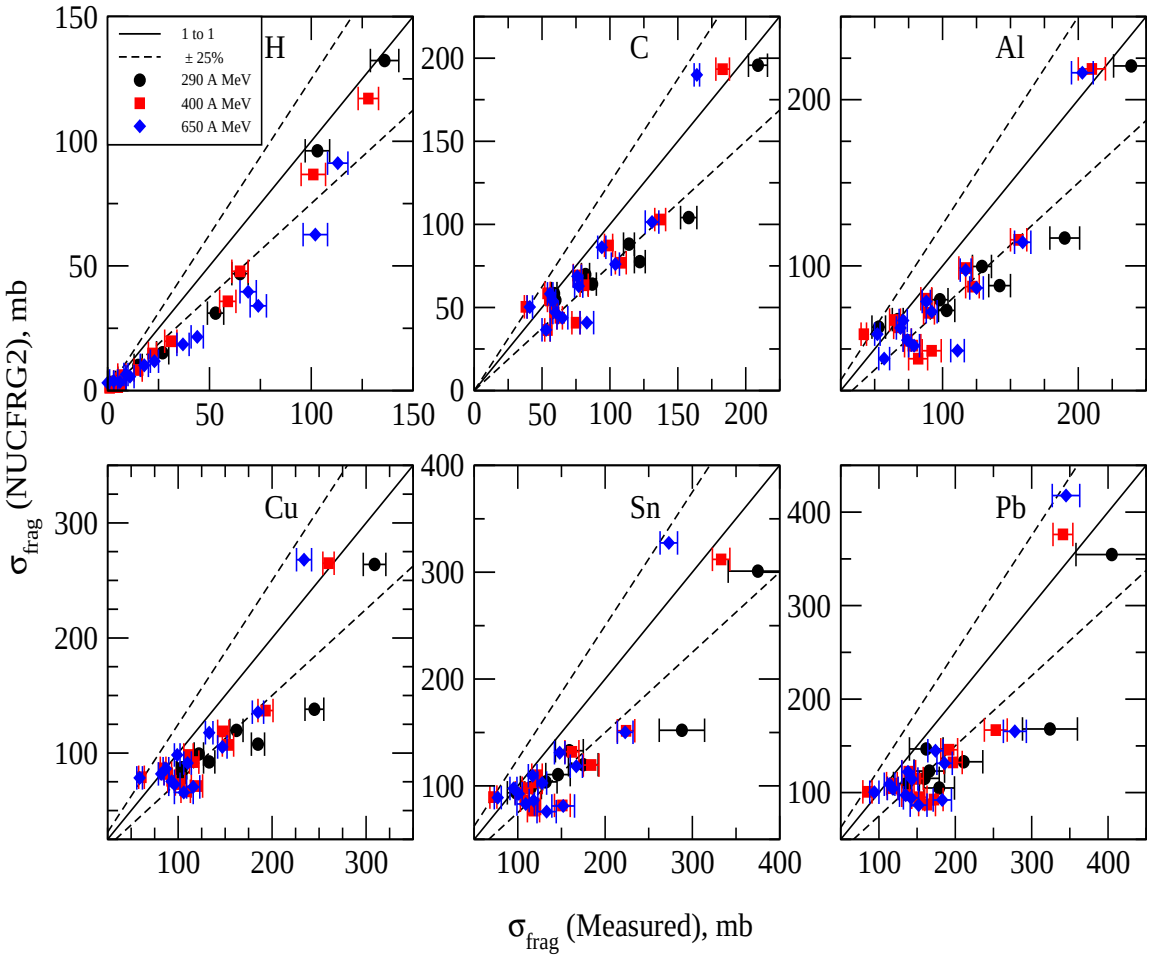

Figure C.54: Comparison of the NUCFRG2 results and the experimental data from Reference [62] for a ^{40}Ar beam incident on the 6 standard targets H, C, Al, Cu, Sn, Pb.

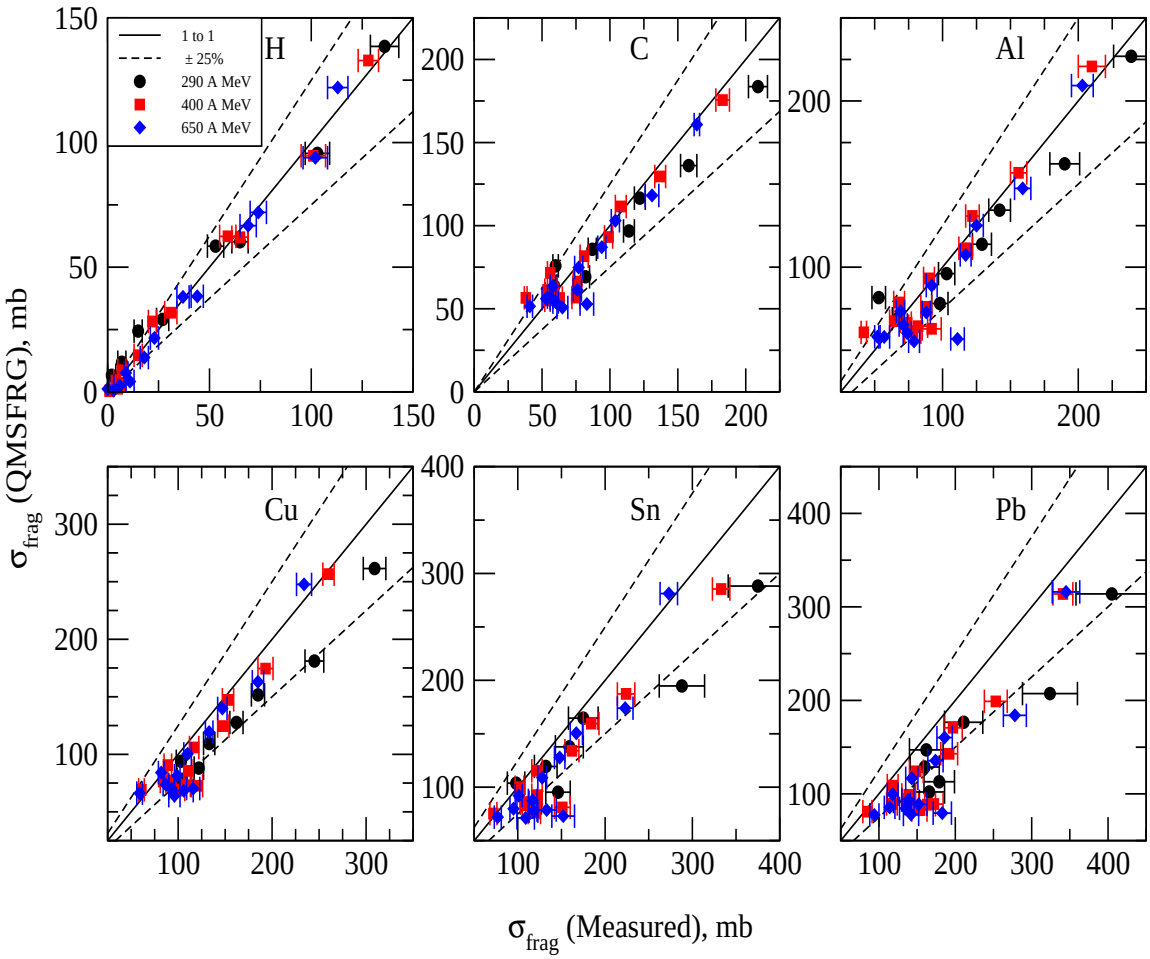

Figure C.55: Comparison of the QMSFRG interpolation results and the experimental data from Reference [62] for a ^{40}Ar beam incident on the 6 standard targets H, C, Al, Cu, Sn, Pb.

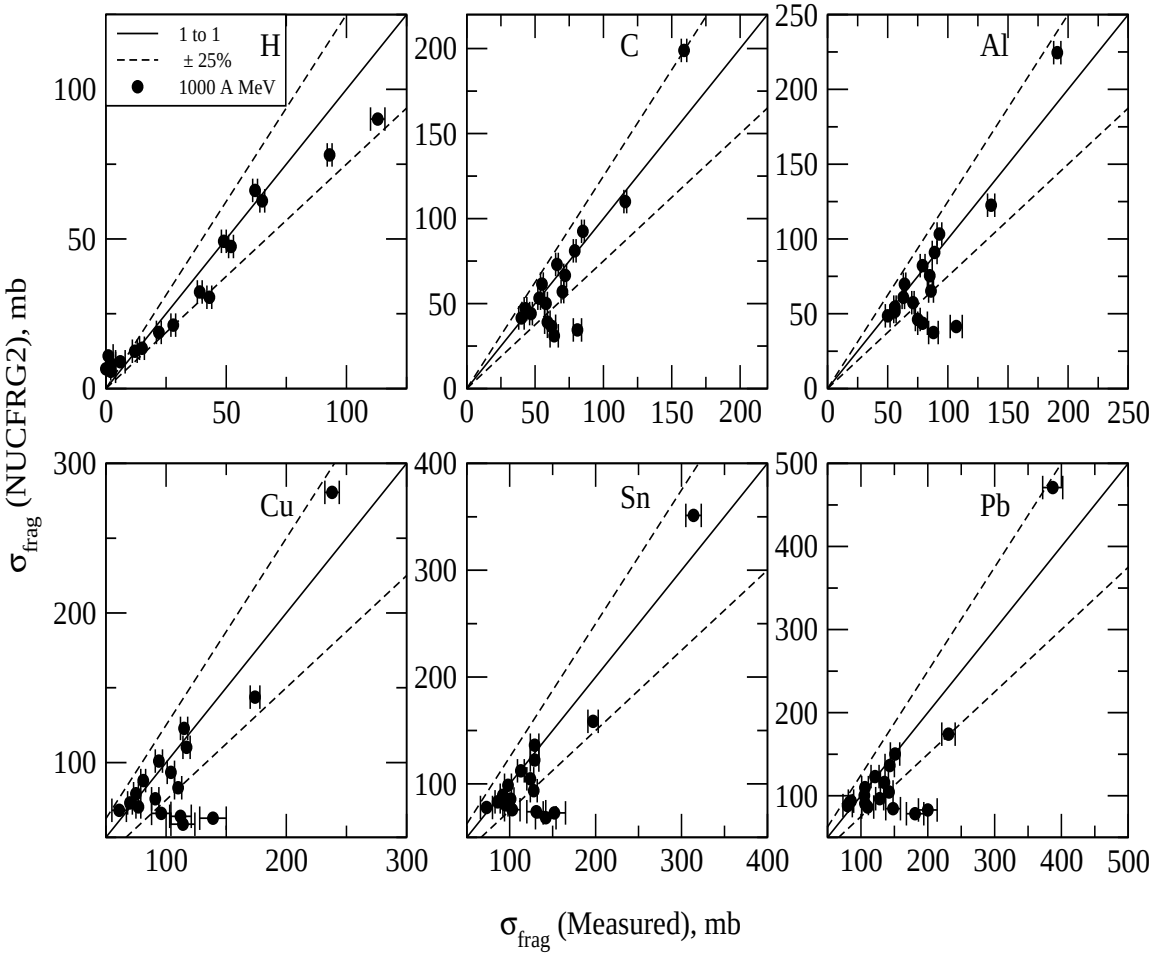

Figure C.56: Comparison of the NUCFRG2 results and the experimental data from Reference [62] for a ^{48}Ti beam incident on the 6 standard targets H, C, Al, Cu, Sn, Pb.

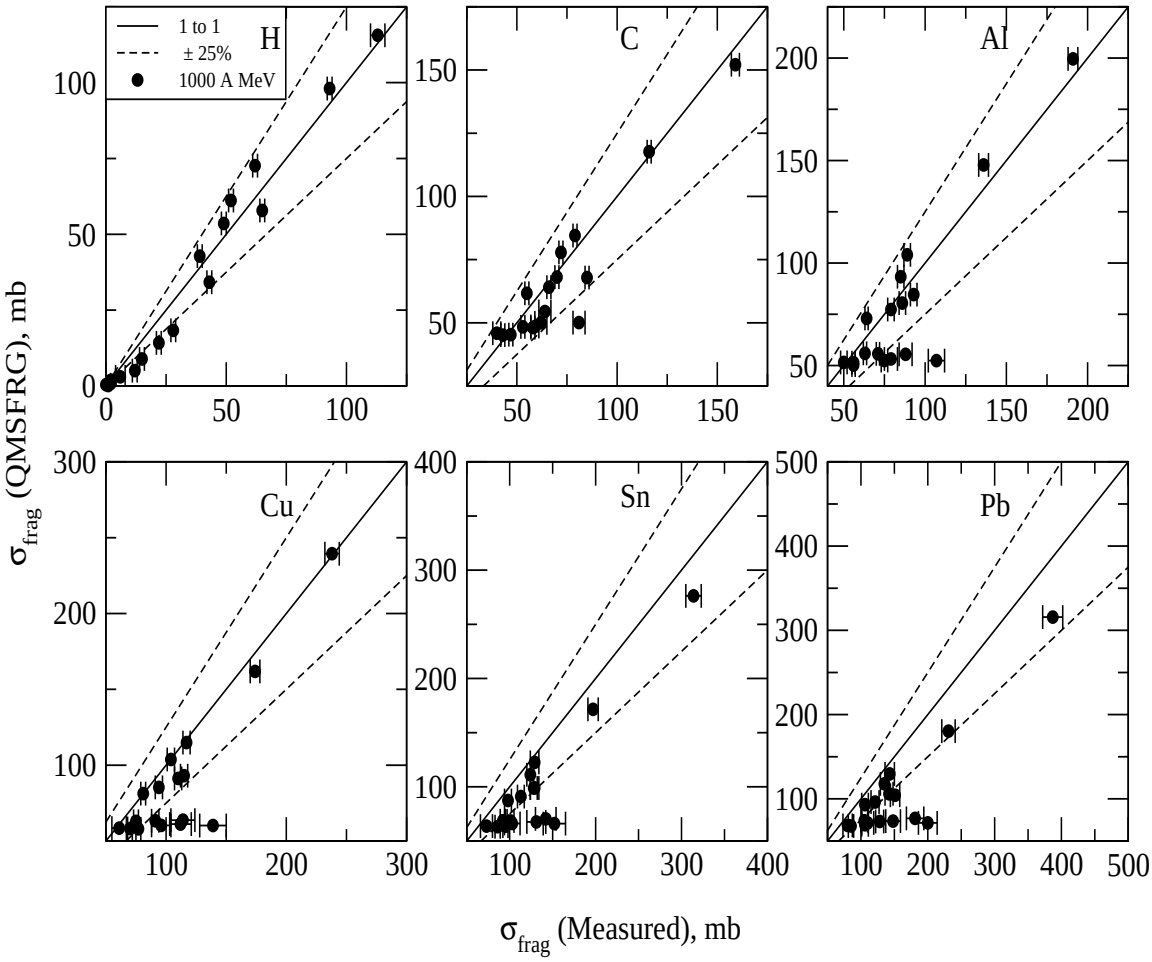

Figure C.57: Comparison of the QMSFRG interpolation results and the experimental data from Reference [62] for a ^{48}Ti beam incident on the 6 standard targets H, C, Al, Cu, Sn, Pb.

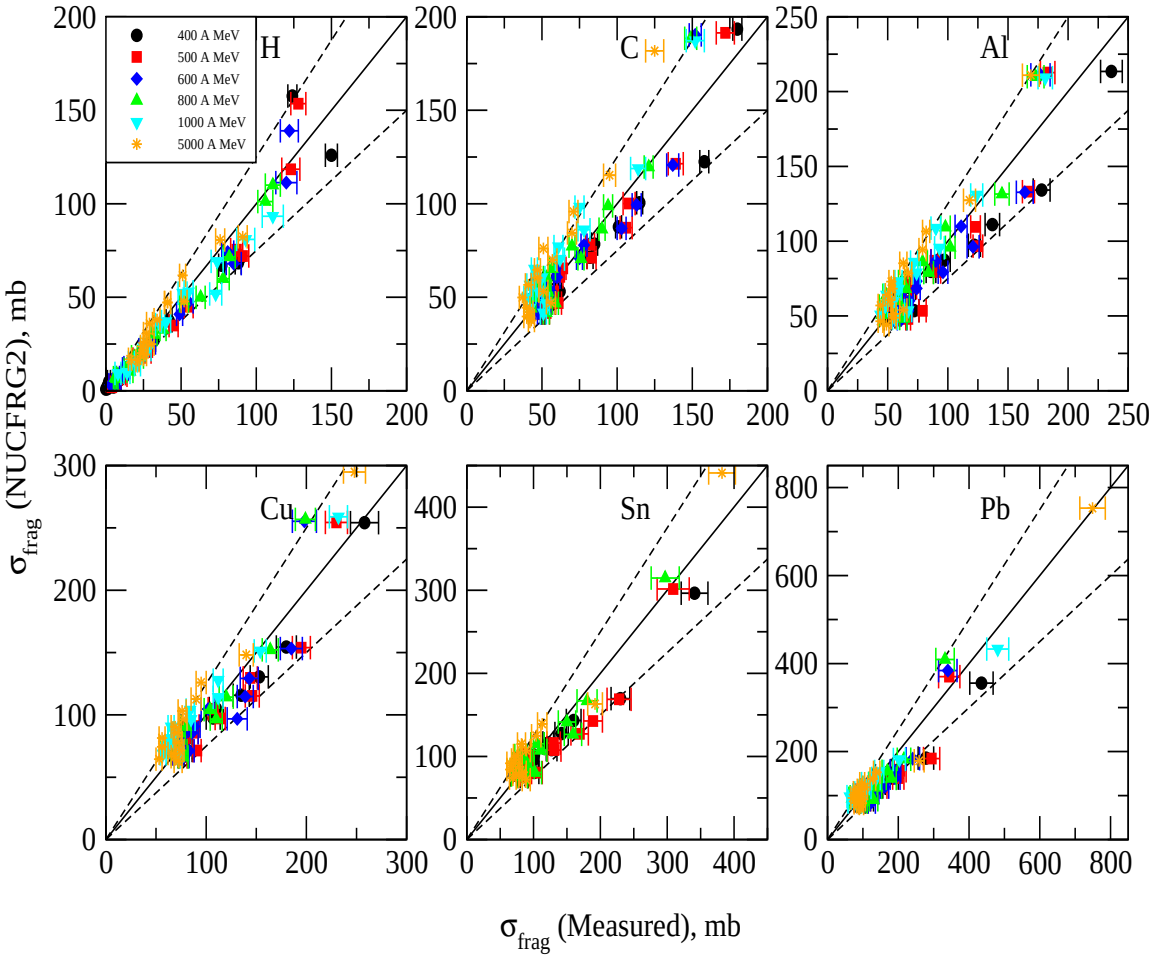

Figure C.58: Comparison of the NUCFRG2 results and the experimental data from References [58] and [62] for a ^{56}Fe beam incident on the 6 standard targets H, C, Al, Cu, Sn, Pb.

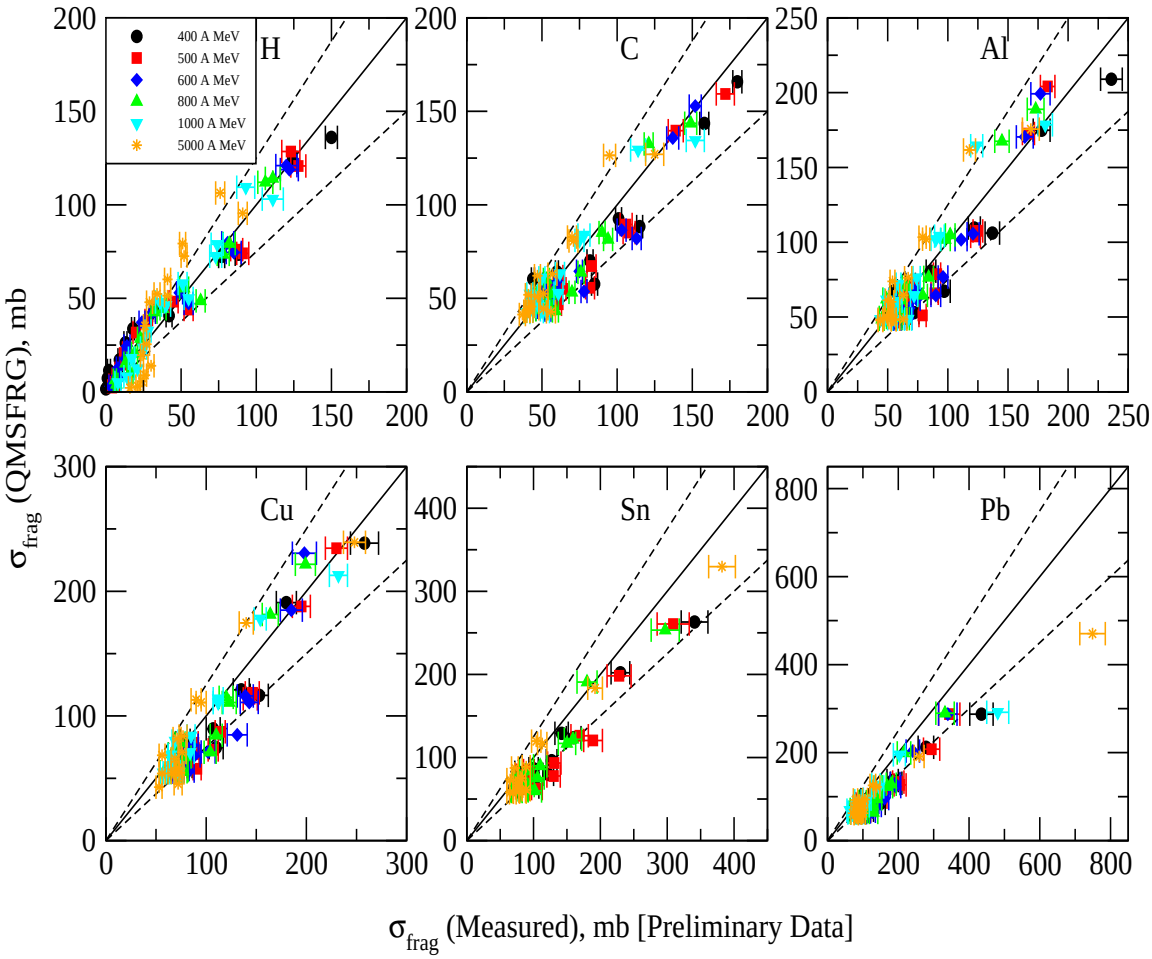

Figure C.59: Comparison of the QMSFRG interpolation results and the experimental data from References [58] and [62] for a ^{56}Fe beam incident on the 6 standard targets H, C, Al, Cu, Sn, Pb.

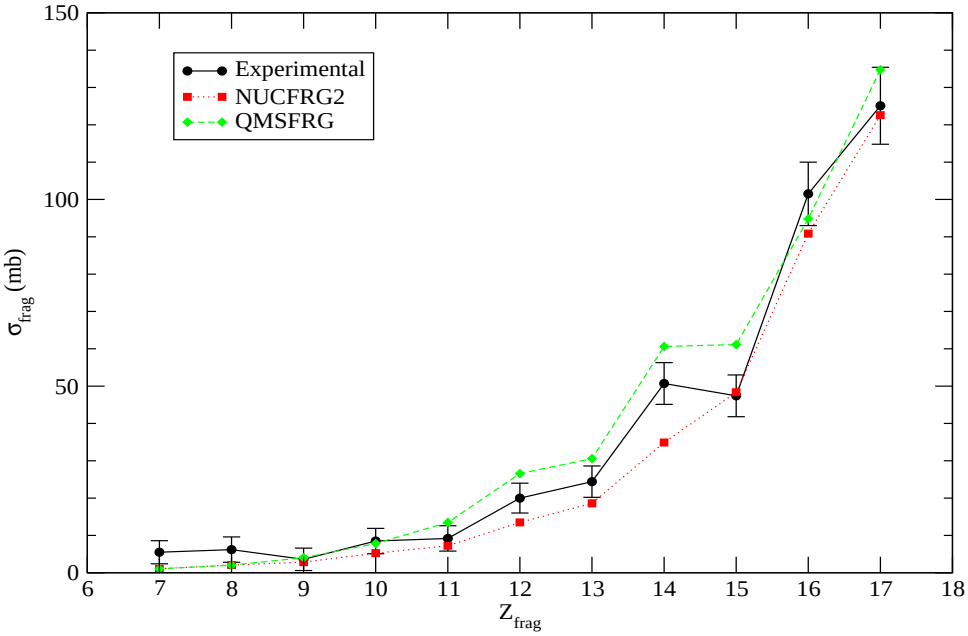

Figure C.60: Comparison of the QMSFRG interpolation and NUCFRG2 model cross section results for the reaction ^{40}Ar $+^{1}$ H $\rightarrow$ Z_{frag} to the experimental data of Iancu *et al.* at a beam energy of 400 A MeV [75].

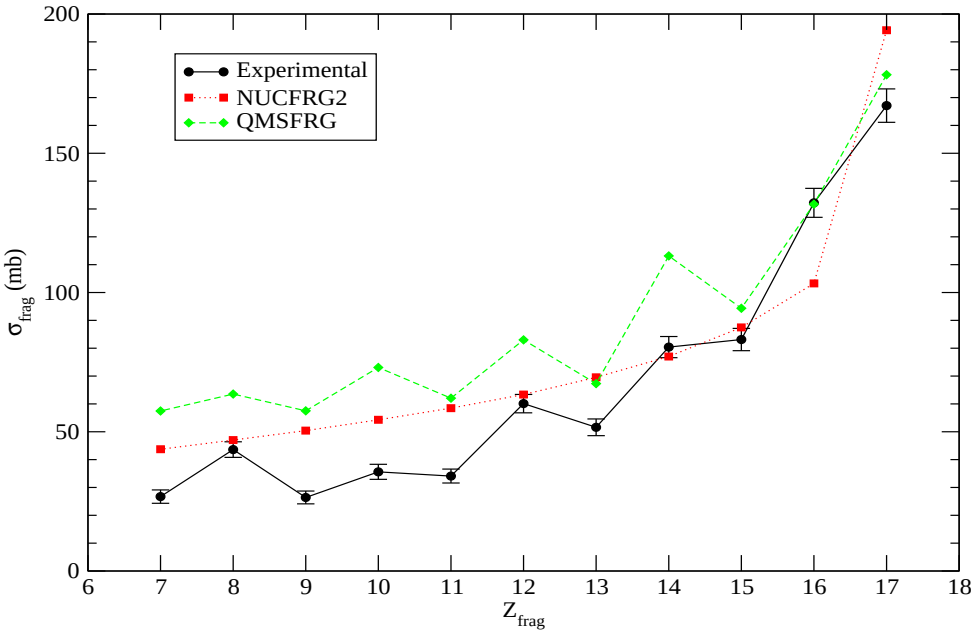

Figure C.61: Comparison of the QMSFRG interpolation and NUCFRG2 model cross section results for the reaction ^{40}Ar $+^{12}$ C $\rightarrow$ Z_{frag} to the experimental data of Iancu *et al.* at a beam energy of 400 A MeV [75].

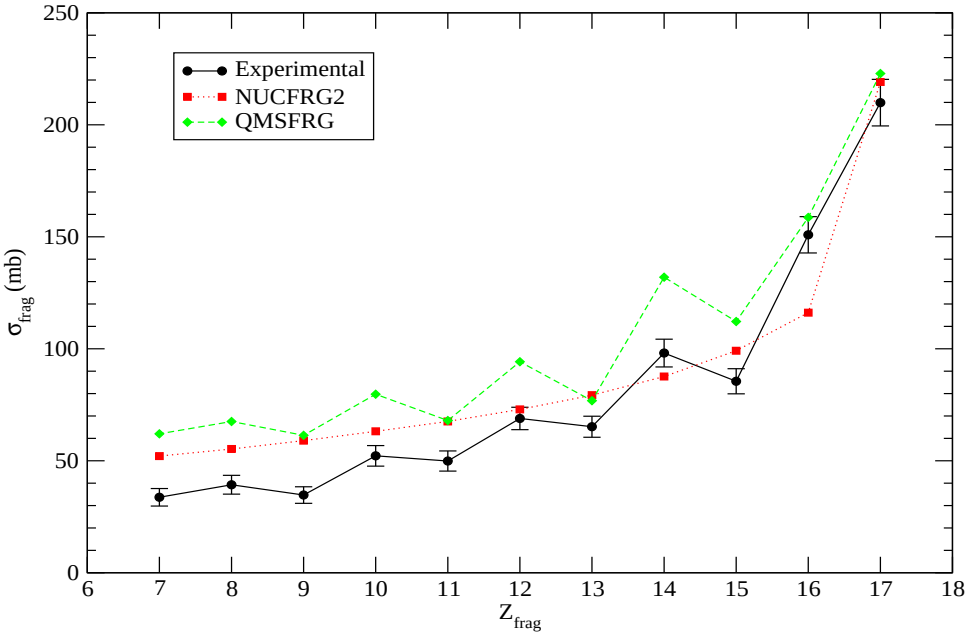

Figure C.62: Comparison of the QMSFRG interpolation and NUCFRG2 model cross section results for the reaction ^{40}Ar $+^{27}$ Al $\rightarrow$ Z_{frag} to the experimental data of Iancu *et al.* at a beam energy of 400 A MeV [75].

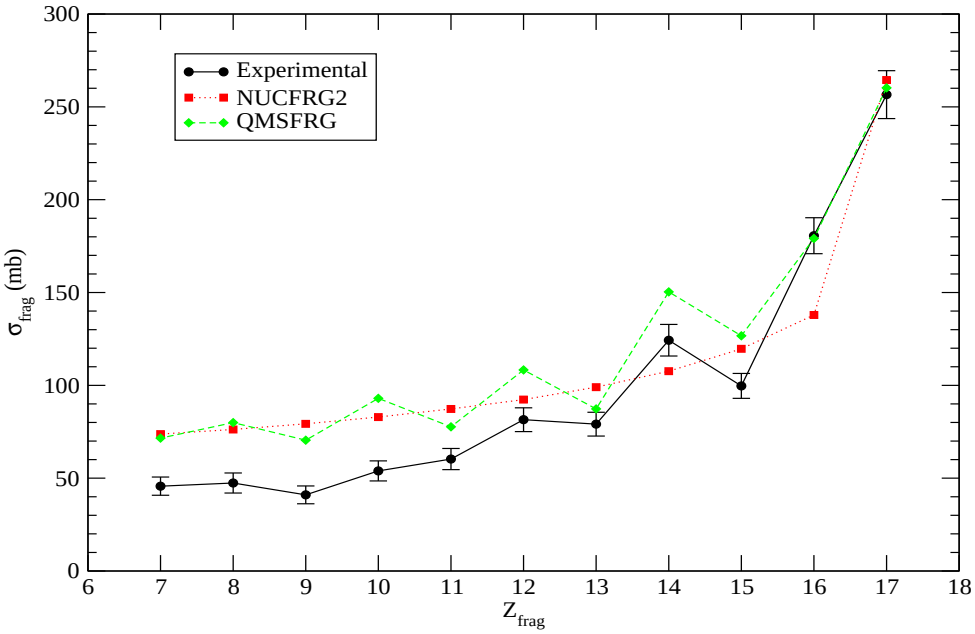

Figure C.63: Comparison of the QMSFRG interpolation and NUCFRG2 model cross section results for the reaction ^{40}Ar $+^{org}$ Cu $\rightarrow$ Z_{frag} to the experimental data of Iancu *et al.* at a beam energy of 400 A MeV [75].

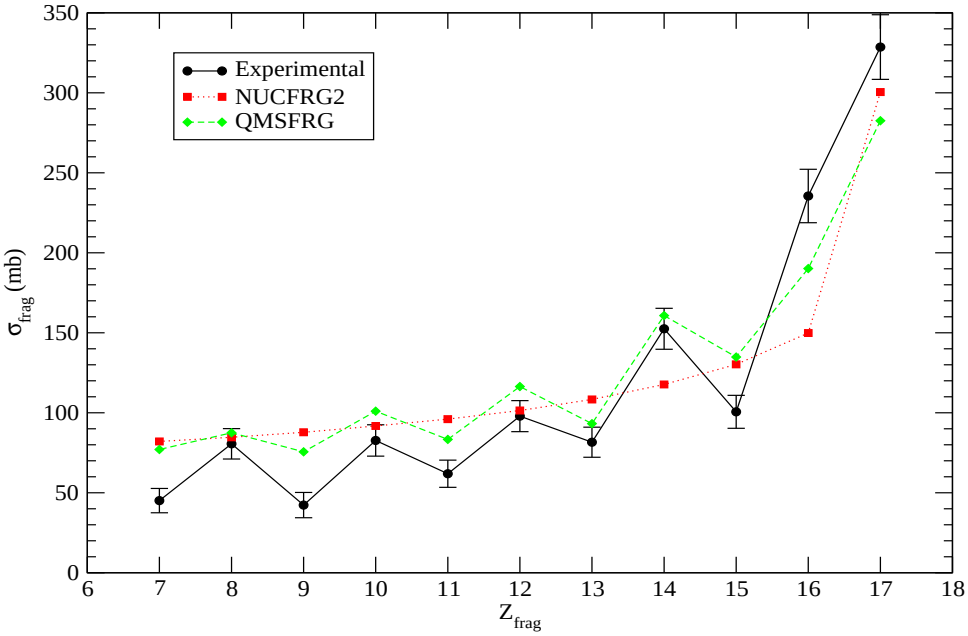

Figure C.64: Comparison of the QMSFRG interpolation and NUCFRG2 model cross section results for the reaction ^{40}Ar $+^{org}$ Ag $\rightarrow$ Z_{frag} to the experimental data of Iancu *et al.* at a beam energy of 400 A MeV [75].

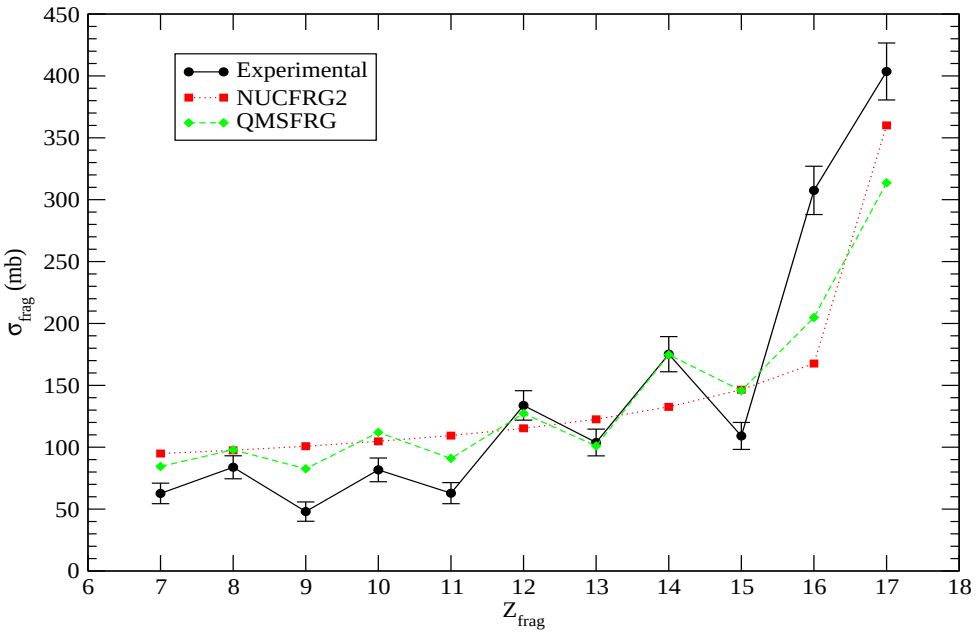

Figure C.65: Comparison of the QMSFRG interpolation and NUCFRG2 model cross section results for the reaction ^{40}Ar $+^{org}$ Pb $\rightarrow$ Z_{frag} to the experimental data of Iancu *et al.* at a beam energy of 400 A MeV [75].

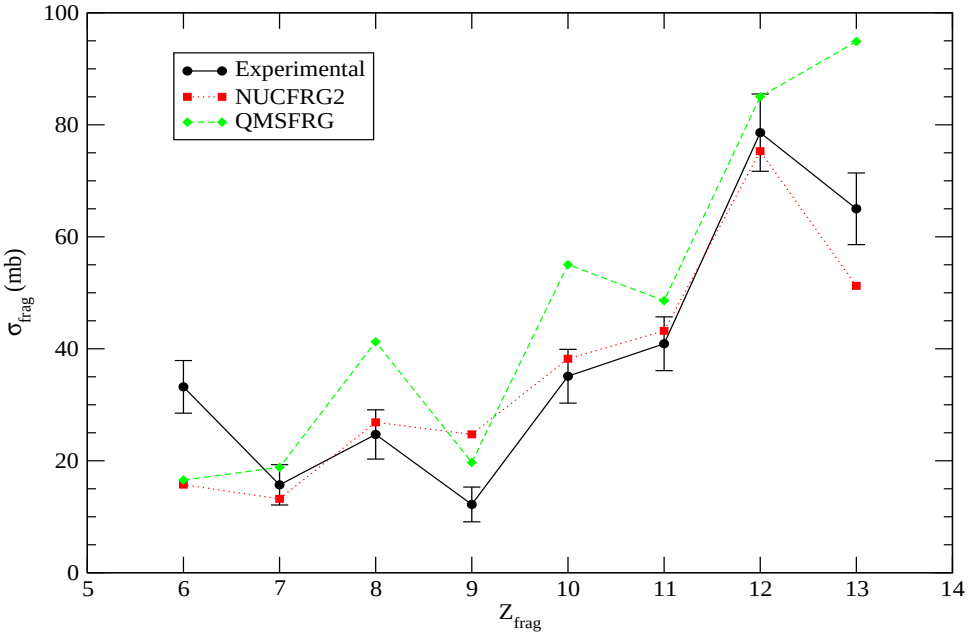

Figure C.66: Comparison of the QMSFRG interpolation and NUCFRG2 model cross section results for the reaction ^{28}Si $+^{1}$ H $\rightarrow$ Z_{frag} to the experimental data of Flesch *et al.* at a beam energy of 490 A MeV [73].

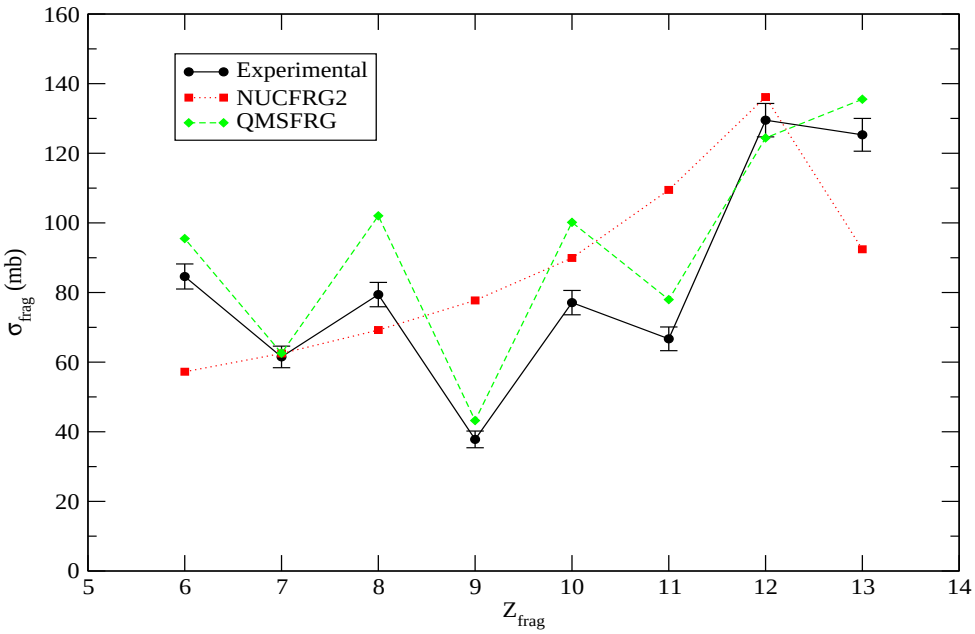

Figure C.67: Comparison of the QMSFRG interpolation and NUCFRG2 model cross section results for the reaction ^{28}Si $+^{12}$ C $\rightarrow$ Z_{frag} to the experimental data of Flesch *et al.* at a beam energy of 490 A MeV [73].

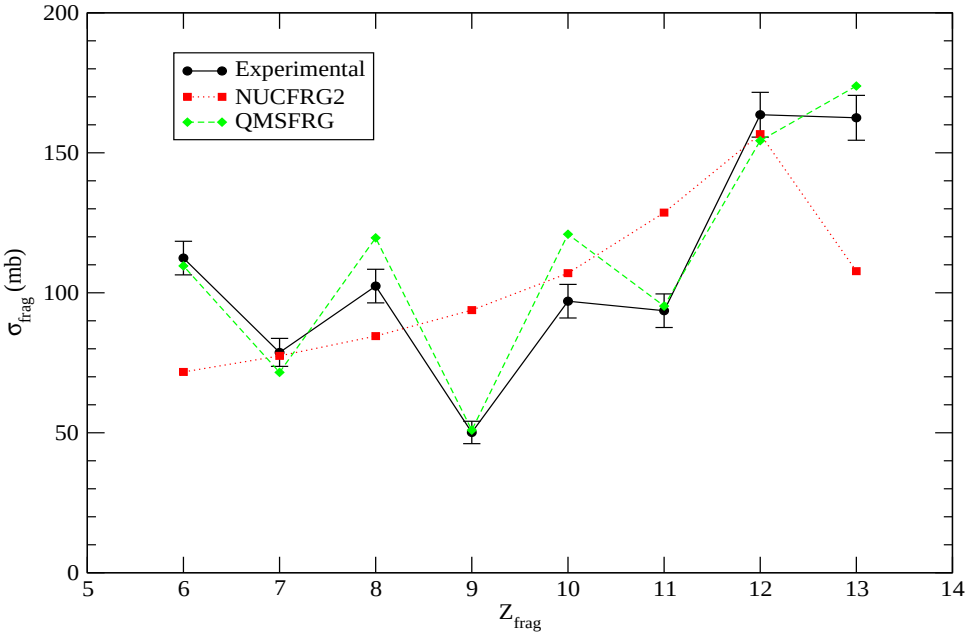

Figure C.68: Comparison of the QMSFRG interpolation and NUCFRG2 model cross section results for the reaction ^{28}Si $+^{27}$ Al $\rightarrow$ Z_{frag} to the experimental data of Flesch *et al.* at a beam energy of 490 A MeV [73].

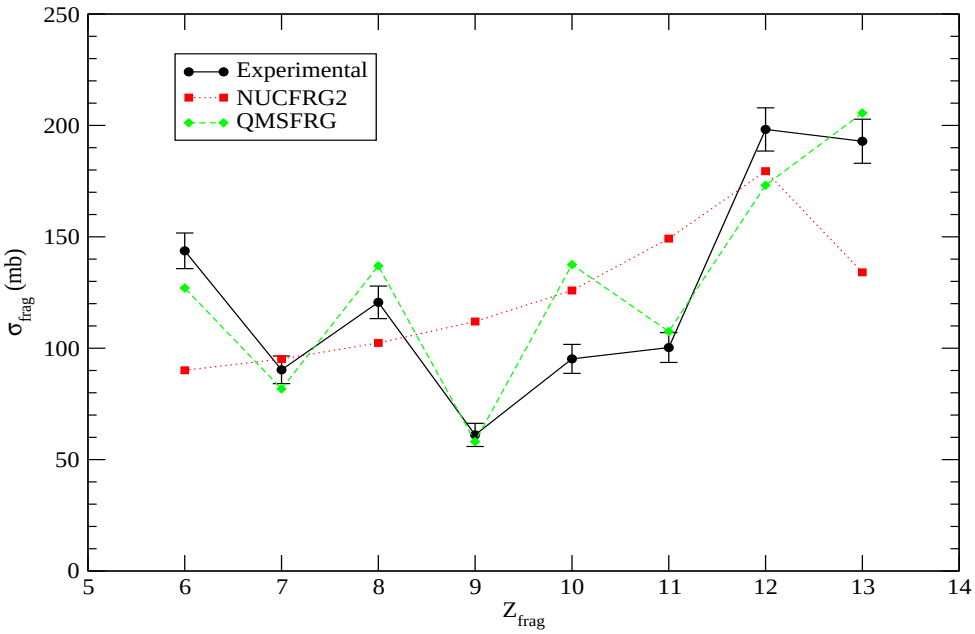

Figure C.69: Comparison of the QMSFRG interpolation and NUCFRG2 model cross section results for the reaction ^{28}Si $+^{org}$ Cu $\rightarrow$ Z_{frag} to the experimental data of Flesch *et al.* at a beam energy of 490 A MeV [73].

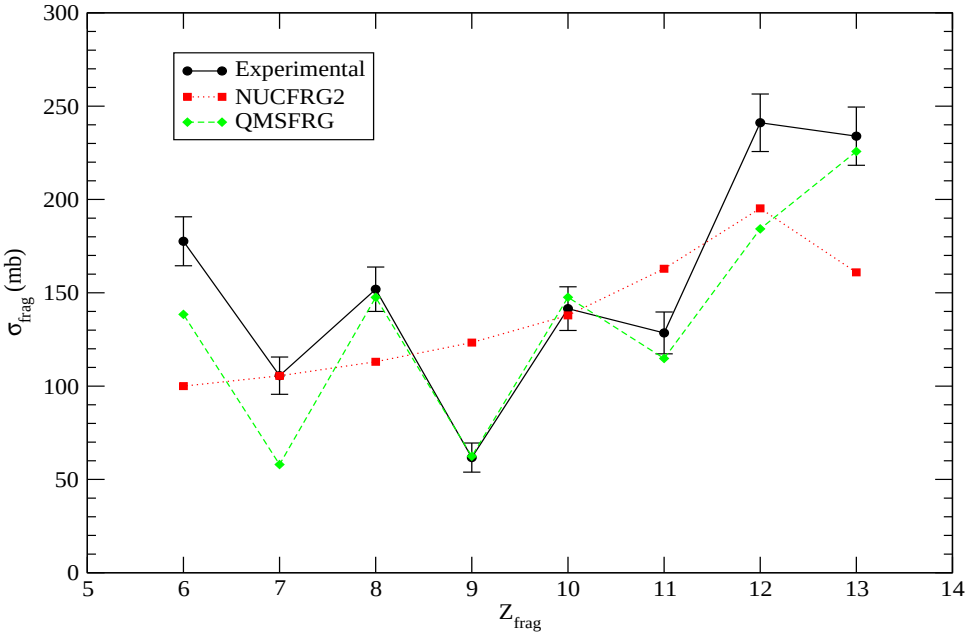

Figure C.70: Comparison of the QMSFRG interpolation and NUCFRG2 model cross section results for the reaction ^{28}Si $+^{org}$ Ag $\rightarrow$ Z_{frag} to the experimental data of Flesch *et al.* at a beam energy of 490 A MeV [73].

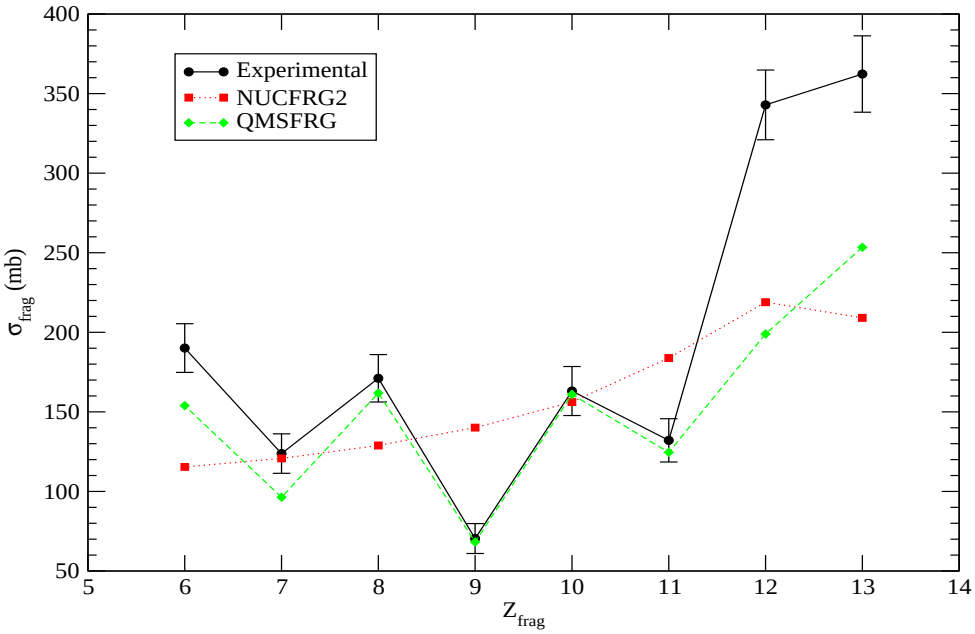

Figure C.71: Comparison of the QMSFRG interpolation and NUCFRG2 model cross section results for the reaction ^{28}Si $+^{org}$ Pb $\rightarrow$ Z_{frag} to the experimental data of Flesch *et al.* at a beam energy of 490 A MeV [73].

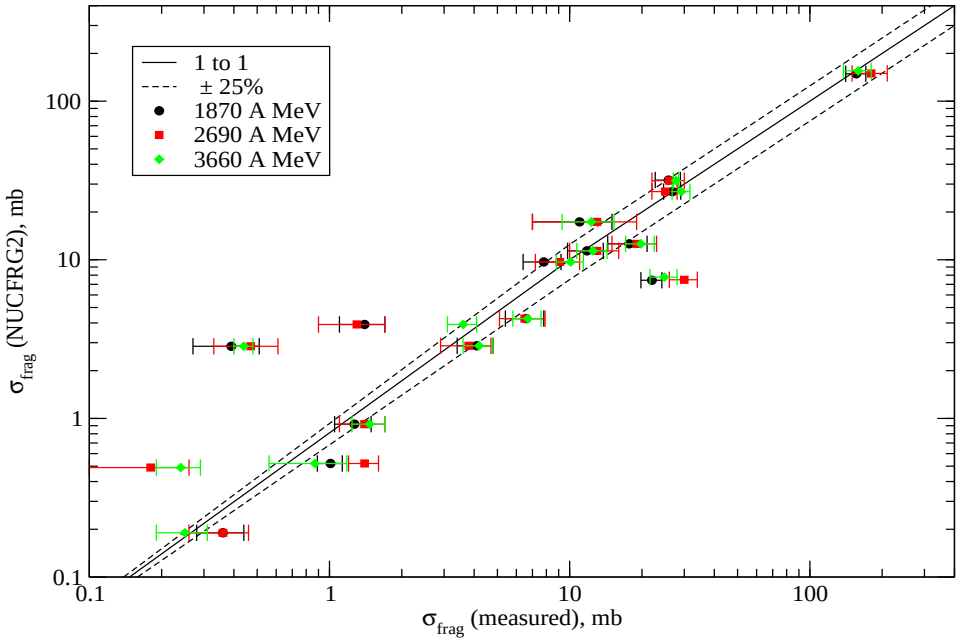

Figure C.72: Comparison of the NUCFRG2 model cross section (σ(Z,A)) results for the reaction ^{12}C + ^{1}H $\rightarrow$ Isotopes to the experimental data of Korejwo *et al.* [78, 79].

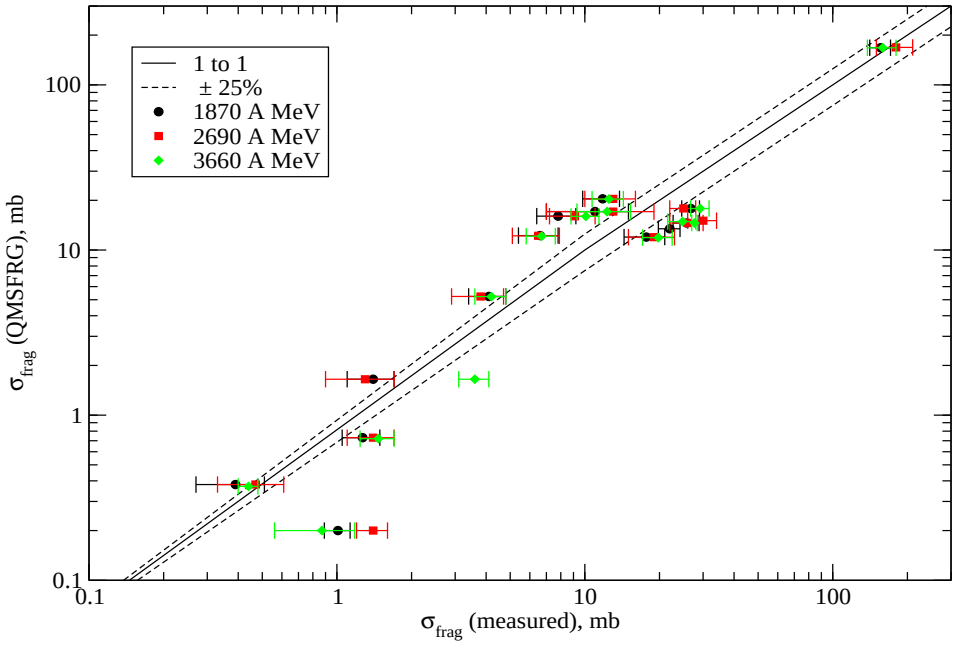

Figure C.73: Comparison of the QMSFRG interpolation cross section (σ(Z,A)) results for the reaction ^{12}C + ^{1}H $\rightarrow$ Isotopes to the experimental data of Korejwo *et al.* [78, 79].

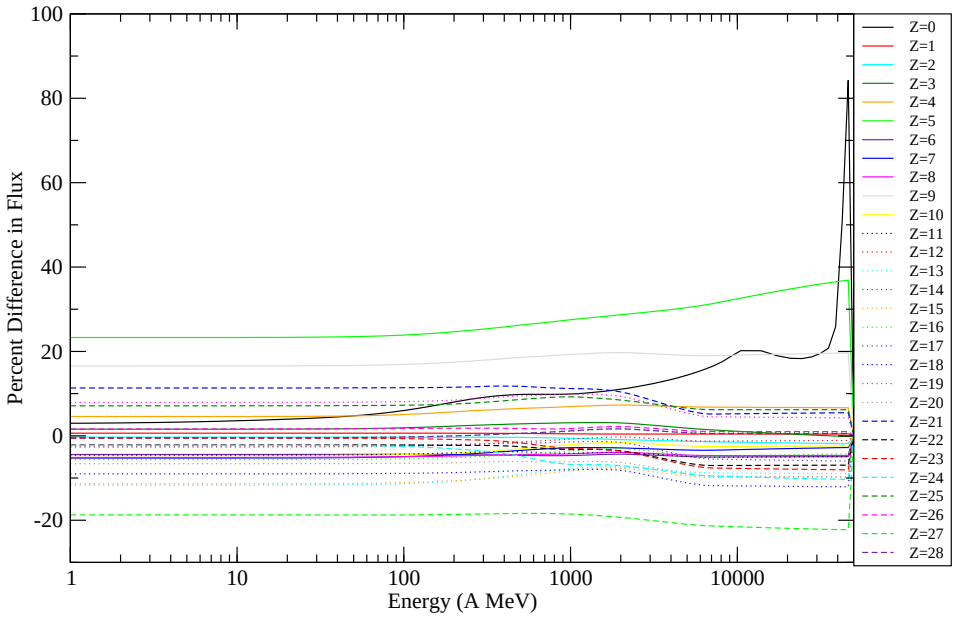

Figure C.74: Comparison of the HZETRN results for percent flux difference vs energy in polyethylene at a depth of 10 g/cm^2 with the 1977 solar minimum GCR model using the QMSFRG interpolation and NUCFRG2 model cross section databases.

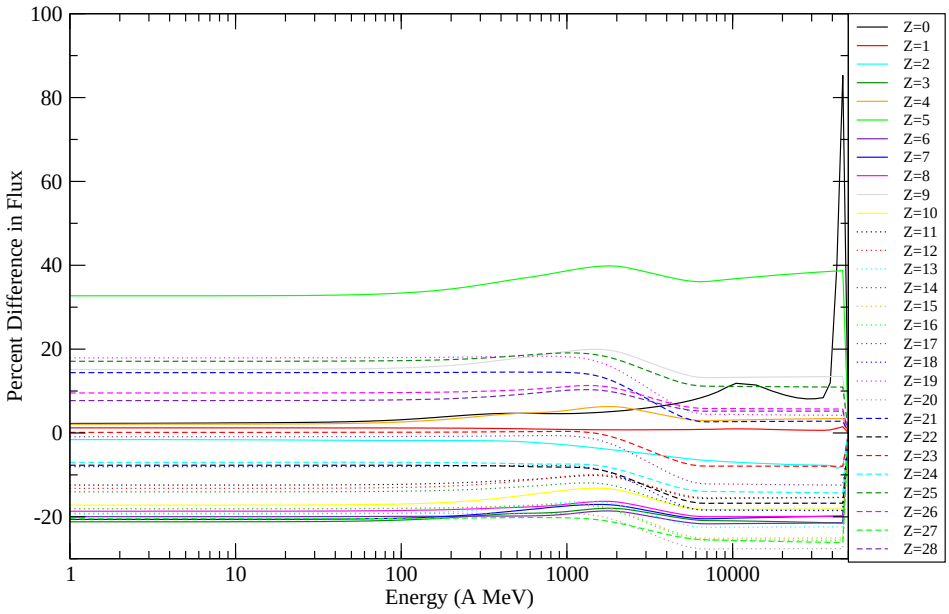

Figure C.75: Comparison of the HZETRN results for percent flux difference vs energy in polyethylene at a depth of 50 g/cm^2 with the 1977 solar minimum GCR model using the QMSFRG interpolation and NUCFRG2 model cross section databases.

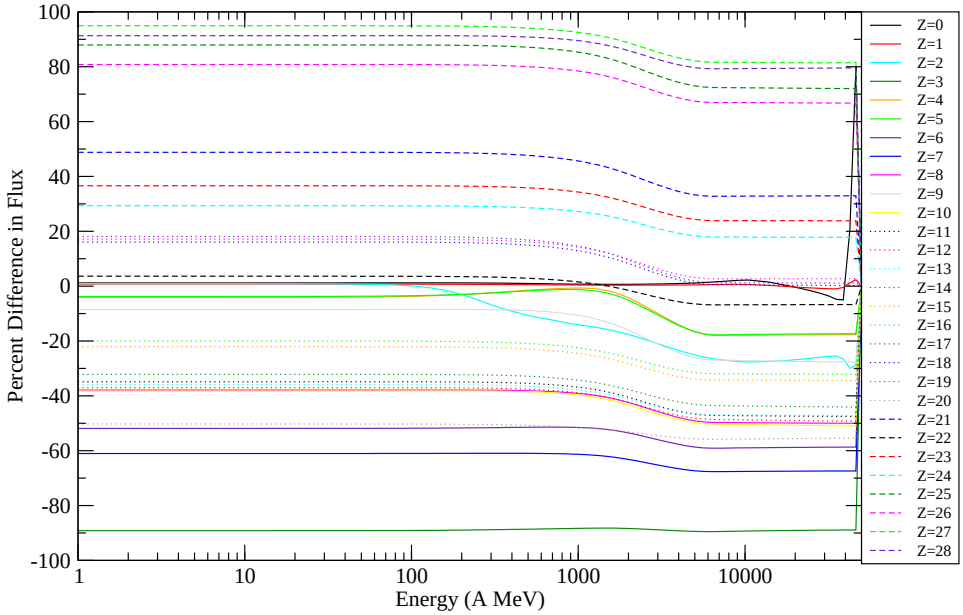

Figure C.76: Comparison of the HZETRN results for percent flux difference vs energy in polyethylene at a depth of 300 g/cm^2 with the 1977 solar minimum GCR model using the QMSFRG interpolation and NUCFRG2 model cross section databases.

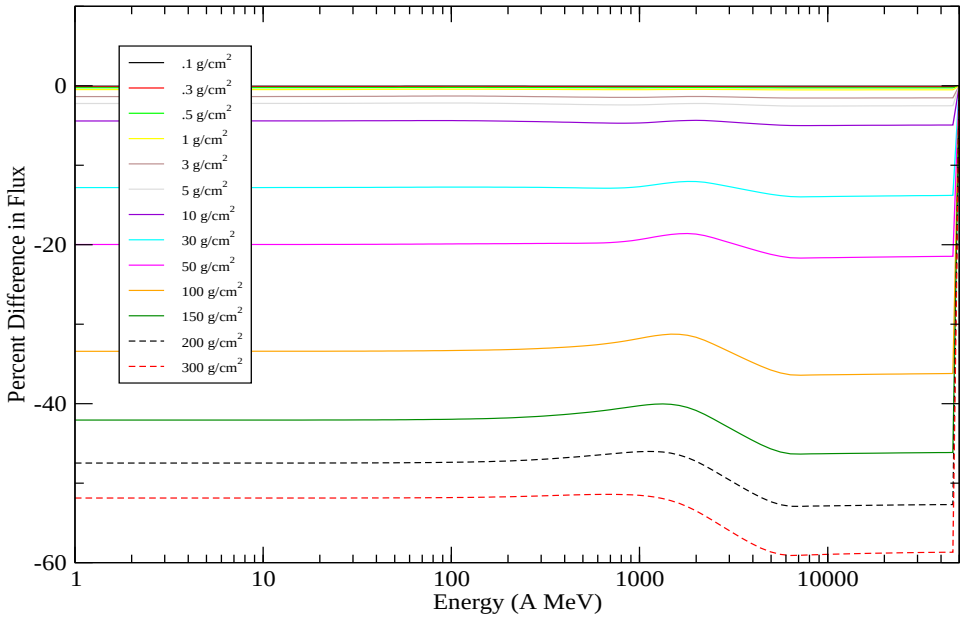

Figure C.77: Comparison of the HZETRN results of carbon isotopes for percent flux difference vs energy at 13 different depths in polyethylene with the 1977 solar minimum GCR model using the QMSFRG interpolation and NUCFRG2 model cross section databases.

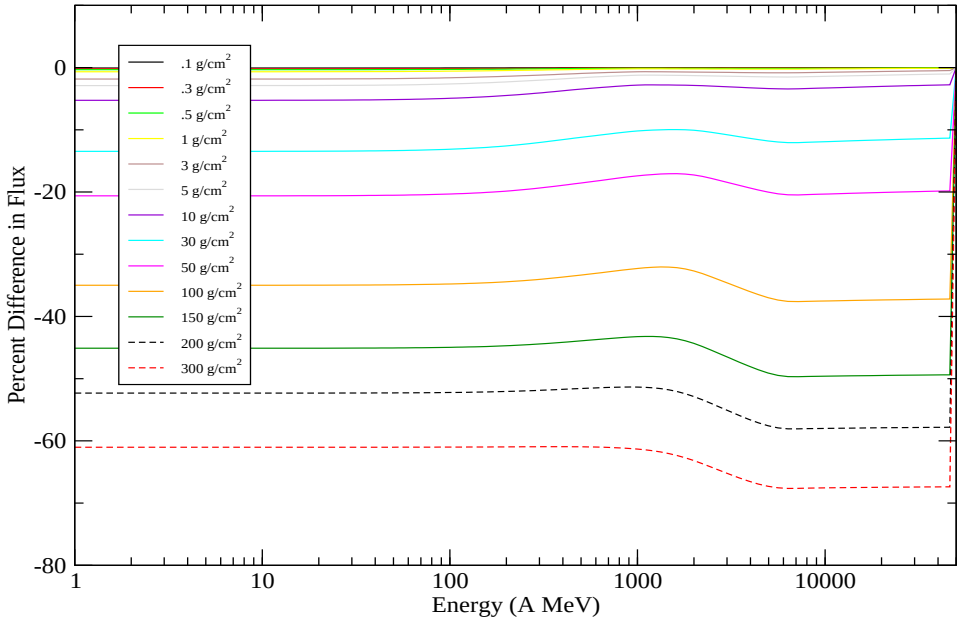

Figure C.78: Comparison of the HZETRN results of nitrogen isotopes for percent flux difference vs energy at 13 different depths in polyethylene with the 1977 solar minimum GCR model using the QMSFRG interpolation and NUCFRG2 model cross section databases.

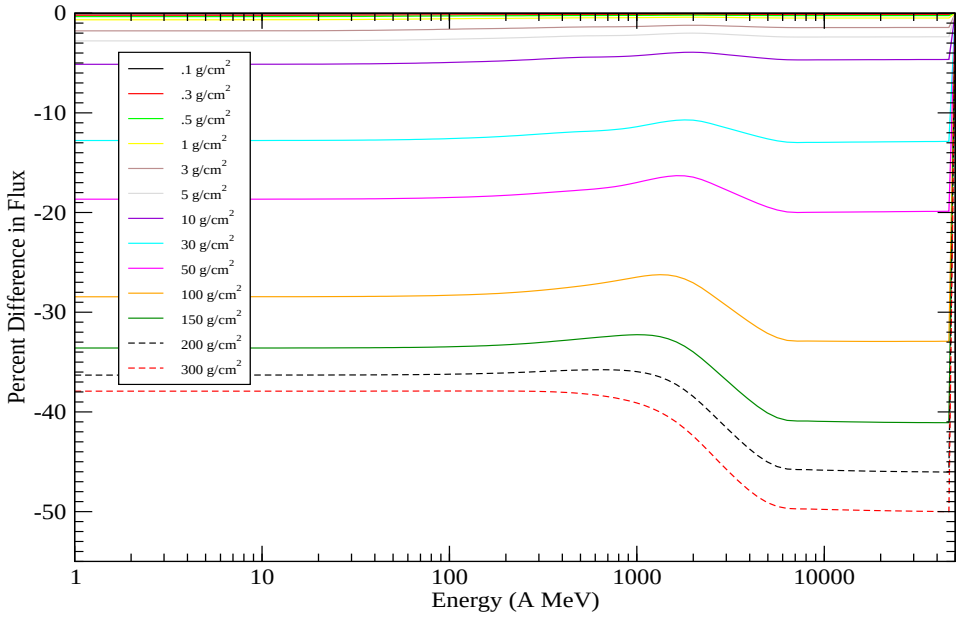

Figure C.79: Comparison of the HZETRN results of oxygen isotopes for percent flux difference vs energy at 13 different depths in polyethylene with the 1977 solar minimum GCR model using the QMSFRG interpolation and NUCFRG2 model cross section databases.

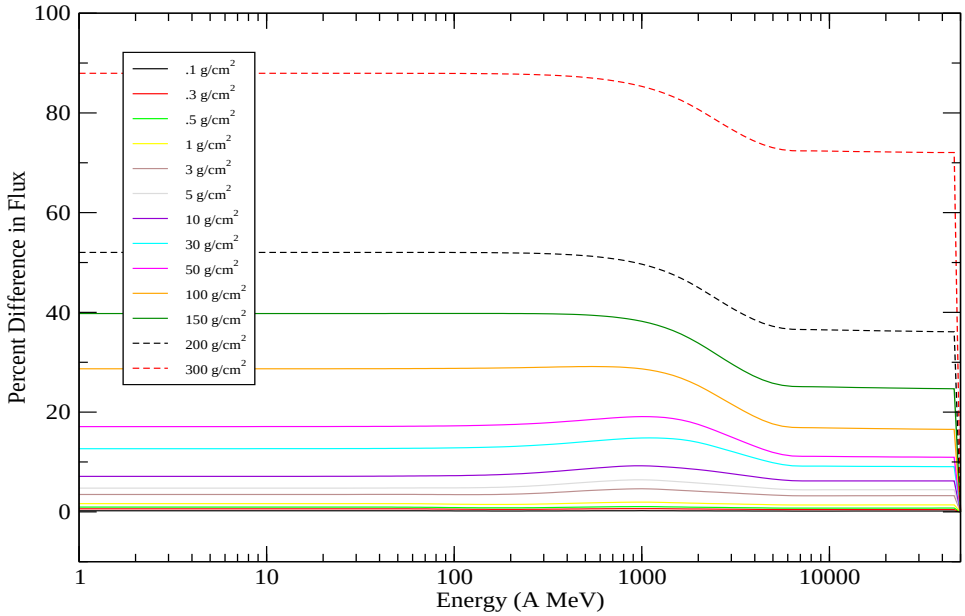

Figure C.80: Comparison of the HZETRN results of iron isotopes for percent flux difference vs energy at 13 different depths in polyethylene with the 1977 solar minimum GCR model using the QMSFRG interpolation and NUCFRG2 model cross section databases.

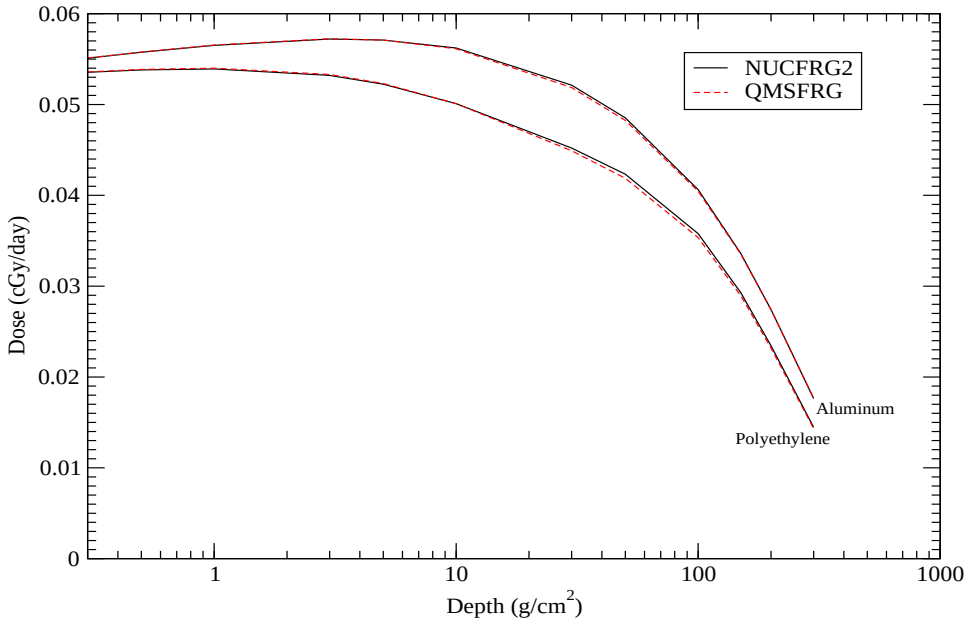

Figure C.81: Comparison of the HZETRN results for dose vs depth in aluminum and polyethylene with the 1977 solar minimum GCR model using the QMSFRG interpolation and NUCFRG2 model cross section databases.

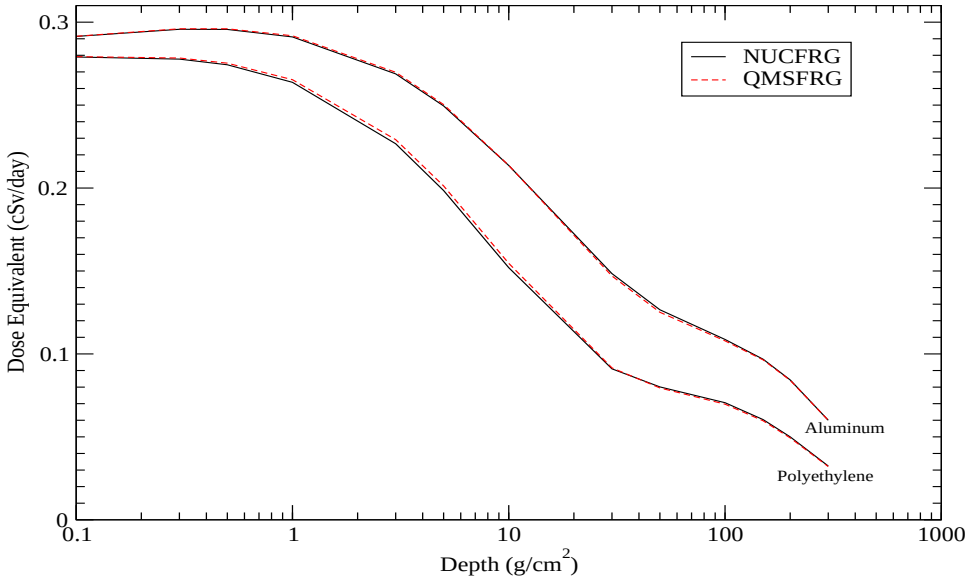

Figure C.82: Comparison of the HZETRN results for dose equivalent vs depth in aluminum and polyethylene with the 1977 solar minimum GCR model using the QMSFRG interpolation and NUCFRG2 model cross section databases.

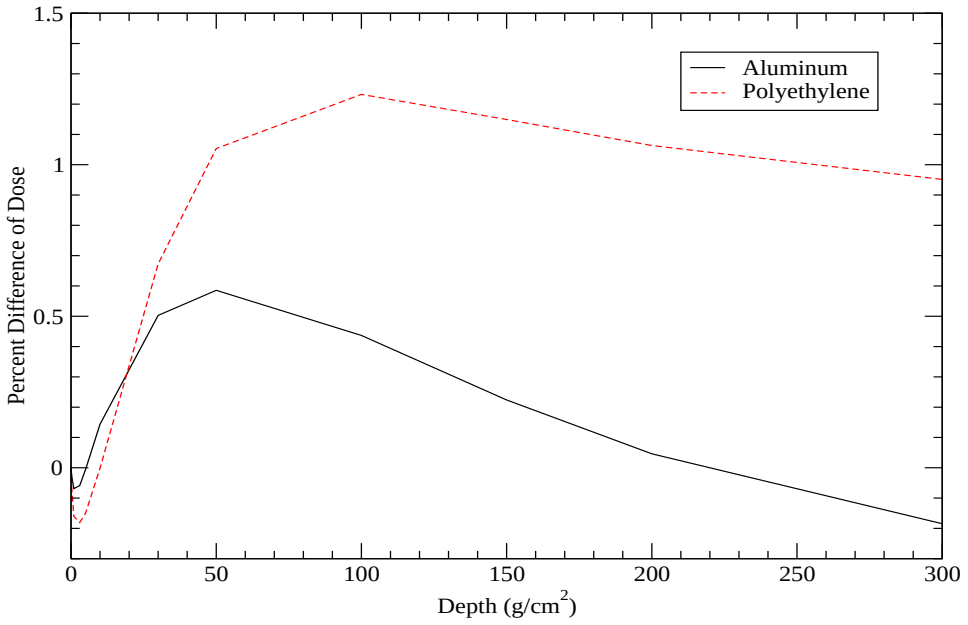

Figure C.83: Comparison of the HZETRN results for dose difference vs depth in aluminum and polyethylene with the 1977 solar minimum GCR model using the QMSFRG and NUCFRG2 model cross section databases. Dose difference is simply the HZETRN results for dose using NUCFRG2 minus the HZETRN results for dose using QMSFRG.

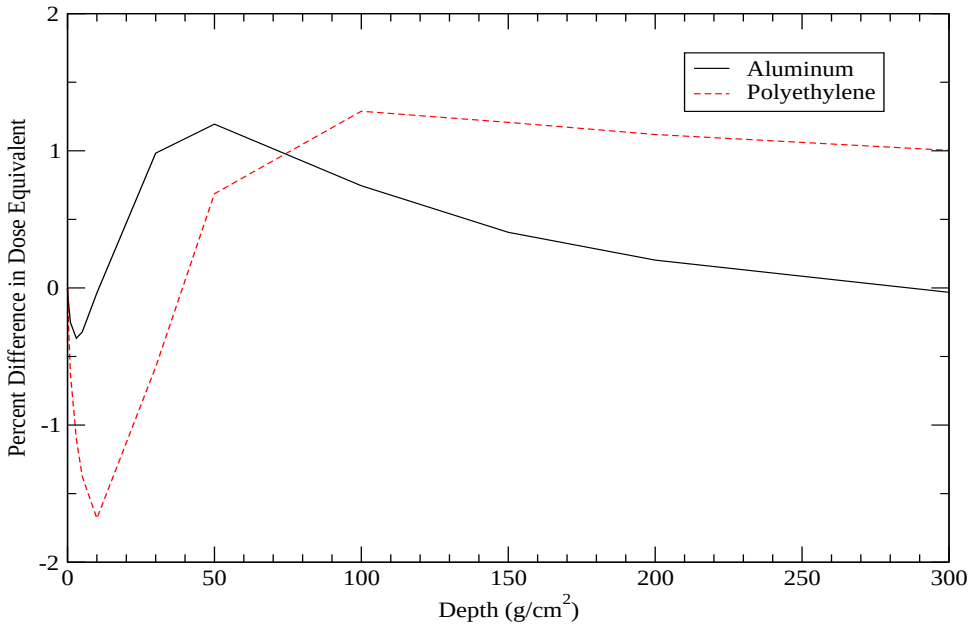

Figure C.84: Comparison of the HZETRN results for dose equivalent difference vs depth in aluminum and polyethylene with the 1977 solar minimum GCR model using the QMSFRG and NUCFRG2 model cross section databases. Dose difference is simply the HZETRN results for dose equivalent using NUCFRG2 minus the HZETRN results for dose equivalent using QMSFRG.

Bibliography

[1] Wilson, J. W. *et al.* HZETRN: Description of a free-space ion and nucleon transport and shielding computer program. Tech. Rep. TP-3495, NASA (1995).

[2] Huber, S. & Aichelin, J. Production of Δ and N^* resonances in the one boson exchange model. *Nucl. Phys. A* **573**, 587 (1994).

[3] Dmitriev, V. *et al.* Δ-Formation In The ^{1}H (^{3}He, ^{3}H) Δ^{++} Reaction At Intermediate-Energies. *Nucl. Phys. A* **459**, 503 (1986).

[4] Blattnig, S. R. *et al.* MESTRN: A Deterministic Meson-Muon Transport Code for Space Radiation. Tech. Rep. TM-212995, NASA (2004).

[5] Wilson, J. W. *et al.* Transport Methods and Interactions for Space Radiations. Tech. Rep. RP-1267, NASA (1991).

[6] Committee on Solar and Space Physics and Committee on Solar-Terrestrial Research. Radiation and the International Space Station: Recommendations to Reduce Risk. Tech. Rep., National Research Council (2000).

[7] Ad Hoc Committee on the Solar System Radiation Environment and NASAs Vision for Space Exploration: A Workshop. Space Radiation Hazards and the Vision for Space Exploration: Report of a Workshop. Tech. Rep., National Research Council (2006).

[8] Wilson, J. W. *et al.* Natural and Induced Enviroment in Low Earth Orbit. Tech. Rep. TM-2002-211668, NASA (2002).

[9] Simpson, J. A. Elemental and isotopic composition of the galactic cosmic rays. *Ann. Rev. Nucl. Part. Sci.* **33**, 323–382 (1983).

[10] Durante, M. Radiation protection in space. *Riv. Nuovo Cimento* **25**, 1–70 (2002).

[11] Jain, B. K. & Santra, A. B. Delta excitation in proton proton and proton nucleus collisions. *Phys. Rep. 230* **1** (1993).

[12] Blattnig, S. R. *et al.* Parametrizations of inclusive cross sections for pion production in proton–proton collisions. *Phys. Rev. D* **63**, 094030 (2000).

[13] Griffiths, D. *Introduction to Elementary Particles* (Wiley, New York, 1987).

[14] Kraus, P. & Griffiths, D. J. Renormalization of a model quantum field theory. *Am. J. Phys.* **60**, 1013 (1992).

[15] Machleidt, R. The Meson Theory Of Nuclear Forces And Nuclear Structure. *Adv. Nucl. Phys.* **19**, 189 (1989).

[16] Peskin, M. E. & V., S. D. *An Introduction to Quantum Field Theory* (Perseus Books, Reading, Massachusetts, 1995).

[17] Froissart, M. Asymptotic behavior and subtractions in the mandelstam representation. *Phys. Rev.* **123**, 1053–1057 (1961).

[18] Bertsch, G. F. & Das Gupta, S. A Guide to microscopic models for intermediate-energy heavy ion collisions. *Phys. Rept.* **160**, 189–233 (1988).

[19] Yao, W.-M. *et al.* The Review of Particle Physics. *J. Phys. G* **33**, 1 (2006).

[20] Albrow, M. G. *et al.* Polarization in elastic proton proton scattering between 0.86 and 2.74 GeV/c. *Nucl. Phys.* **B23**, 445–465 (1970). The data were taken from the HEPDATA Reaction Database found at http://durpdg.dur.ac.uk/hepdata/reac.html.

[21] Dobrovolsky, A. V. *et al.* Experimental data on elastic pp, np, pd and pγ forward scattering at intermediate-energies. Tech. Rep. LENINGRAD-88-1454, Lenigrad Nuclear Physics Institute (1988). The data were taken from the HEPDATA Reaction Database found at http://durpdg.dur.ac.uk/hepdata/reac.html.

[22] Jenkins, K. A. *et al.* Measurement of wide-angle elastic scattering of pions and protons off protons. *Phys. Rev. D* **21**, 2445–2496 (1980). The data were taken from the HEPDATA Reaction Database found at http://durpdg.dur.ac.uk/hepdata/reac.html.

[23] Ambats, I. *et al.* Systematic study of $\pi^{\pm}p$, $k^{\pm}p$, pp, and $p\bar{p}$ forward elastic scattering from 3 to 6 $\frac{GeV}{c}$. *Phys. Rev. D* **9**, 1179–1209 (1974). The data were taken from the HEPDATA Reaction Database found at http://durpdg.dur.ac.uk/hepdata/reac.html.

[24] Baglin, C. *et al.* Elastic Scattering of 10-GeV/c pi+ and K+ Mesons and of 9- GeV/c Protons on Protons. *Nucl. Phys.* **B98**, 365 (1975). The data were taken from the HEPDATA Reaction Database found at http://durpdg.dur.ac.uk/hepdata/reac.html.

[25] Brandenburg, G. W. *et al.* Measurement of Particle and anti-Particle Elastic Scattering on Protons Between 6-GeV and 14-GeV. *Phys. Lett.* **B58**, 367 (1975). The data were taken from the HEPDATA Reaction Database found at http://durpdg.dur.ac.uk/hepdata/reac.html.

[26] Beznogikh, G. G. *et al.* Differential cross-sections of elastic p p scattering in the energy range 8-70 GeV. *Nucl. Phys.* **B54**, 78–96 (1973). The data were taken from the HEPDATA Reaction Database found at http://durpdg.dur.ac.uk/hepdata/reac.html.

[27] Edelstein, R. M. *et al.* Isobar production and elastic scattering in p p interaction from 6 GeV/c to 30 GeV/c. *Phys. Rev. D* **5**, 1073–1096 (1972). The data were taken from the HEPDATA Reaction Database found at http://durpdg.dur.ac.uk/hepdata/reac.html.

[28] Teis, S. *et al.* Probing nuclear expansion dynamics with π^-/π^+ spectra. *Z. Phys.* **A356**, 421 (1997).

[29] Larionov, A. & Mosel, U. The $NN \to N\Delta$ cross section in nuclear matter. *Nucl. Phys. A* **728**, 135 (2003).

[30] Larionov, A. *et al.* Resonance lifetime in Boltzmann-Uehling-Uhlenbeck theory: Observable consequences. *Phys. Rev. C* **66**, 054604 (2002).

[31] Mao, G. *et al.* Relativistic transport theory of N, Δ, and $N^*(1440)$ interacting through σ, ω, and π mesons. *Phys, Rev. C* **57**, 1938 (1998).

[32] Rekalo, M. & Tomasi-Gustafsson, E. The reaction $\Delta + N \to N + N + \phi$ in ion-ion collisions. *Phys. Rev. C* **67**, 044004 (2003).

[33] Mandelstam, S. A resonance model for pion production in nucleon-nucleon collisions as fairly low energies. *Proc. Roy. Soc.* **A224**, 491 (1958).

[34] Flaminio, V. *et al.* Compilation of cross-sections III: p and $\bar{\text{p}}$ induced reactions. Tech. Rep. 84-01, CERN-HERA (1984).

[35] Colton, E. & Kirschbaum, A. R. Study of $|T_z| = \frac{3}{2}\Delta(1238)$ Production in pp Interactions at 6.6 GeV/c. *Phys. Rev. D* **6**, 95 (1972).

[36] Kerret, H. D. *et al.* A study of the charge-exchange reaction $pp \to n\Delta^{++}(1232)$ at ISR energies. *Phys. Lett. B* **69**, 372 (1977).

[37] Eisner, R. L. *et al.* Study of the reaction $p_\uparrow p \to n\delta^{++}$ at 6 gev/c with polarized beam. *Phys. Rev. D* **20**, 596–600 (1979).

[38] Gnat, Y. *et al.* One pion production in pp collisions at 16.2 gev/c. *Nucl. Phys.* **B54**, 333–354 (1973).

[39] Mountz, J. D. *et al.* Some features of the reaction $pp \to \delta^{++}(1236)n$ at 6 gev/c. *Phys. Rev. D* **12**, 1211–1218 (1975).

[40] Panvini, R. A Survey of Experimental Results on Multi-Particle Production from High Energy pp and Kp Collisions. In Yang, C. N., Cole, J. A., Good, M., Hwa, R. & Lee-Franzini, J. (eds.) *Proceedings of the Third International Conferences on High Energy Collisions*. Stony Brook (Gordon and Breach, 1969).

[41] Ward, D. R. *et al.* Exclusive annihilation processes in 8.8 GeV $\bar{\text{p}}$ p interactions and comparisons between $\bar{\text{p}}$ p nonannihilations and p p interactions. *Nucl. Phys.* **B172**, 302 (1980).

[42] Bøggild, H. *et al.* Evidence for dominance of Pomeron like exchange in $pp \to NN\pi$ at 19 GeV/c. *Phys. Letters B* **30**, 369 (1969).

[43] Shimizu, F. *et al.* Study of p p interactions in the momentum range 0.9-GeV/c to 2.0-GeV/c. *Nucl. Phys.* **A389**, 445 (1982).

[44] Allaby, J. V. *et al.* Proton proton elastic scattering and nucleon resonance production at high-energies. *Nucl. Phys.* **B52**, 316–382 (1973).

[45] Tan, T. *et al.* An investigation of the 1.4 GeV/c^2 nucleon isobar in proton-proton interactions. *Phys. Lett. B* **28**, 195 (1968).

[46] Hochman, D. *et al.* Single Pion Production in p n Collisions at 11.6-GeV/c. *Nucl. Phys.* **B80**, 45 (1974).

[47] Yekutieli, G. *et al.* Isobar production and diffraction dissociation in $pn \to pp\pi^-$ at 7.0 GeV/c. *Nucl. Phys.* **B40**, 77–97 (1972).

[48] LeGuyadar, J. *et al.* Experimental study of four-prong events in proton proton interactions at 13.1 GeV/c. *Nucl. Phys.* **B35**, 573 (1971).

[49] Goggi, G. *et al.* Analysis of the charge-exchange reaction $pp \to (p\pi^+)(p\pi^-)$ and of $\Delta^{++}\Delta^0$ production at the CERN ISR. *Nucl. Phys.* **B143**, 365 (1978).

[50] Takibaev, Z. S. *et al.* Quasi Two Particle Reactions in Proton Proton Interactions at 19.1-GeV/c Momentum. *Yad. Fiz.* **21**, 1015–1021 (1975).

[51] Wilson, J. W. *et al.* NUCFRG2: An Evaluation of the Semiempirical Nuclear Fragmentation Database. *NASA TP 3533* (1995).

[52] Cucinotta, F. A. *et al.* Description of light ion production cross sections and fluxes on the Mars surface using the QMSFRG model. *Radiat. Environ. Biophys.* **46** (2007).

[53] Wilson, J. W. *et al.* Standardized Radiation Shield Design Methods: 2005 HZETRN. In *Proceedings of the 36th Conference on Environmental Systems (ICES)* (Norfolk, VA, 2006).

[54] Bowman, J. D. *et al.* Abrasion and Ablation of Heavy Ions. Tech. Rep. LBL-2908, Univ. of California (1973).

[55] Rudstam, G. Systematics of Spallation Yields. *Zeitschrift fur Naturforschung* **21a**, 1027–1041 (1966).

[56] Glauber, R. J. *Lectures in Theoretical Physics*, 315 (Interscience, 1959).

[57] Zeitlin, C. *et al.* Fragmentation cross sections of 600 MeV/nucleon ^{20}Ne on elemental targets. *Phys. Rev. C* **64**, 024902 (2001).

[58] Zeitlin, C. *et al.* Heavy fragment production cross sections from 1.05 GeV/nucleon ^{56}Fe in C, Al, Cu, Pb, and CH_2 targets. *Phys. Rev. C* **56**, 388–397 (1997).

[59] Zeitlin, C. *et al.* Fragmentation cross sections of 290 MeV/nucleon and 400-MeV/nucleon ^{12}C beams on elemental targets. *Phys. Rev. C* **76**, 014911 (2007).

[60] Zeitlin, C. *et al.* Fragmentation cross sections of ^{28}Si at beam energies from 290 A MeV to 1200 A MeV. *Nucl. Phys.* **A784**, 341–367 (2007).

[61] Zeitlin, C. *et al.* Fragmentation cross sections of medium-energy ^{35}Cl, ^{40}Ar, and ^{48}Ti beams on elemental targets. *Phys. Rev. C* **77**, 034605 (2008). URL `http://link.aps.org/abstract/PRC/v77/e034605`.

[62] Zeitlin, C. *et al.* Published on Private Website. Data accessed Jan. 2008.

[63] Webber, W. R. *et al.* Individual charge changing fragmentation cross sections of relativistic nuclei in hydrogen, helium, and carbon targets. *Phys. Rev. C* **41**, 533–546 (1990).

[64] Webber, W. R. *et al.* Individual isotopic fragmentation cross sections of relativistic nuclei in hydrogen, helium, and carbon targets. *Phys. Rev. C* **41**, 547–565 (1990).

[65] Cummings, J. R. *et al.* Determination of the cross sections for the production of fragments from relativistic nucleus-nucleus interactions. I. Measurements. *Phys. Rev. C* **42**, 2508–2529 (1990).

[66] Westfall, G. D. *et al.* Fragmentation of relativistic ^{56}Fe. *Phys. Rev. C* **19**, 1309–1323 (1979).

[67] Bertulani, C. A. & Baur, G. Electromagnetic Processes in Relativistic Heavy Ion Collisions. *Phys. Rep.* **163**, 299–408 (1988).

[68] Olson, D. L. *et al.* Factorization of fragment-production cross sections in relativistic heavy-ion collisions. *Phys. Rev. C* **28**, 1602–1613 (1983).

[69] Tull, C. E. Relativistic Heavy Ion Fragmentation at HISS. Tech. Rep. LBL-29718, Univ. of California (1990).

[70] Golovchenko, A. N. *et al.* Total charge-changing and partial cross-section measurements in the reactions of $\sim 110 - 250$ MeV/nucleon ^{12}C in carbon, paraffin, and water. *Phys. Rev. C* **66**, 014609 (2002).

[71] Momota, S. *et al.* Production of projectile-like fragments at intermediate energies. *Nucl. Phys. A* **701**, 150–155 (2002).

[72] Brechtmann, C. & Heinrich, W. Measurements of elemental fragmentation cross section for relativistic heavy ions using CR39 plastic nuclear track detectors. *Nucl. Instrum. Meth. B.* **29**, 675–679 (1988).

[73] Flesch, F. *et al.* Projectile fragmentation of silicon ions at 490 A MeV. *Radiat. Mes.* **34**, 237–240 (2001).

[74] Leistenschneider, A. *et al.* Fragmentation of unstable neutron-rich oxygen beams. *Phys. Rev. C* **65**, 064607 (2002).

[75] Iancu, G. *et al.* Nuclear fragmentation cross-sections of 400 A MeV ^{36}Ar and ^{40}Ar in collisions with light and heavy target nuclei. *Radiat. Mes.* **39**, 525–533 (2005).

[76] Viyogi, Y. P. *et al.* Fragmentations of ^{40}Ar at 213 MeV/Nucleon. *Phys. Rev. Lett.* **42**, 33–36 (1979).

[77] Alexio, N. F. & Bertulani, C. A. Coulomb Excitation in Intermediate-Energy Collisions. *Nucl. Phys. A* **505**, 448–470 (1989).

[78] Korejwo, A. *et al.* The measurement of isotopic cross sections of ^{12}C beam fragmentation on liquid hydrogen at 3.66-GeV/nucleon. *J. Phys.* **G26**, 1171–1186 (2000).

[79] Korejwo, A. *et al.* Isotopic cross-sections of ^{12}C fragmentation on hydrogen measured at 1.87-GeV/nucleon and 2.69-GeV/nucleon. *J. Phys.* **G28**, 1199–1208 (2002).

[80] Caamano, M. *et al.* Production cross-sections and momentum distributions of fragments from neutron-deficient ^{36}Ar at 1.05-A-GeV. *Nucl. Phys.* **A733**, 187–199 (2004). `nucl-ex/0310033`.

[81] Knott, C. N. *et al.* Interactions of relativistic neon to nickel projectiles in hydrogen, elemental production cross sections. *Phys. Rev. C* **53**, 347–357 (1996).

[82] Knott, C. N. *et al.* Interactions of relativistic ^{36}Ar and ^{40}Ar nuclei in hydrogen: Isotopic production cross sections. *Phys. Rev. C* **56**, 398–406 (1997).

[83] Tripathi, R. K. *et al.* Universal Parameterization of Absorption Cross Sections. Tech. Rep. TP-3621, NASA (1997).

[84] Silberberg, R. *et al.* Semiempirical cross sections and applications to nuclear interactions of cosmic rays. In Shen, B. S. P. & Merker, M. (eds.) *Spallation Nuclear Reactions and Their Applications*, 49 (D. Reidel Publ. Co., 1976).

[85] Engelmann, J. J. *et al.* Charge composition and energy spectra of cosmic-ray nuclei for elements from Be to NI - Results from HEAO-3-C2. *A&A* **233**, 96–111 (1990).